# CREEP RUPTURE BEHAVIOR OF TRANSITION WELD JOINT BETWEEN P91 STEEL AND AISI 304 AUSTENITIC STAINLESS STEEL

by

Javed Akram

A dissertation submitted to the faculty of
The University of Utah
in partial fulfillment of the requirements for the degree of

Doctor of Philosophy

Department of Metallurgical Engineering

The University of Utah

December 2016

**The University of Utah Graduate School**

# STATEMENT OF DISSERTATION APPROVAL

The dissertation of **Javed Akram**

has been approved by the following supervisory committee members:

| | | |
|---|---|---|
| **Manoranjan Misra** | , Chair | **05-26-2016** Date Approved |
| **Prasad Rao Kalvala** | , Member | **05-26-2016** Date Approved |
| **Sivaraman Guruswamy** | , Member | **05-26-2016** Date Approved |
| **Michael L Free** | , Member | **05-26-2016** Date Approved |
| **Alagar Krishnan Balaji** | , Member | **05-26-2016** Date Approved |

and by **Manoranjan Misra** , Chair/Dean of

the Department/College/School of **Metallurgical Engineering**

and by David B. Kieda, Dean of The Graduate School.

# ABSTRACT

The objective of this work is to understand the mechanisms of high temperature failures in dissimilar metal welds between modified 9Cr-1Mo steel (P91) and austenitic stainless steel (AISI 304). It is proposed to apply functionally graded multilayers between these metals by friction-based solid state welding methods to obtain smooth and gradual transition. The study examined the effect of the smooth and gradual transition in physical and metallurgical properties imparted by the weld interlayers on the stress rupture behavior of weld transition joints between P91 and AISI 304. Two types of transitions joints were developed: welds with three interlayers (P91/IN625/IN600/IN800H/AISI304) and welds with a single interlayer (P91/IN600/AISI304).

The experimental study involved the evaluation of microstructural and mechanical properties of weld interlayers and base metals. The mechanical property evaluation included hardness profiles across weld interfaces and stress rupture behavior. The evolution of microstructure in friction welds was studied using cellular automata modeling technique.

Dynamically recrystallized grain sizes predicted by the Cellular automata method were found to be comparable with the experimental results. The strain rates predicted by the model at the center and edge of the weld fabricated with 1500 RPM rotational speed were found to be 1850 $s^{-1}$ and 290 $s^{-1}$, respectively.

A soft zone in the heat affected zone of P91 was observed, 2mm away from the

weld interface which was found to be due to the carbon diffusion. Three interlayer weld transition joints showed better rupture life than the single interlayer welds. The increased rupture life of three interlayer welds is attributed to the gradual transition in coefficient of thermal expansion between P91 steel and AISI 304. A stress exponent of 3 was obtained suggesting creep mechanism as viscous glide due to solute drag effect. Creep damage tolerance factor ($\lambda$) of 1.75 was obtained which indicates the damage mechanism is cavity growth by the combined effect of power law creep and diffusional creep.

*I would like to dedicate my thesis to Ammi & Abbu, my family, friends, and my beloved wife.*

TABLE OF CONTENTS

LIST OF TABLES

LIST OF FIGURES

# ACKNOWLEDGEMENTS

I sincerely thank these individuals for their pivotal role in my dissertation work: my advisors Dr. Mano Misra for giving me the opportunity and continuous support and Dr. Prasad Rao Kalvala for technical guidance and valuable input to experiments and writing, and my committee members Dr. Sivaraman Guruswamy for sharing his expertise and guidance when needed, and Dr. Michael Free and Dr. A.K. Balaji for their useful feedback to my dissertation project.

I am also grateful to Dr. Sekhar Rakurty, Dr. Vikas Jindal, and Dr. Deepankar Pal for helping me progress with the microstructure modeling project, Dr. Indrajit Charit for giving access to the creep facility and his expert advice, and our collaborators in the University of Louisville, especially Dr. J.J.S. Dilip for carrying out TEM characterization, all of whom have been instrumental in the completion of my dissertation work. Lastly, I want to thank former undergraduate research assistant James Samuel for assisting me with the friction welding machine.

I gratefully acknowledge the financial help from the National Science Foundation (NSF Grant No. 1234079) in supporting my work. I would also like to thank the University of Utah Graduate School for awarding me the Graduate Research Fellowship.

# CHAPTER 1

# INTRODUCTION

The need for increasing steam temperatures to enhance thermal efficiencies led to the development of a variety of Cr-Mo steels. For example, current plants operating with steam temperature of 811 K have thermal efficiencies of around 35% and by increasing the steam temperature to 873 K, the efficiencies of these plants could rise to around 42%. This increase in thermal efficiency significantly reduces fuel consumption and environmental impact. Therefore, high efficiency pulverized coal power plants capable of operating at steam pressures and temperatures much higher than possible today are under development to provide relatively low cost power with much less pollution [1].

Projects sponsored by the U.S. Department of Energy and the Ohio Coal Development Office have set 1033 K/35 MPa as the goal for what is termed “Advanced Ultra Super Critical” (AUSC) coal-fired power plants [2]. Chromium (9%) steels, such as T/P91 (T stands for tube and P for plate), T/P92, and E911, provide the higher creep rupture strengths required for the higher steam temperatures. For the same design conditions, the rupture strength of T/P91 or T/P92 was found to be higher compared to conventional Cr-Mo steels and close to austenitic stainless steels [3,4]. However, steam oxidation resistance is the drawback of T91/T92 steels. In spite of their high temperature mechanical properties, the steam oxidation resistance of T91/T92 is poor compared to

austenitic stainless steels (Figure 1.1) [4]. This limits the operating temperature of T/P91 to 873 K and T/P92 to 893 K. For boiler super heater tubes experiencing 903 K, austenitic stainless steels such as AISI 316, 304H, and 347H steels are used. These heater tubes have to be joined to steam headers made of T91. Hence, dissimilar, multimaterial welding becomes necessary. The joining of these metals is normally carried out by fusion welding techniques using Inconel filler wires. For example, modified 9Cr-1Mo ferritic steel and austenitic stainless steels are joined by using Ni-based fillers such as Inconel 82/182 . Though dissimilar welding has been practiced for many high temperature tubular applications, numerous failures have been reported [5–9]. A typical failure on the ferritic steel side (160 MPa, 823 K, Rupture Time = 10,547 h) is shown in Figure 1.2 [10]. Compared to the base metal counterparts, stress rupture properties of dissimilar welds of Cr-Mo steels with austenitic stainless steels were found to be inferior, showing lower creep rupture lives as shown in Figure 1.3 [10].

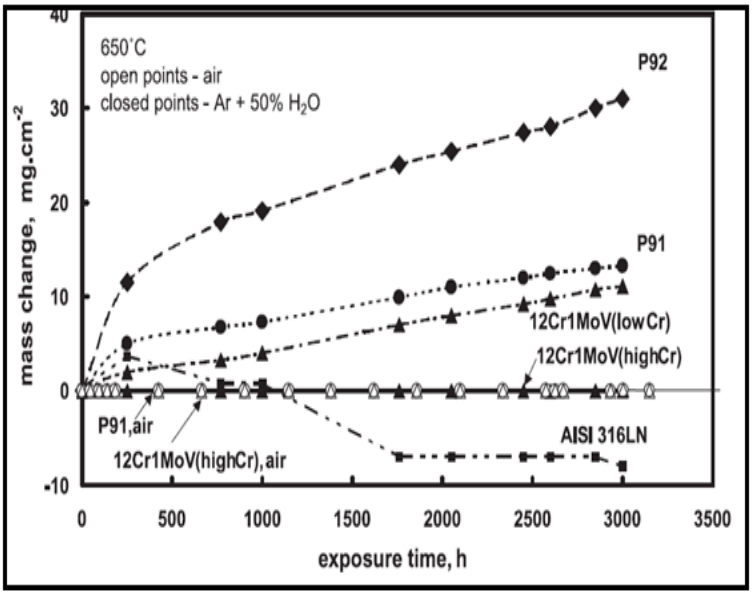


Figure 1.1 High temperature steels -mass change data for Cr steels exposed in Ar-50% H2O and in air at 922 K [4].

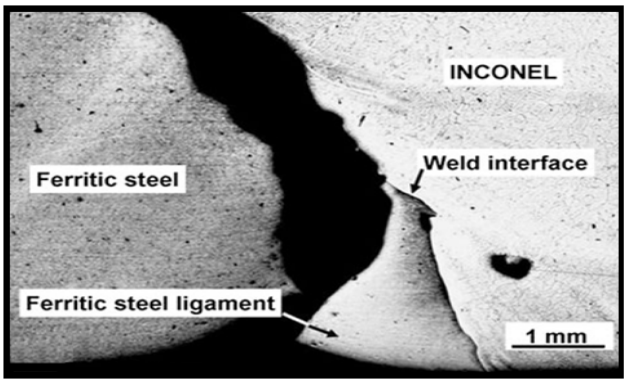


Figure 1.2 Creep failure at the P91 and Inconel 182 (filler) weld interface[10].

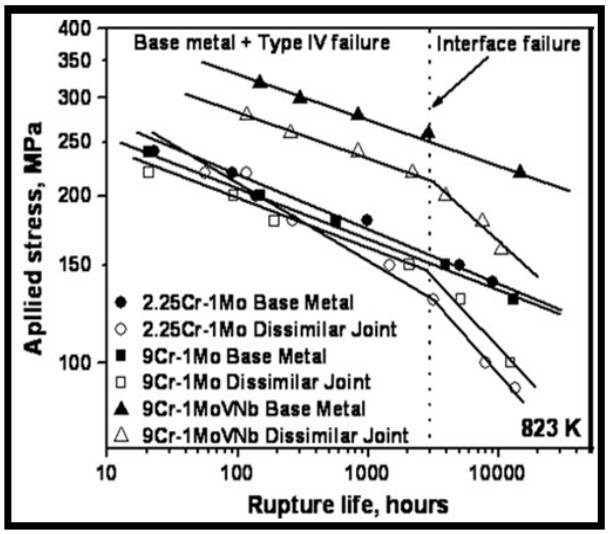


Figure 1.3 Creep rupture lives of different dissimilar welds and base metals [10].

One of the mechanisms for the premature failures is reported to be the coefficient of thermal expansion (CTE) mismatch between the two metals [11]. Inconel 82 filler has a CTE in between the two metals and provides transition in CTE values between these two metals. As this approach is found inadequate to mitigate the premature failures of the dissimilar metal welds, a modified approach has to be adopted. In the current work, we propose the application of number of Ni-based alloy interlayers to form a transition joint resulting in a gradual change in CTE rather than an abrupt change in CTE between

ferritic steel and austenitic stainless steels. Another failure mechanism proposed is carbon-denuded zone formation in the ferritic steel side [12] due to carbon diffusion towards the austenitic stainless steel side. We propose that our approach will result in not only a gradual change in CTE but also help reduce the extent of carbon diffusion from the HAZ of the ferritic steel side.

In this work, we intended to achieve the transition joint between P91 and AISI 304 through friction surfacing/ friction welding techniques which have not been explored so far. Friction surfacing, an off shoot of friction stir welding, is an ideal process to build relatively thick 3D parts, as it involves friction stir addition of material to a substrate rather than simply stirring a joint between adjoining materials. Earlier studies have shown that friction surfaced layers exhibit good bond strength with the substrate material [13]. Friction welding is also a useful technique to realize such graded layered structures. As no melting is involved, metallurgical issues such as microsegregation and physical limitations such as porosity and tensile residual stresses are reduced. Joining and cladding of metals using friction (e.g., ultrasonic welding and friction stir welding) are well-known. Friction bonding has been applied previously to the surfacing of objects for corrosion protection and for repair of worn areas [14]. However, detailed studies on the application of friction-based processes for additive manufacturing of large components with multilayered structure are limited. Linear friction welding was applied to build simple blocks which were used for fabricating large structures [15]. These structures were found to exhibit good mechanical properties [16]. Though rotary friction welding and friction stir welding were also used for the purpose of additive manufacturing [17], it was more like building larger structures by welding small size pieces together. In

summary, friction-based processes have been attempted for use as additive manufacturing processes but they need further studies. In this regard, friction surfacing and friction welding are solid-state processes that are ideal for additive manufacturing. In the current work, friction surfacing and friction welding methods are applied for developing weld transition joints between P91 and AISI 304 involving selected Ni-based alloy layers deposited on a P91 substrate. The microstructural changes in the welds in the as-welded and post weld heat treated conditions affect their service behavior. Therefore, the creep behavior and mechanisms of these newly proposed welds have to be understood. Keeping these challenges in mind, this proposed hypothesis has the following research objectives:

1. Development and characterization of weld transition joints between P91 and AISI 304 by friction surfacing and friction welding methods.
2. Microstructure modeling of dynamic recrystallization using cellular automata.
3. Carbon diffusion studies across weld transition joints.
4. Creep behavior of dissimilar metal weld joints.

## 1.1 References

[1] R. Viswanathan, J. Tanzosh, B. Vitalis, R. Power, U.S. program on materials technology for ultrasupercritical coal-fired boilers, in: Adv. Mater. Technol. Foss. Power Plants Proc. 5th Int. Conference. (2008) 1–15.

[2] R. Purgert, P. Rawls, V. Viswanathan, Coal-fired power materials, Adv. Mater. Process. (2008) 47–49.

[3] K. Coleman, I.A. Shibli, Failures of P91 steel at the west burton plant in england raise concerns about the long term behavior of the advanced steel, 2003. http://www.ommi.co.uk/etd/ETD-EPRI- P91 Failures.pdf.

[4] P.J. Ennis, A. Czyrska-Filemonowicz, Recent advances in creep-resistant steels for power plant applications, Sadhana. 28 (2003) 709–730. doi:10.1007/BF02706455.

[5] R.L. Klueh, J.F. King, Austenitic-ferritic weld joint failures, Weld. J. 61 (1982)

302s–311s.

[6] R.W. Emerson, R.W. Lackson, C.A. Dauber, Transition joints between austenitic and ferritic steel piping for high temperature steam service, Weld. J. 41 (1962) 385s–393s.

[7] A. Joseph, A.S. Ramesh, T. Jayakumar, N. Murugan, Failure analysis of a dissimilar weld joint in steam generator, Pract. Metallogr. 38 (2001) 667–679.

[8] H.Y. Lee, S.H. Lee, J.B. Kim, J.H. Lee, Creep-fatigue damage for a structure with dissimilar metal welds of modified 9Cr-1Mo steel and 316L stainless steel, Int. J. Fatigue. 29 (2007) 1868–1879. doi:10.1016/j.ijfatigue.2007.02.009.

[9] J. Cao, Y. Gong, Z.G. Yang, X.M. Luo, F.M. Gu, Z.F. Hu, Creep fracture behavior of dissimilar weld joints between T92 martensitic and HR3C austenitic steels, Int. J. Press. Vessel. Pip. 88 (2011) 94–98. doi:10.1016/j.ijpvp.2011.01.003.

[10] K. Laha, K.S. Chandravathi, P. Parameswaran, S. Goyal, M.D. Mathew, A comparison of creep rupture strength of ferritic/austenitic dissimilar weld joints of different grades of Cr-Mo ferritic steels, Metall. Mater. Trans. A Phys. Metall. Mater. Sci. 43 (2012) 1174–1186. doi:10.1007/s11661-011-0957-8.

[11] M.M. Rahman, A.K. Kadir, Failure analysis of high temperature superheater tube (HTS) of a pulverized coal-fired power station, in: Proceeding Int. Conf. Adv. Sci. Eng. Inf. Technol. (2011) 517–522.

[12] R.J. Christoffel, M.R. Curran, Carbon migration in welded joints at elevated temperatures, Weld. J. 35 (1956) 457s–468s.

[13] J. Gandra, H. Krohn, R.M. Miranda, P. Vilaça, L. Quintino, J.F. Dos Santos, Friction surfacing - a review, J. Mater. Process. Technol. 214 (2014) 1062–1093. doi:10.1016/j.jmatprotec.2013.12.008.

[14] U.S. Pat. Nos. 6,457,629 ;5,469,617; 5,183,390; 5,077,081; 4,959,241 and 4,930,675.

[15] K.T. Slattery, K.A. Young, U.S. Patent # 7398911 Structural assemblies and preforms therefor formed by friction welding, 2008.

[16] M.J. Russell, R.R. Boyer, Recent developments in linear friction welding of Ti for aerospace applications, in: Aeromat 2006, Seattle, Washington, USA, 2006.

[17] P.L. Threadgill, M.J. Russell, Friction welding of near net shape preforms in Ti-6Al-4V, in: 11th World Conf. Titan. (JIMIC-5), Kyoto, Japan, 2007.

# CHAPTER 2

# LITERATURE REVIEW

This chapter presents a background on (1) chemical composition and microstructural details of materials used to develop the dissimilar metal welds, (2) failure mechanisms of dissimilar metal welds, (3) creep rupture behavior and deformation mechanism of base metal (P91), similar metal welds (P91-P91), and dissimilar metal welds.

## 2.1 Chemical composition and microstructural details of materials used to develop the dissimilar metal welds

### 2.1.1 Cr-Mo steels

Cr-Mo steels are widely used for various components in the power generation industry due to their high creep strength, low cost compared to austenitic and nickel-based alloys, ease of fabrication, and availability. Development of different grades of Cr-Mo steel was driven by a continuous need to optimize the economics and efficiency of power generation systems. Following are the advantages of developing high strength Cr-Mo steels: (a) increased efficiency can be achieved by raising the plant operating temperature, (b) wall thickness of the material can be reduced which can cut down the economics in production, and c) ease of handling and maintenance. Many

components/systems used in the power generation industries such as boilers, heaters, heat exchangers, hydrocrackers, and heat exchangers are made from Cr-Mo steels. The usage of various Cr-Mo steel in various components in the power industry and their maximum operating temperatures is listed in Table 2.1.

2.1.1.1 Effect of alloying elements

In Cr-Mo steels, various elements such as carbon (C), nitrogen (N), nickel (Ni), manganese (Mn), copper (Cu), cobalt (Co), chromium (Cr), molybdenum (Mo), niobium (Nb), vanadium (V), tungsten (W), silicon (Si), titanium (Ti), and aluminum (Al) are present in various proportions. These elements are responsible for enhancing the strength, toughness, and various other properties. They also help stabilize the different phases in the given system and are grouped as ferrite stabilizers and austenite stabilizers. C, N, Ni, Mn, Cu, and Co are austenite phase stabilizers while Cr, Mo, Nb, V, W, Si, Ti, and Al are ferrite stabilizers. One has to be careful while adding these elements because they can greatly affect the cooling curves. Not having prior knowledge of their effects may result in partially transformed phases which will eventually alter the desired property of a material.

Chromium as a major alloying element helps increase the room and high temperature strength of steel and improves the wear and corrosion resistance. Cr combines with carbon and nitrogen and forms $Cr_{23}C_6$, and $Cr_2N$ types of carbides. The $Cr_{23}C_6$ carbides are responsible for the high creep strength in these steels and are mostly found at the lath boundaries and prior austenitic grain boundaries.

Niobium also combines with carbon and nitrogen and forms different types of

Table 2.1 Various Cr-Mo steels used for power boiler applications [1].

| Cr-Mo Alloy Type | ASTM & ASME Alloy Designation | Application | Maximum Service Temperature, K |
|---|---|---|---|
| 0.5 Mo | *T/P1 | Pressure Vessels; *$R_p$0.2>290 MPa, *$R_m$>500 MPa | < 733 |
| 1.25Cr-0.5Mo | T/P11 | Steam Headers | <808 |
| 1.0Cr-0.5Mo | T/P12 | Water walls; part of evaporator | <818 |
| 1.25Cr-1MoV | | Main steam pipe; reheater steam pipe; $R_p$0.2> 440 MPa, $R_m$ 590-780 MPa | <818 |
| 2.25Cr-1Mo | T/P22 | Parts of superheaters; $R_p$0.2> 310 MPa, $R_m$ 515-690 MPa | <808 |
| 2.25Cr-1MoV | T/P22V | Parts of superheaters; $R_p$0.2> 415 MPa, $R_m$ 585-760 MPa | <755 |
| 2.25Cr-Mo-VW | T/P23 | Parts of superheater; membrane walls | <823 |
| 2.25Cr-1MoV | T/P24 | Parts of superheater; membrane walls | <823 |
| 9Cr-1Mo mod. | T/P91 | Steam headers, superheaters for Ultra Super Critical boilers; $R_p$0.2> 450 MPa, $R_m$ 630-790 MPa | <858 |
| 9Cr-0.5Mo-WV | T/P912 | Steam headers, superheaters for Ultra Super Critical boilers | <898 |
| 12Cr-1Mo-NiV | T/P911 | Steam headers, superheaters; Rp> 500 MPa, Rm 700-850 MPa | <858 |

(*$R_p$ is the 0.2% offset yield strength and $R_m$ is the ultimate tensile strength)

precipitates such as NbC, NbN, Nb(CN), and (NbV)C. They are finely dispersed at the grain boundaries as well as in the matrix. These finely dispersed MX type precipitates pin the mobile dislocation and improve the long-term creep strength. Vanadium and molybdenum are ferrite stabilizers and form different types of carbides and help improve the creep strength of a material. Molybdenum participates in forming carbides such as $M_{23}C_6$ carbides ($(Cr_{16}Fe_6Mo)C_{6)}$ and vanadium forms $V_4C_3$ carbides. An increased amount of Mo in the system leads to the formation of laves phase which is detrimental to creep strength.

Carbon and nitrogen are austenite formers and play a major role in forming carbides and carbo-nitrides with Cr, Nb, Mo, and V which imparts high creep strength in these materials. However, higher percentage of carbon decreases the toughness, corrosion resistance, and weldabiltiy of the material [2]. Although nitrogen is an austenite stabilizer, the amount required is generally very high.

Nickel is also an austenite stabilizer but less effective than carbon and nitrogen; however, it is preferred in non-nuclear applications because it has fewer adverse effects. Addition of manganese increases the hardenability and wear resistance but high manganese steel is prone to embrittlement during thermal aging due to chi ($\chi$) phase formation [2]. Cobalt is an expensive austenite stabilizer and its amount has to be kept to a minimum in steel components used in fusion reactor systems because of its high residual radioactivity induced by neutron irradiation. Table 2.2 lists the typical concentration ranges (in wt%) of alloying elements present in modified 9Cr-1Mo steel.

Table 2.2 Typical alloying elements present in modified 9Cr-1Mo steel.

| Elements | C | Mn | P | S | Si | Cr |
|---|---|---|---|---|---|---|
| Composition, wt% | 0.08-0.2 | 0.3-0.6 | 0.02 max | 0.01 max | 0.2-0.5 | 8.0-9.5 |
| | Mo | Ni | V | Nb | Al | N |
| | 0.85-1.05 | 0.4 max | 0.18-0.25 | 0.06-0.10 | 0.04 max | 0.03-0.07 |

2.1.1.2 Strengthening mechanisms in modified Cr-Mo steels

The mechanisms by which modified 9Cr-1Mo steels get their high temperature strength are classified as solute hardening, precepitiation or dispersion hardening, dislocation hardening, and boundary or sub-boundary hardening.

Strengthening of pure iron is enhanced by dissolving various alloying elements in the iron lattice to form a solid solution. Depending on the size of the solute atoms, solid solution can be classified as substitutional or interstitial. If the atomic radius of solute atoms is much smaller than parent (Fe) atomic radius, they occupy the interstitial space of Fe lattice forming interstitial solid solution. For example, C and N atoms have atomic radii that are much smaller than the radius of Fe atoms, and form interstitial solid solution with Fe. If the atomic radius of solute atoms is larger or smaller by less than ~15 % of the solvent atom, they form substitutional solid solution. Substitutional solute atoms such as Mo and W have atomic radii larger than parent (Fe) atom and have been favored for solid solution strengthening in ferritic and austenitic steels. Addition of both substitutional and interstitial solute atoms in Fe lattice creates large lattice distortion and impedes the movement of dislocation resulting in the increased strength of a material. Addition of 2.3

mass % of W in α iron showed reduced creep rate on the order of three magnitude as compared to plain α iron [3].

Precipitation hardening is considered as the main strengthening mechanism in high chromium alloy steels. Alloying elements such as Cr, Mo, Nb, W, and V combine with carbon and nitrogen and form various types of carbides and carbonitrides. Table 2.3 is the list of different types of precipitates and their location.

These fine dispersed precipitates are mostly located at lath boundaries and in the matrix and are responsible for stabilizing the subgrain structure against recovery [4]. These precipitates pin the movement of dislocations which helps in improving the creep strength of the material. To move a dislocation through these precipitates, a minimum stress known as threshold stress is required. Several mechanisms of how these dislocations bypass the precipitates have been proposed, such as Orowan mechanism, local climb mechanism, general climb mechanism, and Srolovitz mechanism [4]. The Orowan stress is given by the following relation:

$$\sigma_{or} = \frac{0.8MGb}{\lambda}$$

where M is the Taylor factor, G is a shear modulus, b is the burger vector, and λ is the mean interparticle spacing. The smaller the interparticle spacing (λ), the higher the stress required to bypass through the precipitates.

The microstructure of 9Cr-1Mo steels consists of lath martensite structure which has high dislocations density usually in the range of $1\text{-}10\times10^{14}$ $m^{-2}$. Dislocation motion is usually impeded by the elastic stress/strain fields of the other dislocation present in the lattice. This high dislocation density gives high strength to this steel by these dislocation interactions.

Table 2.3 Different precipitates, their crystal structure and composition in Cr-Mo steels [5].

| Precipitate Phase | Crystal Structure, Lattice Parameter | Composition | Distribution of Precipitates |
|---|---|---|---|
| $M_{23}C_6$ | FCC, 1.066 nm | $(Cr_{16}Fe_6Mo)C_6$, $(Cr_4Fe_{12}Mo_4Si_2WV)C_6$ | Coarse particles at prior austenite grain and martensite lath boundaries and fine intra-lath particles |
| MX | FCC, 0.444-0.447 nm | NbC, NbN, VN, (CrV)N, Nb(CN) and (NbV)C | Undissolved particles and fine precipitates at martensite lath boundaries |
| $M_2X$ | Hexagonal, a = 0.478 nm, c = 0.444 nm | $Cr_2N$, $Mo_2C$, and $W_2C$ | Martensite lath boundaries ($Cr_2N$ and $Mo_2C$); prior austenite grain boundaries ($Mo_2C$); intra-lath ($Mo_2C$ and $W_2C$); δ-ferrite in duplex steel [$Cr_2(CN)$ and $(CrMo)_2$ and $(CrMo)_2(CN)$] |
| Z-phase | Tetragonal, a = 0.286 nm, c = 0.739 nm | (CrVNb)N | Large plate like particles in the matrix after creep straining at 873 K |
| η-carbide | Diamond cubic, 1.07-1.22 nm | $M_6C$, $(Fe_{39}Cr_6Mo_4Si_{10})C$ | Prior austenite grain and martensite lath boundaries and intra-lath |
| Vanadium carbide | FCC, 0.420 nm | $V_4C_3$ | Low number density in matrix |
| Laves phase | Hexagonal, a = 0.4744 nm, c = 0.7725 nm | $Fe_2Mo$, $Fe_2W$, and $Fe_2(MoW)$ | Prior austenite grain and martensite lath boundaries and intra-lath; δ-ferrite in duplex steels |
| Chi(χ) | BCC, 0.892 nm | $M_{18}C$ or $Fe_{35}Cr_{12}Mo_{10}C$ | Intra-martensite lath; δ-ferrite in duplex steels |

$$\sigma_p = 0.5MGb\sqrt{\rho}$$

where ρ is the dislocation density in the matrix. Hardening by dislocation-dislocation interactions is useful mainly for room temperature. At high temperature, dislocation hardening effect gets less effective due to dislocation annihilation via recovery and recrystallization of deformed matrix forming new dislocation free grains. Therefore, dislocation hardening is useful for enhancing creep resistance over a short term but not useful over a long term.

High chromium alloy steels in tempered condition have martensitic structure which consists of laths and blocks. In these lath and block boundaries, fine carbides and carbonitrides are present which are responsible for high temperature strength in high alloy steel. These laths and blocks can be considered as elongated subgrains. Apart from lath boundaries, these precipitates, such as $M_{23}C_6$, typically having a rod like structure, and MX, spherical in shape, also enhance the sub-boundary hardening. The hardening by sub-boundary is given by the following relation [4]:

$$\sigma_{sg} = \frac{10Gb}{\lambda_{sg}}$$

where $\lambda_{sg}$ is the width of the lath boundary. Hardening effect by sub-boundary is inversely proportional to the width of the lath boundary. Finer lath martensite boundaries will give higher sub-boundary hardening. During long-term creep, lath boundary becomes wider resulting in decreased sub-boundary hardening effect. Presence of precipitates at the lath boundaries help in reducing the coarsening of lath boundaries; therefore, these precipitates not only increase the creep strength of material by precipitation hardening but also add to the creep strength by sub-boundary hardening.

2.1.1.3 Tempering of modified Cr-Mo steels

The high temperature strength of the modified 9Cr-1Mo steels is due to the presence of lath martensitic structure and presence of fine carbides at the lath boundaries and in the matrix. Evolution of these fine carbides and carbonitrides are temperature dependent. Therefore, understanding of tempering characteristic of these steels is very important because all these carbides precipitate from matrix during tempering. Apart from carbide precipitation during temperature, phase transformation at high temperature heat treatment is also very important. Figure 2.1 is the equilibrium phase diagram of Fe-Cr-0.1wt%C system. It can be seen from the equilibrium phase diagram that the composition of Fe- 9Cr-0.1%C is close to Liquid+δ+γ region (δ ferrite is the high temperature ferrite phase) at high temperature. The high temperature heat treatment and temperature excursion during welding operation will result in varying amounts of austenite, δ-ferrite, and undissolved carbides which will eventually affect the transformation characteristic of austenite to martensite. Table 2.4 tabulates the different phases present in the microstructure as a function of austenitising temperature [6].

At 873 K, $M_2X$ ($Cr_2N$) needles precipitate at the dislocations throughout the matrix which provide dispersion strengthening and also maintain high dislocation density. In the later stage of tempering these needle like precipitates, ($M_2X$) become coarser and proceed with precipitation of $M_{23}C_6$ at the grain and tempered lath boundaries [6]. At higher temperature heat treatments, $M_2X$ precipitates dissolve in the matrix and leave only $M_{23}C_6$ precipitates. The fine precipitates such as NbC and VC usually form throughout the matrix and provide a secondary hardening effect in these steels.

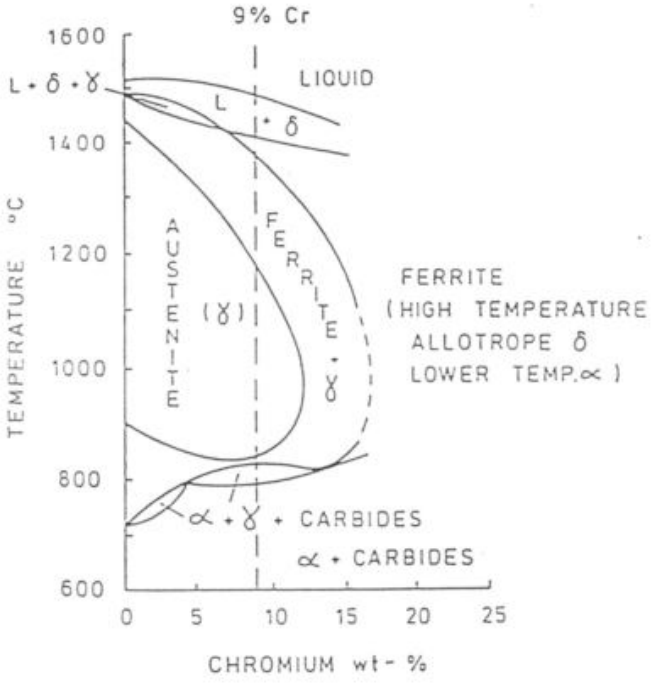


Figure 2.1 Equilibrium phase diagram of Fe-Cr-0.1wt%C system [6].

Table 2.4 Different phases present in 9Cr-1Mo steel as a function of austenitising temperature [6].

| Temperature, K | Structure |
|---|---|
| 1173 | γ + undissolved α + undissolved $M_{23}C_6$ |
| 1273 | Coarser γ + fine undissolved $M_{23}C_6$ |
| 1373 | Coarse grained γ |
| 1473 | γ + 35% δ-ferrite |

### 2.1.2 Austenitic stainless steels for high temperature applications

The AISI 304 grade stainless steel is the most well-known grade of stainless steel with a composition Fe-18%Cr-8%Ni. Carbon is an important impurity and influences the corrosion resistance and mechanical properties of austenitic stainless steels. 'L' grade austenitic stainless steels such as 304L etc., are used mainly for applications involving corrosion where intergranular corrosion due to chromium carbide precipitation has to be avoided. The carbon content, in this case, is restricted to 0.03 wt% or below. AISI 316 grade is the austenitic stainless steel with the composition Fe-18% Cr-8%Ni-2%Mo. The addition of about 2% Mo improves its corrosion and creep resistance. The low carbon version is called 316L. In order to circumvent intergranular corrosion, Nb and Ti are added to austenitic stainless steel which are known as 347 and 321 grade stainless steels, respectively. In contrast to "L" grade, the "H" grades austenitic stainless steels such as 304H grade stainless steel are used mainly for applications involving relatively high temperatures. For example, 304H grade stainless steel is used for super heater tubes in power boilers [7]. The high carbon (in contrast to the "L" grades) will help the stainless steels to retain their high temperature strength when exposed for longer periods of time. The minimum and maximum carbon contents for "H" grades are 0.04% and 0.10%, respectively. In the present study, AISI 304 containing 0.08% C was used.

### 2.1.3 Inconel alloys

In the present study, Inconel 600, 625, and 800H alloys were used to fabricate weld transition joints made with friction surfacing/welding process to study the stress rupture behavior. Inconel 718 was also included for the preliminary studies involving

friction surfacing. In the following paragraphs, the chemical composition and metallurgical aspects of these alloys are presented.

Inconel 600 [8] is considered to be an austenitic solid-solution alloy. It contains about 72% Ni, 16% Cr, and 8% Fe. In this alloy, titanium nitrides, titanium carbides, and chromium carbides are observed in the austenitic matrix. When exposed to temperatures between 813 and 1253 K, precipitation of chromium carbides occur mainly at the grain boundaries and to some extent in the matrix.

Inconel 625 is considered as a solid-solution alloy, the strength of which is derived by the hardening effect of refractory metals addition such as niobium and molybdenum [9,10]. It contains about 58% Ni, 21% Cr, 5% Fe, 9% Mo, 3.5% Nb, 0.4% Ti, and 0.4% Al. Although the main strengthening is due to solid solution strengthening, the alloy responds to aging (823-1123 K) [11] resulting in the formation of precipitation of metastable phases (such as $Ni_3Nb$) leading to increased strength. Aging also results in the precipitation of various carbides such as MC, $M_6C$, and $M_{23}C_6$ [12–14].

Inconel 800H [15] is an austenitic solid-solution alloy with about 40%Fe, 20%Cr, and 35%Ni. It contains Ti, and Al to provide precipitation strengthening. The following precipitates are observed in the alloy: Titanium nitrides, titanium carbides, and chromium carbides. The nitrides are very stable at all temperatures below the melting point of the alloy. Precipitation of chromium carbides occurs between 813 and 1368 K.

## 2.2 Failure mechanism of dissimilar metal joints

The dissimilar metal joints are subjected to very high temperatures during service and also experience thermal fluctuations during shut down and startup of power plant.

Combination of service environment and different chemical composition of material across the weld interface creates a lot of metallurgical issues over a long period of service and is responsible for premature failure of these dissimilar joints. The main reasons cited for these failures are the difference in the coefficient of thermal expansion (CTE) between ferritic and austenitic stainless steel [16–19] and carbon migration from ferritic to austenitic steel [6,17–21]. These factors are explained in detail in the following sections.

### 2.2.1 Coefficient of thermal expansion

In the temperature range from 293-873 K, the average linear CTE of ferritic steel is 13.5-14.4 μm/m/$^0$K, while for austenitic stainless steels, it is 17.1-18.0 μm/m/$^0$K. At elevated temperature, ferritic steel will try to constrain the stainless steel weld from expanding because of its lower CTE. This results in build-up of large local tensile stresses at the interface and leads to failure of the joint [22]. In order to have a transition in CTE in fusion welds, methods such as a) using filler metals with an intermediate CTE or b) using an intermediate alloy with a CTE in between two metals have been adopted [23]. Although these changes helped extend the weld life, they did not provide a long-term solution to the problem and failures still occur in joints prepared with these modifications [24–26].

### 2.2.2 Carbon diffusion

Apart from differences in CTE, carbon diffusion from ferritic steel to austenitic stainless steel [21,27,28] produces a carbon-denuded heat affected zone (HAZ) within the

ferritic steel adjacent to the weld interface. A majority of transition joint failures were attributed to the eventual failure by the link up of creep voids within the carbon-denuded zone. This mechanism has been supported by careful characterization of both laboratory and field-induced failures. The driving force for carbon diffusion comes from different chemical compositions of material at the interface. The carbon diffusion occurs during welding operation, heat treatment, and mainly during service at elevated temperature. The difference in carbon and chromium content provides gradient across the weld interface needed for the diffusion of carbon atoms from one side to other side of the material. Carbon diffuses from the high carbon content side to low carbon content side material, by downhill diffusion driven by the carbon gradient. On the other hand, carbon diffuses from the low chromium content side to high content side, uphill diffusion driven by the chromium gradient. As carbon diffusion progresses with time, one side is left behind with a zone which is depleted in carbon and the other side is left with enrichment of carbon content. The zone with depleted carbon content is referred to as the carbon-denuded zone or soft zone. This zone is prone to void formation during the service period and eventually all the voids link up together and propagate the crack inside the material.

### 2.2.3 Other factors

Though coefficient of thermal expansion (CTE) and carbon diffusion are the main failure mechanisms proposed, other factors are also found to aid the failure of these joints. These factors include oxide notch formation at the ferritic side, change in chemical composition of materials at the interface, and carbide formation at the interface. Oxide formation mostly occurs near the fusion line in the ferritic side of the dissimilar metal

weld. Oxide notch was found to form due to the difference in chemical composition at the interface and difference in chromium content between ferritic and austenitic steel [6]. Once the oxide forms, local stresses at the interface break these oxides and expose fresh surface to allow further oxide formation. The oxide notch is the area of localized oxidation [17] that causes stress concentration and leads to crack propagation. Differences in creep strength of material at the interface are also considered as one of the factors for failure [17]. Typically these welds were made using either nickel base filler or austenitic base filler material. When welds were made using nickel filler, type I carbides were found to form along the fusion line which is responsible for cavity formation and growth. On the other hand, in welds made with austenitic filler, failures occurred at prior austenitic grain boundaries at the ferritic heat affected zone (HAZ) away from the fusion line [17].

## 2.3 Creep ruptures behavior and deformation mechanism of base metal (P91), similar metal welds (P91-P91) and dissimilar metal welds

### 2.3.1 Base metal (P91)

Data with regard to the creep properties of P91 steel are reported by various workers [29–32]. Kloc et al. [29] conducted short-term creep tests on P91 base metal at temperatures between 873 to 923 K and at stress levels below 100 MPa. The steady state creep rates were found to correspond to viscous behavior and the apparent stress exponent was found to be close to 1. Ule et al. [30] studied the creep properties of P91 in the temperature range between 873 to 923 K and stress range between 125 to 250 MPa.

They found the stress exponent value ($n$) to be 5.5, and the apparent activation energy was stress dependent. Spigarelli et al. [31] performed tests between 848 to 923 K and 85 to 250 MPa, and the obtained stress exponent ‘n’ in the range of 9 to 14, suggesting dislocation climb as a creep mechanism. Choudary et al. [32] studied the creep behavior of P91 at 823, 848, and 873 K and 125 to 275 MPa and found the stress dependence of minimum creep rate on Norton’s power law with a stress exponent ‘n’ of approximately 12. Shreshta et al. [33] studied the creep behavior of P91 base metal in a wider stress regime (35–350 MPa) and in the temperature range of 873–1023 K and found the rate controlling creep deformation mechanism to be the climb of edge dislocation with a stress exponent of $n = 5$ after incorporating threshold stress.

### 2.3.2 Similar metal welds (P91-P91)

The creep failure of P91 similar metal welds was found to be in the HAZ of the weldment. Kumar et al. [34] studied the creep crack growth rate in P91 welds and found it to be higher in the HAZ than the weld metal attributed to the combined effect of high constraint situation and high creep strain while Ogata et al. [35] found it to be because of the triaxial stress state resulting in failure of the specimens. Creep failure was found [36] to be localized in the finer grain heat affected zone (FGHAZ). The finer grains in FGHAZ led to higher rate of recovery of dislocations and coarsening of the sub-grain structure, which eventually led to lower creep resistance. Low temperature friction stir welding of P91 [37] was found to be beneficial in reducing the HAZ damage.

### 2.3.3 Dissimilar metal welds

There are applications involving welding of 2.25 Cr-1Mo steels (P22) to modified 9Cr-1Mo steel (P91) [38] which are found to be affected by the microstructural instabilities and fail at the weld interface [39–41]. The reason cited is carbon redistribution from the low to higher alloy steel which takes place during exposure to high temperatures. This redistribution leads to the formation of a carbon depleted region in the low Cr steel resulting in creep failures [42–46].

The dissimilar metal weld between P91 and 347H which experienced a service life of about 105,000 hours at steam pressure of 12.5 MPa and 813 K temperature was examined for its microstructural changes [47]. The degree of degradation of the microstructure of base materials and HAZ on the 347H steel side was insignificant while P91 HAZ experienced most of the damage. The degradation was confined to FGHAZ characterized by complete decomposition of martensite lath structure into ferrite microstructure. Dissimilar weld joint between P91 and 316LN SS failed at relatively lower stresses at the weld interface compared to P91 base metal and P91 similar metal weld due to the formation of secondary phase, Z-phase in the intercritical heat affected zone (ICHAZ) region [48]. Fatigue crack growth properties of dissimilar metal weld between P91 steel and SS 316L(N) for applications in the prototype fast breeder were studied [49] and found to be influenced by the fatigue crack closure and dynamic strain aging.

## 2.4 Summary

Coal-based thermal power plants are generally designed to last for about 25 years with minimum modifications. It is not uncommon to extend the life of these plants to 40

years by refurbishing and upgrading the power plant parts [50]. P91 steel is designed to withstand these life cycles. However, both similar and dissimilar welds made of this material are found to exhibit lower creep life compared to the base metal. The main reasons cited for these failures are the difference in the coefficient of thermal expansion (CTE) between ferritic and austenitic stainless steel and carbon migration from ferritic to austenitic steel. Most of the workers reported failure of P91 similar welds to take place in the HAZ attributed to various factors such as triaxial stress, fine grain size, coarsening of the sub-grain structure, and Cr-rich carbide particles. The failures of P91 dissimilar metal welds with austenitic stainless steels were found to be at the weld interface and were attributed to the microstructural instabilities such as the carbon-denuded zone, and complete decomposition of martensite lath structure into ferrite microstructure. The background work suggests that a modified approach is required to address the problem of premature failures of dissimilar metal welds between modified Cr-Mo steel and austenitic stainless steel.

## 2.5 References

[1] J. Hilkes, V. Gross, Welding CrMo steels for power generation and petrochemical applications - past , present and future creep resistant CrMo steels, Biul. Inst. Spaw. (2013) 11–22.

[2] D.R. Harries, R.L. Klueh, Physical metallurgy of high-chromium steels, in: High chromium ferritic martensitic steels nuclear application. (2001) 28–38.

[3] K. Maruyama, K. Sawada, J. Koike, Strengthening mechanisms of creep resistant tempered martensitic steel, Isij Int. 41 (2001) 641–653.

[4] F. Abe, Precipitate design for creep strengthening of 9% Cr tempered martensitic steel for ultra-supercritical power plants, Sci. Technol. Adv. Mater. 9 (2008) 013002. doi:10.1088/1468-6996/9/1/013002.

[5] T. Shrestha, Creep deformation, rupture analysis, heat treatment, and residual

stress measurement of monolithic and welded grade 91 steel for power plant components presented in partial fulfillment of the requirements for the degree of doctor of philosophy, 2013.

[6] J.M. Race, Carbon diffusion across dissimilar steel welds, 1992.

[7] V.K. Gouda, M.M. Nassrallah, S.M. Sayed, N.H. Gerges, Failure of boiler tubes in power plants, Br. Corros. J. 16 (1981) 25–31. doi:10.1179/bcj.1981.16.1.25.

[8] http://www.specialmetals.com/assets/documents/alloys/inconel/inconel-alloy-600.pdf.

[9] H.Y. Zhang, S.H. Zhang, M. Cheng, Z.X. Li, Deformation characteristics of δ phase in the delta-processed inconel 718 alloy, Mater. Charact. 61 (2010) 49–53.

[10] F. Liu, X. Lin, G. Yang, M. Song, J. Chen, W. Huang, Microstructure and residual stress of laser rapid formed inconel 718 nickel-base superalloy, Opt. Laser Technol. 43 (2011) 208–213.

[11] S.K. Rai, A. Kumar, V. Shankar, T. Jayakumar, B.R. K. Bhanu Sankara Rao, Characterization of microstructures in inconel 625 using X-ray diffraction peak broadening and lattice parameter measurements, Scr. Mater. 51 (2004) 59–63.

[12] N.D. Evans, P.J. Maziasz, J.P. Shingledecker, Y. Yamamoto, Microstructure evolution of alloy 625 foil and sheet during creep at 750 °C, Mater. Sci. Eng. A. 498 (2008) 412–420.

[13] R. Rodriguez, R.W. Hayes, P.B. Berbon, E.J. Lavernia, Tensile and creep behavior of cryomilled inconel 625, Acta Mater. 51 (2003) 911–929.

[14] M.D. Mathew, K.B.S. Rao, S.L. Mannan, Creep properties of service-exposed alloy 625 after re-solution annealing treatment, Mater. Sci. Eng. A. 372 (2004) 327–333.

[15] http://www.specialmetals.com/assets/documents/alloys/incoloy/incoloy-alloys-800h-800ht.pdf.

[16] K. Laha, K.S. Chandravathi, P. Parameswaran, S. Goyal, M.D. Mathew, A comparison of creep rupture strength of ferritic/austenitic dissimilar weld joints of different grades of Cr-Mo ferritic steels, Metall. Mater. Trans. A Phys. Metall. Mater. Sci. 43 (2012) 1174–1186. doi:10.1007/s11661-011-0957-8.

[17] J.N. Dupont, R.E. Mizia, Review of dissimilar metal welding for the NGNP helical-coil steam generator, 2010. doi:INL/EXT-10-18459.

[18] C.D. Lundin, Dissimilar metal welds—transition joints literature review, Weld. J. (1982) 58s–63s.

[19] A.K. Bhaduri, Transition metal joints for steam generatore-an overview, Int. J. Press. Vessel. Pip. 58 (1994) 251–265.

[20] Y.Y. You, R.K. Shiue, R.H. Shiue, C. Chen, The study of carbon migration in dissimilar welding of the modified 9Cr-1Mo steel, J. Mater. Sci. Lett. 20 (2001) 1429–1432. doi:10.1023/A:1011616232396.

[21] J.F. Eckel, Diffusion across dissimilar metal joints, Weld. J. 43 (1964) 170s–178s.

[22] J.A. Williams, Residual stresses in austenitic-ferritic transition joints fabricated with austenitic weld metal, High Temp. Technol. 2 (1984) 135–140.

[23] H.Y. Lee, S.H. Lee, J.B. Kim, J.H. Lee, Creep-fatigue damage for a structure with dissimilar metal welds of modified 9Cr-1Mo steel and 316L stainless steel, Int. J. Fatigue. 29 (2007) 1868–1879. doi:10.1016/j.ijfatigue.2007.02.009.

[24] S.L. Mannan, D.H. Sastry, K. Laha, K.S. Chandravathi, K.B.S. Rao, An assessment of creep deformation and fracture behavior of 2.25Cr-1Mo similar and dissimilar weld joints, Metall. Mater. Trans. A Phys. Metall. Mater. Sci. 32 (2001) 115–124.

[25] J.D. Parker, G.C. Stratford, Characterisation of microstructures in nickel based transition joints, J. Mater. Sci. 35 (2000) 4099–4107.

[26] Y. Gong, J. Cao, L.N. Ji, C. Yang, C. Yao, Z.G. Yang, Assessment of creep rupture properties for dissimilar steels welded joints between T92 and HR3C, Fatigue Fract. Eng. Mater. Struct. 34 (2011) 83–96. doi:10.1111/j.1460-2695.2010.01496.x.

[27] R.J. Christoffel, M.R. Curran, Carbon migration in welded joints at elevated temperatures, Weld. J. 35 (1956) 457s–468s.

[28] F. Gauzzi, S. Missori, Microstructural transformations in austenitic-ferritic transition joints, J. Mater. Sci. 23 (1988) 782–789.

[29] L. Kloc, V. Sklenička, Transition from power-law to viscous creep behaviour of P91 type heat-resistant steel, Mater. Sci. Eng. A. 234–236 (1997) 962–965. doi:10.1016/S0921-5093(97)00364-X.

[30] B. Ule, A. Nagode, A model based creep equation for 9Cr–1Mo–0.2V (P91 type) steel, Mater. Sci. Technol. 23 (2007) 1367–1374.

[31] S. Spigarelli, E. Cerri, P. Bianchi, E. Evangelisa, Interpretation of creep behaviour of a 9Cr-Mo-Nb-V-N steel using threshold stress concept, Mater. Sci. Technol. 15 (1999) 1433–1440.

[32] B.K. Choudhary, E. Isaac Samuel, Creep behaviour of modified 9Cr-1Mo ferritic steel, J. Nucl. Mater. 412 (2011) 82–89. doi:10.1016/j.jnucmat.2011.02.024.

[33] T. Shrestha, M. Basirat, I. Charit, G.P. Potirniche, K.K. Rink, U. Sahaym, Creep deformation mechanisms in modified 9Cr-1Mo steel, J. Nucl. Mater. 423 (2012) 110–119. doi:10.1016/j.jnucmat.2012.01.005.

[34] Y. Kumar, S. Venugopal, G. Sasikala, S.K. Albert, A.K. Bhaduri, Study of creep crack growth in a modified 9Cr–1Mo steel weld metal and heat affected zone, Mater. Sci. Eng. A. 655 (2016) 300–309.

[35] T. Ogata, T. Sakai, M. Yaguchi, Damage assessment method of P91 steel welded tube under internal pressure creep based on void growth simulation, Int. J. Press. Vessel. Pip. 87 (2010) 611–616. doi:10.1016/j.ijpvp.2010.08.009.

[36] M.E. Abd El-Azim, O.H. Ibrahim, O.E. El-Desoky, Long term creep behaviour of welded joints of P91 steel at 650℃, Mater. Sci. Eng. A. 560 (2013) 678–684. doi:10.1016/j.msea.2012.10.013.

[37] P. Rao, J. Akram, M. Misra, Low temperature frictions stir welding of P91 steel, Def. Technol. (2015). doi:10.1016/j.dt.2015.11.003.

[38] V. Moorthy, S. Vaidyanathan, K. Laha, T. Jayakumar, K. Bhanu Sankara Rao, B. Raj, Evaluation of microstructures in 2.25Cr-1Mo and 9Cr-1Mo steel weldments using magnetic Barkhausen noise, Mater. Sci. Eng. A. 231 (1997) 98–104.

[39] P. Seliger, A. Thomas, High temperature behaviour of similar and dissimilar welded components of steel grade P22 and P91, in: 5th Int. Conf. Mech. Mater. Des. (2006) 1–9.

[40] C. Sudha, V.T. Paul, A.L.E. Terrance, S. Saroja, M. Vijayalakshmi, Microstructure and microchemistry of hard zone in dissimilar weldments of Cr-Mo steels, Weld. J. 85 (2006) 71s–80s.

[41] C. Sudha, A.L.E. Terrance, S.K. Albert, M. Vijayalakshmi, Systematic study of formation of soft and hard zones in the dissimilar weldments of Cr–Mo steels, J. Nucl. Mater. 302 (2002) 193–205.

[42] J. M Race & H. K. D. H. Bhadeshia, Precipitation sequences during carburisation of Cr-Mo steel, Mater. Sci. Technol. 8 (1992) 875–882.

[43] D. Jandová, J. Kasl, A. Rek, Electron microscopy and microanalysis of steel weld joints after long time exposures at high temperatures, IOP Conf. Ser. Mater. Sci. Eng. 7 (2010) 1–10. doi:10.1088/1757-899X/7/1/012012.

[44] S.K. Albert, T.P.S. Gill, A.K.Tyagi, S.L. Mannan, S.D.Kulkarni, P.Roderiguez, Soft zone formation in dissimilar welds between two Cr-Mo steels, Weld. J. 76 (1997) 135–142.

[45] L. Střílková, Z. Kuboň, V. Vodárek, Evaluation of local mechanical properties in P23/P91 dissimilar welds after creep exposure at 500-600 °C, Chem. List. 105

(2011) s848–s849.

[46] V. Vodárek, L. Střílková, Z. Kuboň, Creep behaviour and microstructure of a heterogeneous P23/P91 weld, in: Metals (Basel). (2009) 129–135.

[47] A. Zielinski, G. Golanski, P. Urbanczyk, J. Slania, J. Jasak, Microstructure and properties of dissimilar welded joint between P91 and TP347HFG steels after 105000 h service, Pr. IMZ. 1 (2015) 37–43.

[48] P. Parameswaran, K. Laha, Role of microstructure on creep rupture behaviour of similar and dissimilar joints of modified 9Cr-1Mo steel, Procedia Eng. 55 (2013) 438–442. doi:10.1016/j.proeng.2013.03.277.

[49] M. Nani Babu, G. Sasikala, Fatigue crack growth behavior of ferritic and austenitic steels at elevated temperatures, Mater. Perform. Charact. 3 (2014) 182–209. doi:http://dx.doi.org/10.1520/MPC20130055.

[50] International Energy Agency, Life extension of coal-fired power plants, 2005. http://www.iea-coal.org.uk/documents/81405/5990/Life-extension-of-coal-fired-power-plants.

# CHAPTER 3

# DEVELOPMENT, METALLURGICAL CHARACTERIZATION, AND MODELING OF WELD TRANSITION JOINTS

The major aim of this research work is to develop the weld transition joints between modified 9Cr-1Mo steel (P91) and austenitic stainless steel (AISI 304) with different Ni-based alloy interlayers and study its creep properties. These joints are useful for boiler tube applications which experience temperatures around 873 K. The approach adopted in this research work to develop such transition joints is solid state coating and welding methods. This is in contrast to the conventional approach of applying fusion-based welding methods. In this work, friction surfaced coating method and friction welding method was applied to develop Ni-based alloy interlayers between P91 and AISI 304. In this chapter, experimental details and results and discussion pertaining to the development of these joints and their metallurgical characterization are presented. It also describes the results of modeling work to describe the microstructural evolution in these joints. Section 3.1 consists of development and characterization of weld transition joint by friction surfacing method and most of the content from this section is adopted from our published work [1–4].

## 3.1 Development and characterization of weld transition joints by friction surfacing

In friction surfacing process, the rotating consumable rod moves in linear direction relative to the substrate under the action of vertical applied load as shown in Figure 3.1**.** Frictional heat is generated between the consumable rod and substrate material due to rubbing action. Frictional heat assisted with axial pressure makes the plasticized metal flow outwards.

During this process, the oxide layer which is sheared off due to severe plastic deformation is also expelled out along with the flash. The layers of plasticized metal thus sheared away from the consumable rod get coated on to the substrate by the large axial force. The combined effect of the axial force and the shear force generated due to transverse movement of the substrate initiates the detachment of a layer of material from the face of the consumable rod. As no melting of substrate or coating rod takes place, the coating thus formed is a solid phase coating. Being solid state, friction surfaced coatings are free from cracks, tensile residual stresses, inclusions, porosity, lack of fusion, dilution, coarser columnar grains, microsegregation of elements, and phase transformations.

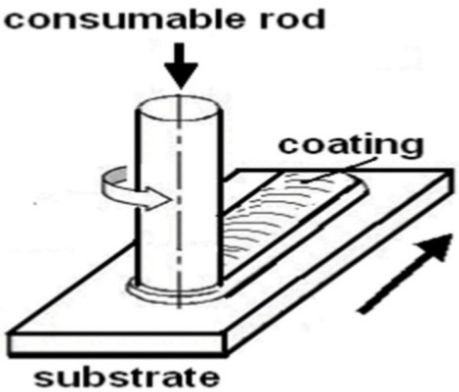


Figure 3.1 Schematic of friction surface coating process.

### 3.1.1 Study on effect of process parameters on friction surfaced coating dimensions

#### 3.1.1.1 Materials and experimental methods

Carbon steel-AISI 1012 (wt% 0.12 C, 0.40Mn, 0.02 P, 0.01 S, and balance Fe), austenitic stainless steel- AISI 304 (0.08 C, Cr 17.75, Ni 7.70, Mn 1.17, Si 0.77, and balance Fe), and Inconel 718 (51.60 Ni, 18.2 Cr, 5.10Nb, 3.28 Mo, 1.06 Ti, 0.56 Al, 0.33 V, 0.09Mn, 0.01 S, 0.004 C, 0.003 B, and 19.76 Fe) were used as materials. Dimension of the substrate was 150×150×2 mm. The diameter of circular consumable rods (henceforth referred to as rods) was 19 mm for carbon steel and AISI 304 and 12.5 mm for Inconel 718. Friction stir welding machine was used to generate coatings as shown in Figure 3.2 (model-RM1, manufacturer-MTI (Manufacturing Technology, Inc.)). The parameters used are as follows: rotational speed ranges from 1000 to 2000 RPM, feed rate ranges from 50 to 150 mm/min, axial load ranges from 3 to 12 kN, and dwell time of 5s. The substrate plate was clamped firmly. The dimensions (width, height) of the coatings were measured by Vernier calipers.

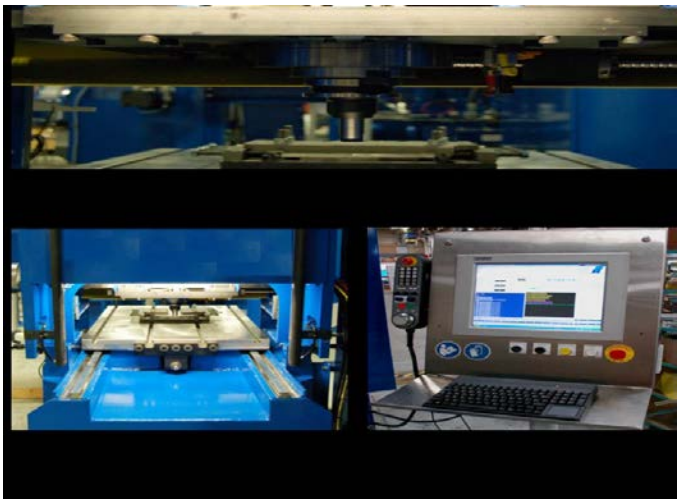

Figure 3.2 Photographs of friction stir welding machine.

3.1.1.2 Results and discussion

Four combinations of materials were used to study the effect of rotational speed (RPM) of consumable rod: 1) Steel over Steel substrate, 2) Steel over Stainless steel substrate, 3) Stainless steel over Stainless steel substrate, and 4) Inconel 718 over Stainless steel. RPM was varied from 1000 to 2000 RPM, while keeping axial force (8000 N), feed rate (100 mm/min), and dwell time (10 s) constant. Table 3.1 shows the thickness and width of coatings with the variation of RPM.

It can be seen that achieved load was found to be different than applied load depending on high temperature strength of rod. For example, steel over steel showed lower than 8000 N, steel over stainless steel showed intermediate value, stainless steel over stainless steel showed close to 8000 N, whereas Inconel 718 showed the same value as applied. Typical coatings made are shown in Figure 3.3. For clarity, the same results are shown in Figure 3.4 to show the trend more clearly.

It can be seen from Table 3.1 that the rotational speed significantly affected both the coating width and thickness. The coating width and thickness decreased with increased RPM. Therefore, it can be concluded that the coating width and thickness are a function of rotational speed. This could be attributed to the actual contact area between the consumable rod and the substrate during the friction surfacing process. It shows that the real contact area and therefore the metal transfer area decreases with increase in rotational speed of the consumable rod resulting in narrower coatings. Interestingly, the achieved load was found to be increased with increased RPM in all the cases. The increased load at higher RPM is due to high rate of flash generation which allows the nascent surface of rod to be in direct contact with the substrate.

Table 3.1 Effect of RPM on the coating dimensions.

| Material | Applied Load, N | Achieved load, N | RPM | Width, mm | Thickness, mm |
|---|---|---|---|---|---|
| Steel coating over Steel | 8000 | 2000 -3000 | 1000 | 24.50 | 3.45 |
| | | 2300 | 1200 | 23.00 | 3.00 |
| | | 2000-3000 | 1600 | 20.50 | 2.45 |
| | | 3000-4000 | 2000 | 20.00 | 1.45 |
| Steel coating over Stainless steel | 8000 | 2000-3000 | 1000 | 23.20 | 3.50 |
| | | 2000-3000 | 1200 | 23.00 | 3.00 |
| | | 4000 | 1600 | 23.00 | 2.50 |
| | | 5000 | 2000 | 21.00 | 1.60 |
| Stainless steel coating over Stainless Steel | 8000 | 6000-7000 | 1000 | 18.3 | 2.00 |
| | | 6000-7000 | 1200 | 16.00 | 1.80 |
| | | 7000-8000 | 1600 | 14.5 | 1.60 |
| | | 7000-8000 | 2000 | 12.5 | 1.00 |
| Inconel 718 over Stainless steel | 8000 | 8000 | 1000 | 10 | 1.00 |
| | | 8000 | 1600 | 8.6 | 0.51 |
| | | 8000 | 2000 | 7.5 | 0.23 |

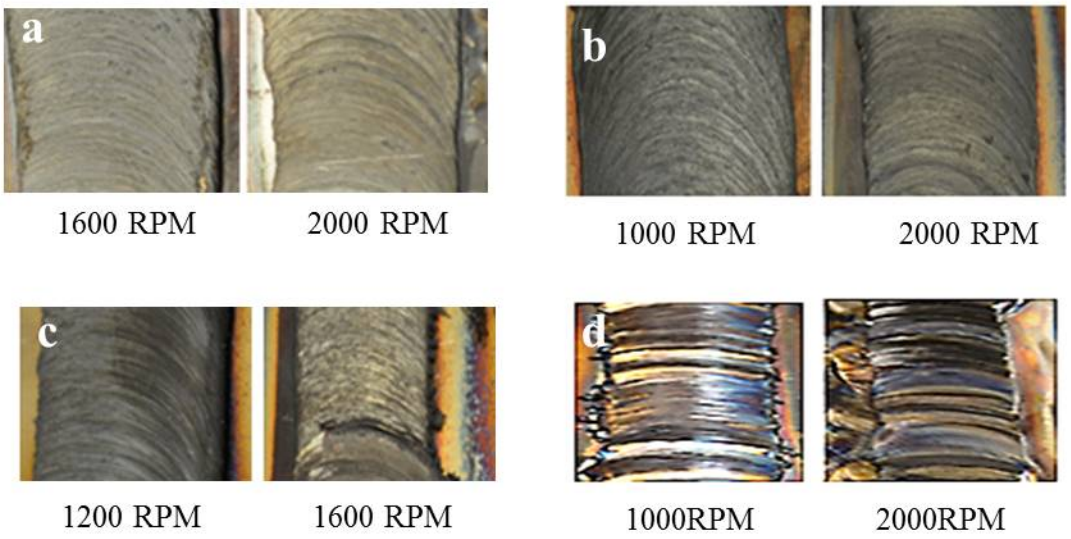


Figure 3.3 Photographs of coatings with different combinations of coating and substrate: (a) steel over steel, (b) steel over stainless steel, (c) stainless steel over stainless steel, and (d) Inconel 718 over stainless steel.

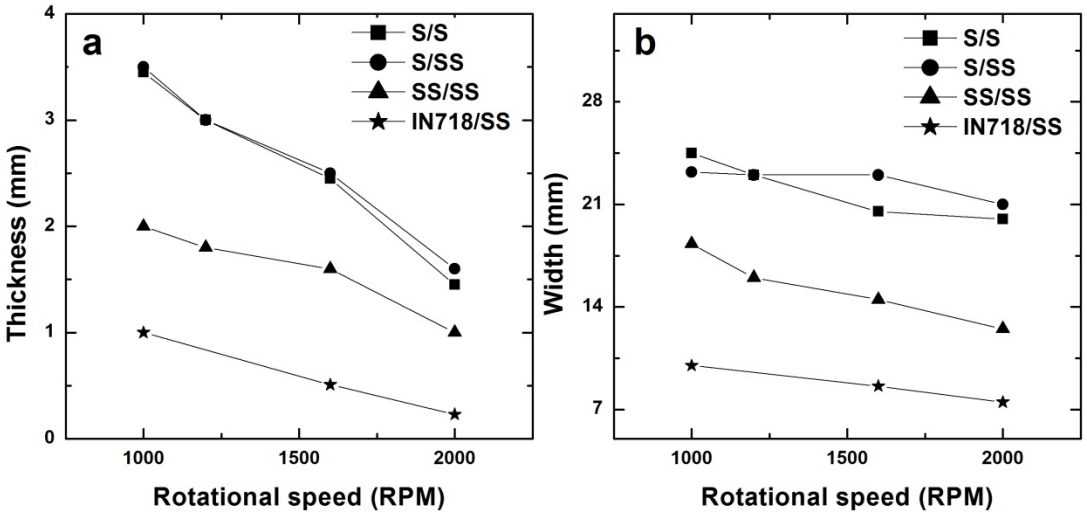


Figure 3.4 Coating thickness (a) and coating width (b) as a function of rotational speed (S/S: steel over steel, S/SS: steel over stainless steel, SS/SS: stainless steel over stainless steel, and IN718/SS: Inconel 718 over stainless steel).

Further, increased load would have resulted in displacement of more plastic material resulting in decreased thickness of coatings. From Table 3.1, it can also be noted that thickness and width values of steel coatings were higher than the stainless steel coatings. This could be attributed to the difference in their high temperature strengths. Carbon steel, due to its lower high temperature strength, deposited thicker and wider coatings than the austenitic stainless steel and Inconel 718. Therefore, apart from process parameters, the dimensions of metallic coatings are also dictated by the rod high temperature strength. It can be noted that the Inconel 718 coating thickness and width values were comparatively lesser than either steel or stainless steel coatings. This could be attributed to the relatively higher values of high temperature strength of Inconel 718 compared to steel and stainless steels. Based on uniformity and smoothness of the coating, the optimum rotational speeds for steel, stainless steel, and Inconel 718 consumable rods were chosen to be 1600 RPM, 1000 RPM, and 1000 RPM, respectively.

Effect of rod feed rate on coating dimensions was studied applying the optimum RPM values found in the earlier section. Applied load (8000 N) and dwell time (10 s) were kept constant. Table 3.2 shows the variation in coating thickness and width with feed rate. Typical coatings made with different rod feed rates are shown in Figure 3.5. For clarity, the same results are shown in Figure 3.6 to show the trend more clearly. The coating thickness decreased with increased feed rate.

The coating width increased with increased feed rate, but not so significantly. For example, when the feed rate increased for stainless steel coating over stainless steel from 50 mm/min to 150 mm/min, thickness decreased from 2.7 to 1.10 mm. When the feed rate increased from 50 mm/min to 150 mm/min, the coating width increased from 18 mm

Table 3.2 Effect of rod feed rate on coating dimensions.

| Material | Applied Load, N | Achieved load, N | Feed Rate (mm/min) | Width, mm | Thickness, mm |
|---|---|---|---|---|---|
| Steel coating over Steel | 8000 | 1000 -2000 | 50 | 20.00 | 2.75 |
| | | 2000-3000 | 100 | 21.00 | 2.45 |
| | | 3000-4000 | 150 | 23.00 | 2.00 |
| Steel coating over Stainless steel | 8000 | 1000-2000 | 50 | 20.00 | 3.00 |
| | | 4000 | 100 | 23.00 | 2.50 |
| | | 6000-7000 | 150 | 25.00 | 1.35 |
| Stainless steel coating over Stainless Steel | 8000 | 3000-4000 | 50 | 18.00 | 2.70 |
| | | 6000-7000 | 100 | 18.30 | 2.00 |
| | | 8000 | 150 | 19.00 | 1.10 |
| Inconel 718 over - Stainless Steel | 8000 | 8000 | 100 | 10 | 1 |
| | | 8000 | 150 | 10.5 | 0.8 |

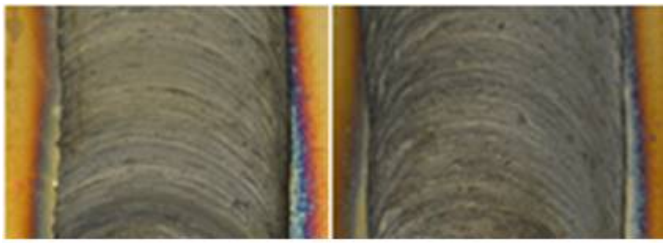


Figure 3.5 Photograph of steel coating over stainless steel as a function of rod feed rate.

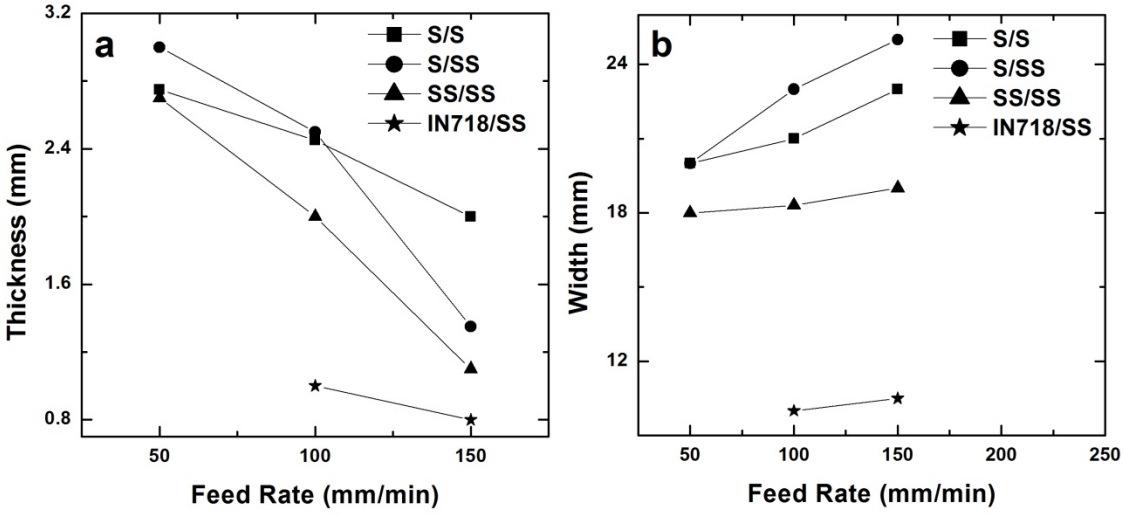


Figure 3.6 Coating thickness (a) and coating width (b) as a function of rod feed rate.

to 19 mm. The decrease in thickness values could be attributed to less available plastic material with increased feed rate. As there is less plastic material available with increased feed rate, it resulted in increased achieved load.

In order to study the effect of applied axial force, only limited studies were conducted using stainless steel and Inconel 718 rods on stainless steel substrate. Stainless steel was coated as button sample and Inconel 718 was coated as full coating. For stainless steel, axial force was varied between 3000-12000 N keeping RPM (1000) and feed rate (60 mm/min) constant whereas for Inconel 718, axial force was varied from 4000 to 12000N, while keeping the feed rate (100 mm/min) and rotational speed (1000 RPM) constant. Table 3.3 and Figure 3.7 show the effect of axial force on coating thickness and width.

Typical coatings obtained with different values of axial force are shown in Figure 3.8. It can be seen that the increased axial force decreased thickness and increased width of coatings in both cases. At lower force, coating was not continuous which can be attributed to the insufficient load to plasticize the material. Excessive force led to thinner and wider coatings due to excessive material expelling from the rubbing end of consumable rod [1].

3.1.1.3 Conclusions

1) The studies showed that process parameters such as consumable rod rotational speed (RPM), and feed rate (mm/min) and axial load (N) play significant role in affecting the metallic coating dimensions using friction surfacing.

2) The rotational speed (RPM) significantly affected both coating width and

Table 3.3 Effect of axial force on coating dimensions.

| Axial force, N | | 3000 | 6000 | 9000 | 12000 |
|---|---|---|---|---|---|
| AISI 304 over AISI 304 | Thickness, mm | 5 | 4.5 | 2.5 | 2.25 |
| | Width, mm | 18 | 19.8 | 20 | 21 |
| Axial force, N | | | 4000 | 8000 | 12000 |
| Inconel 718 over AISI 304 | Thickness, mm | | 1.23 | 1 | 0.64 |
| | Width, mm | | 8 | 10.00 | 10.56 |

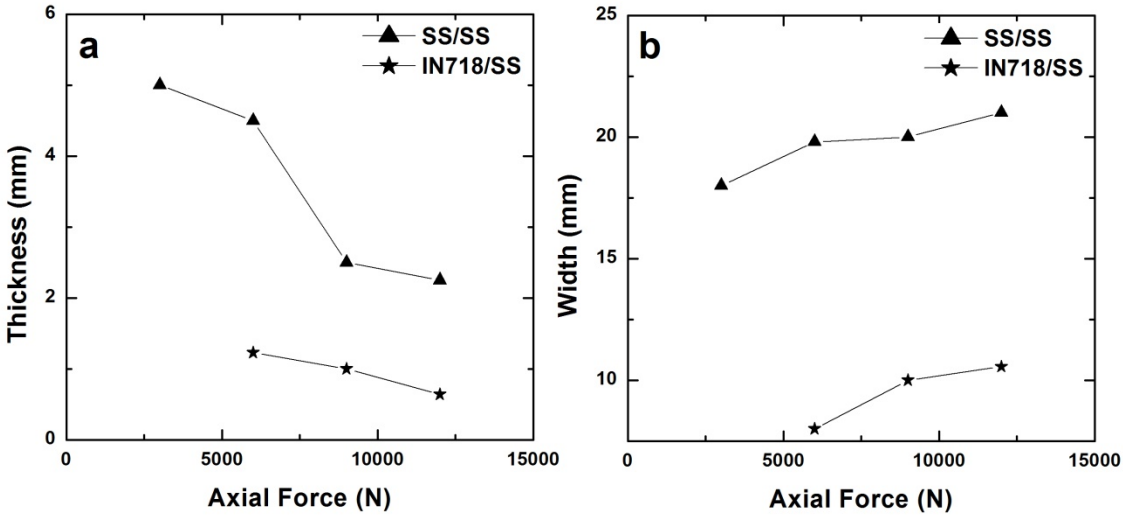


Figure 3.7 Effect of axial force on AISI 304 and Inconel 718 coatings (a) thickness and (b) width.

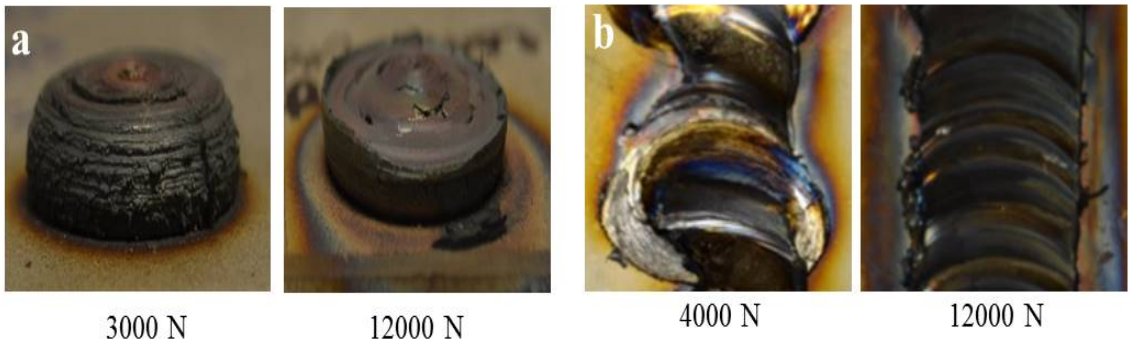


Figure 3.8 Photograph of (a) button coating of stainless steel over stainless steel as a function of axial force (b) full-length coating of Inconel 718 over stainless steel as a function of axial force.

thickness. The coating width decreased with increased RPM. The lowest RPM resulted in thicker coatings.

3) The coating thickness decreased with increased rod feed rate whereas coating width increased with increased rod feed rate.

4) Increased axial force decreased thickness and increased width of coating.

5) The coating dimensions were found to be affected by consumable rod high temperature strength. The higher the high temperature strength of rod, the lower was the coating thickness and width. Inconel 718 showed relatively thinner and narrower coatings than steel and stainless steel coatings.

### 3.1.2 Microstructural characterization of Inconel layers developed by friction surfacing

In this section, based on optimized parameters from the previous section, transition joint was developed between P91-AISI 316 by depositing Ni-based alloy interlayers using friction surfacing. This study mainly focused on the microstructural

characterization of these layers using optical microscopy, scanning electron microscopy (SEM), electron backscattered diffraction (EBSD), and transmission electron microscopy (TEM).

3.1.2.1 Materials and experimental methods

Cr-Mo steel (P91) was taken in a plate form (50×50×125mm) and used as the substrate. Inconel 625, Inconel 718, Inconel 600, and Inconel 800H (12.5 mm diameter) were used to deposit coatings. AISI 316 or 304 rod (12.5 mm diameter) was friction welded to the Inconel 800H. AISI 316 was used for optical and SEM studies and AISI 304 was used for TEM studies. Table 3.4 shows the chemical composition of materials used. The parameters which resulted in good interface bond integrity were selected as follows: rotational speed-1000 rpm, axial force-6000N, and dwell time-30 seconds. The sequence of friction surfaced coatings one over the other on P91 was as follows: Inconel 625, Inconel 718, Inconel 600, Inconel 800H, and AISI 316/304. Surface temperature profiles generated at the rod/substrate interface were recorded using an infrared (IR) camera. The deposited coatings were machined to get a cylindrical rod and a transverse slice was cut by EDM in the length direction of the rod for bend test and microstructural evaluation. The samples were ground, polished, and etched as per standard metallographic practice for microstructural examination. P91 steel was etched using 5% Nital; Inconel layers were etched using solution of 10ml $H_2SO_4$, 10ml HCl, and 10g $CuSO_4$; and AISI 316 stainless steel was electrolytically etched using oxalic acid solution (10 g oxalic acid + 100 ml water, Electrode–Platinum, applied voltage of 6 V, and current density of 1 A/cm$^2$ for 1-2 minutes). Microstructures of friction surfaced coatings were

Table 3.4 Chemical composition of substrate and consumable rods.

| Materials | Composition (in wt%) |
|---|---|
| P91 (substrate) | 0.10%C, 9.23%Cr, 1.14%Mo, 0.30%Ni, 0.30%Si, 0.38%Mn, 0.21%V, and Balance Fe |
| Inconel 625 | 0.03% C, 22.90 %Cr, 0.10% Co, 8.70% Mo, 3.60% Nb, 0.20% Ti, 3.90% Fe and Balance Ni |
| Inconel 718 | 0.004% C, 18.80% Cr, 17.2% Fe, 5.10%Nb, 3.30% Mo, 1.10% Ti, 0.60% Al, and Balance Ni |
| Inconel 600 | 0.05% C, 16.10% Cr, 9.00% Fe, 0.30% Ti, 0.04% Co, 0.03% Nb, and Balance Ni |
| Inconel 800H | 0.07% C, 20.40% Cr, 48.40% Fe, 0.51% Ti, and Balance Ni |
| AISI 316 | 0.08% C, 18.30% Cr, 10.20% Ni, 2.02% Mo, 1.02% Mn, and Balance Fe |
| AISI 304 | 0.08 %C, 17.75% Cr, 7.70% Ni, 1.17% Mn, 0.77% Si, and balance Fe |

examined using optical microscope and SEM. Grain size and Vickers microhardness were measured for coatings and compared with consumable rods. Energy Dispersive Spectroscopy (EDS) was used to determine the chemical composition of friction surfaced coatings near the interface to confirm intermixing. Scanning electron microscope electron backscattered diffraction (SEM-EBSD) studies were carried out on limited samples to study the mechanisms of dynamic recrystallization in the friction surfaced coatings. EBSD studies were conducted using an FEI Quanta-200 scanning electron microscope.

The scan area was 200×200 μm at a step size of 0.5 μm. TSL-OIM software was used for electron backscattered diffraction analysis. For TEM analysis, samples were extracted from individual layers of weld transition joint. The consumable rods and coated samples were cut using a low speed saw to a thickness of 0.6 mm to 0.8 mm. The specimens were ground to a thickness of 100 microns using SiC papers. The thin foils thus made were thoroughly washed in alcohol and ultrasonically cleaned in acetone for a sufficient amount of time. Using a disc punch, 3 mm diameter discs were extracted. The discs were ultrasonically cleaned in alcohol and thinned by jet polishing. Final sample preparation was carried out in an automatic twin-jet electro-polisher which uses two jets to direct electrolyte flow onto the specimen, which simultaneously thins and polishes both sides. Mixture of methanol and 10% perchloric acid was used as electrolyte for all specimens. As a specimen is thinned and finally forms a hole at the center of the specimen, light is transmitted to the sensor indicating completion of polishing by an alarm. Table 3.5 gives the conditions for electro-polishing of different alloys used in the study.

Table 3.5 Electro-polishing conditions used for the specimens*.

| Sample | Voltage (V) | Current (mA) | Temperature (K) |
|---|---|---|---|
| Inconel 625 | 12 to 15 | 10-12 | 243 to 233 |
| Inconel 600 | 12 to15 | 12 -14 | 243 to 233 |
| Inconel 800H | 12 to 15 | 12 -14 | 243 to 233 |
| AISI 304 | 12 to 15 | 14-16 | 253 to 243 |
| P91 | 18 to 20 | 40-50 | 223 to 203 |

*Electrolyte: 10% perchloric acid + methanol

A transmission electron microscope (TEM), FEI Tecnai F2 operated at 200 kV, was used to characterize the coated samples and consumable rods. Second phase particles were characterized using EDS equipped with the TEM.

3.1.2.2 Results and discussion

3.1.2.2.1 Characterization by optical and scanning electron microscope

The interfaces of the friction surfaced coatings and the substrates are shown in Figure 3.9. Complete bonding without any voids and cracks at the coating interfaces were noticed. The U-bend test showed no de-bonding between the successive coating layers. EDS spot analysis is shown in Table 3.6, corresponding to points shown in Figure 3.9. The EDS results showed almost negligible dilution near the interfaces. Friction surfacing does not involve any melting and solidification during deposition of the coating materials which makes coatings free from dilution with the substrate materials. Friction surfaced coatings showed equiaxed fine grained microstructures in contrast to their consumable rod counterparts (Figure 3.10). The corresponding grain sizes in μm are as follows: Inconel 625 (rod 11.8±4.9; coating 3.6±0.8); Inconel 718 (67.4±4.4; 18.8±1.2); Inconel 600 (62.8±8.4; 12.4±2.2); Inconel 800H (84.4±10.2; 12.8±4.0); and AISI 316 (48.3±7.8; 14.6±1.4). Significant reduction in the grain size of friction surfaced coatings compared with their consumable rod counterparts is an indication that the friction surfaced coatings are subjected to dynamic recrystallization. This is in line with earlier studies [5–9]. High strain rates and temperatures involved in these friction-based process result in the dynamic recrystallization and grain refinement. Relatively high strain rates (>400 $S^{-1}$) and temperatures (0.8–0.9$T_m$) are reported for the friction surfaced coatings [5,6,10].

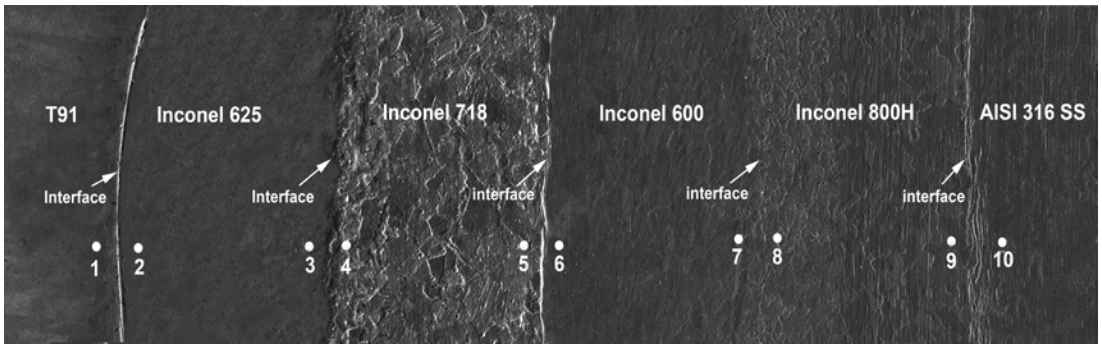


Figure 3.9 Montage of P91/ AISI 316 transition joint with various friction surfaced Inconel alloy interlayers.

Table 3.6 EDS spot analysis of friction surfaced interlayers.

| Element | Spectrum Location (Elements are in wt%) | | | | | | | | | |
|---|---|---|---|---|---|---|---|---|---|---|
| | P91 | Inconel 625 | | Inconel 718 | | Inconel 600 | | Inconel 800H | | AISI 316 SS |
| | 1 | 2 | 3 | 4 | 5 | 10 | 7 | 8 | 9 | 10 |
| Cr | 9.2 | 22.8 | 23.0 | 18.9 | 18.8 | 18.2 | 16.4 | 20.6 | 21.4 | 18.2 |
| Fe | 89.0 | 3.7 | 3.4 | 17.2 | 17.1 | 68.7 | 8.1 | 48.4 | 48.9 | 68.7 |
| Ni | - | 59.2 | 60.2 | 52 | 52.2 | 9.8 | 75.0 | 30.1 | 28.8 | 9.8 |
| Nb | - | 3.8 | 3.6 | 5.1 | 5.0 | -- | -- | -- | -- | -- |

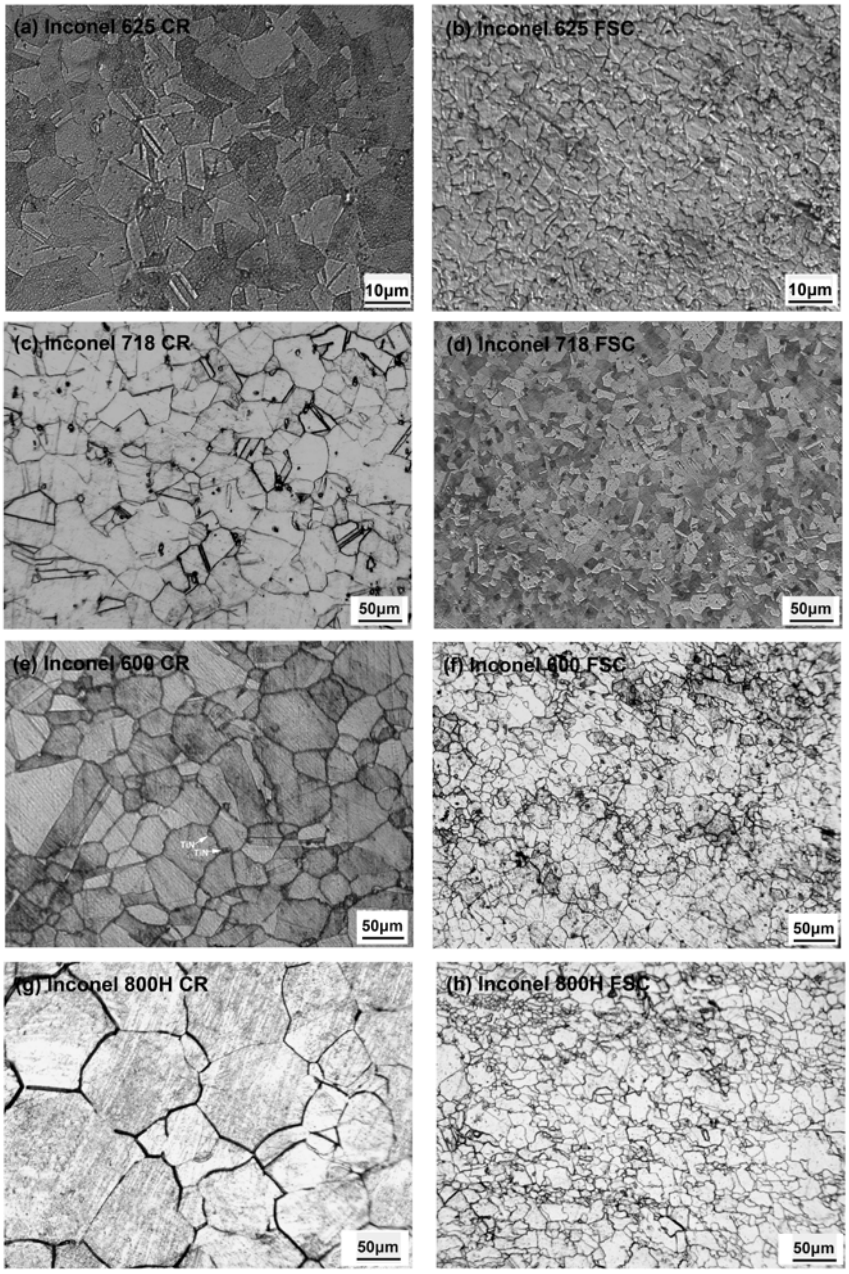


Figure 3.10 Optical micrographs of consumable rods (CR) and their friction surfaced coatings (FSC).

The temperatures recorded in this study using IR camera (Figure 3.11) showed that the temperature attained at the interface between the Inconel 600 rod and the Inconel 718 substrate was about 1373 K. These severe plastic deformation conditions promote nucleation and growth of a new set of grains at prior deformed grain boundaries which eventually produce grain refinement. Different hot restoration mechanisms such as dynamic recovery and dynamic recrystallization are responsible for the grain refinement in friction surfaced coating materials. Stacking fault energy of the processed material plays a vital role in deciding the type of hot restoration mechanism. Dynamic recovery processes are slow in low or medium stacking fault energy materials such as copper, nickel, and austenitic iron. Dynamic recrystallization may take place in these materials when a critical deformation condition is reached [11]. In the present work, nickel-based alloys are friction surfaced to develop a transition joint between P91 and AISI 316. Nickel-based alloys have medium stacking fault energy ($\approx$ 128 $mJm^{-2}$), therefore, dynamic recrystallization is the hot restoration mechanism in the present case.

Grain size of friction surfaced coatings was found to change from top to bottom and is in line with earlier works [6]. The large size grains are observed near the top surface of the coating compared with its bottom surface. A difference of about 40% in the grain size was observed from top surface to bottom surface of different Ni-based alloy coatings and AISI 316 friction surfaced coatings. The difference in the grain size across the cross-section of coatings can be attributed to the difference in cooling rates experienced by the friction surfaced coatings. Further, it is observed that fresh depositions during multiple layer build-ups did not cause noticeable coarsening of grains in the previously deposited layers indicating that temperatures and cooling rates involved

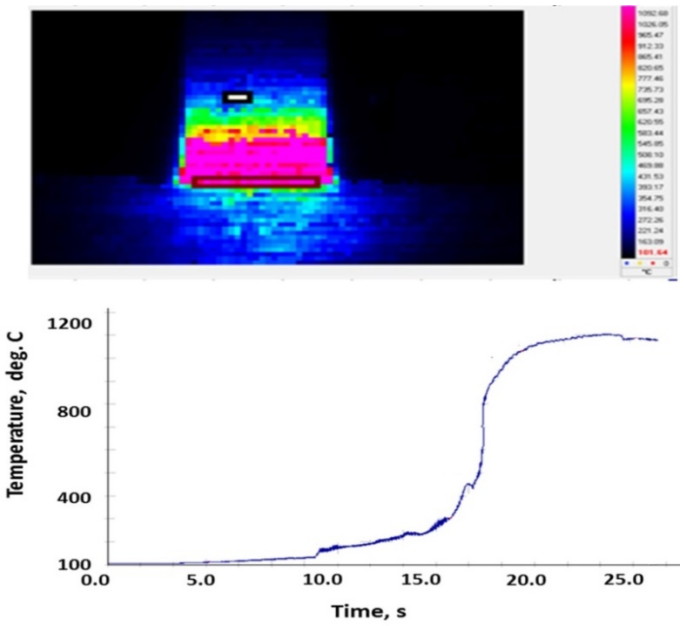


Figure 3.11 Screen shot of temperature profile generated by IR camera during friction surfacing (Consumable rod: Inconel 600 friction and substrate: Inconel 718).

in friction surfacing will not lead to significant microstructural changes in the substrate.

It is further observed that friction surfaced coatings of Ni-based alloy alloys showed decrease in density of twin boundaries compared to the consumable rod counterparts as shown in Figure 3.10. The decrease in the density of twin boundaries can be attributed to involvement of high processing temperatures and high strain rates in these friction-based processes. It is also noteworthy that the initial grain size of the consumable rod does not affect the grain refinement in friction surfaced coatings. Average microhardness values of rods and friction surfaced coatings (near the top surface) are found to be as follows: Inconel 625 (rod 285±10; coating 348±15); Inconel 718 (310±5; 370±15); Inconel 600 (190 ±10; 240±10); Inconel 800H (150±8; 215±12); and AISI 316 (210±10; 268±15). In all these cases, friction surfaced coatings showed higher hardness than their consumable rods. The gain in hardness of friction surfaced

coatings can be attributed to finer grain size in friction surfaced coatings compared with their consumable rods [2,4].

3.1.2.2.2 Characterization by transmission electron microscope

AISI 304 base metal rod was obtained in mill annealed condition. Using optical metallography, the grain size of the base metal rod was measured to be around 50 ± 10 μm. Thin foil specimens after jet polishing were directly examined in the TEM. Figure 3.12 shows the TEM micrograph of the AISI 304 base metal rod. The micrograph reveals a typical grain boundary triple point and annealing twins within the grain. Being one of the most important kinds of special boundaries, annealing twin boundaries affect many properties in a large variety of materials [12]. In friction surfaced coatings of AISI 304, the grain size was found to be finer than their consumable rod counterparts. TEM studies showed dynamic recrystallization (DRX) driven by the strain energy stored in the material during processing [13].

P91 base metal was normalized at 1323 K/1h and tempered at 1023 K/2h and air cooled. TEM samples after jet polishing were carefully preserved in methanol to avoid atmospheric corrosion of the thinned edge. Samples were dried before examination in the TEM. Figure 3.13 shows the TEM micrograph of P91 sample. The micrograph reveals typical lath morphology of martensite. Carbide particles were seen to decorate the martensite lath boundaries. Several works reported these dark particles to be predominantly $M_{23}C_6$ type carbides [14,15]. EDS analysis showed that the finer particles appearing in the subgrain interior were carbides or carbonitrides such as NbC, Nb(C, N), $Nb_2C$, MoC, and $Mo_2C$.

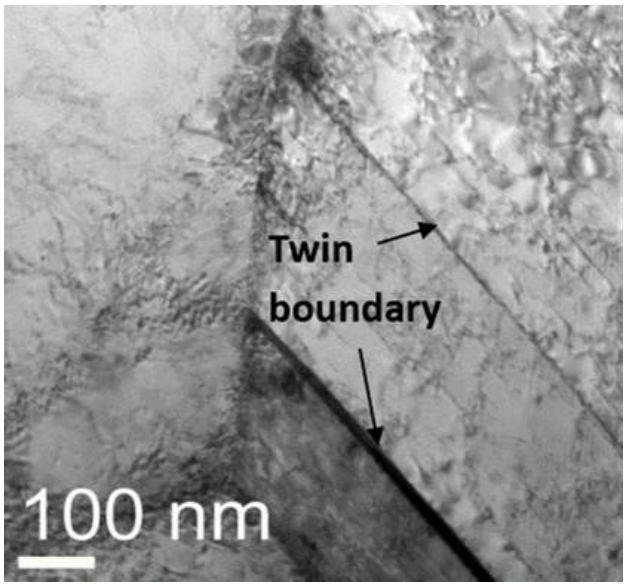


Figure 3.12 AISI 304 base metal rod in mill annealed condition.

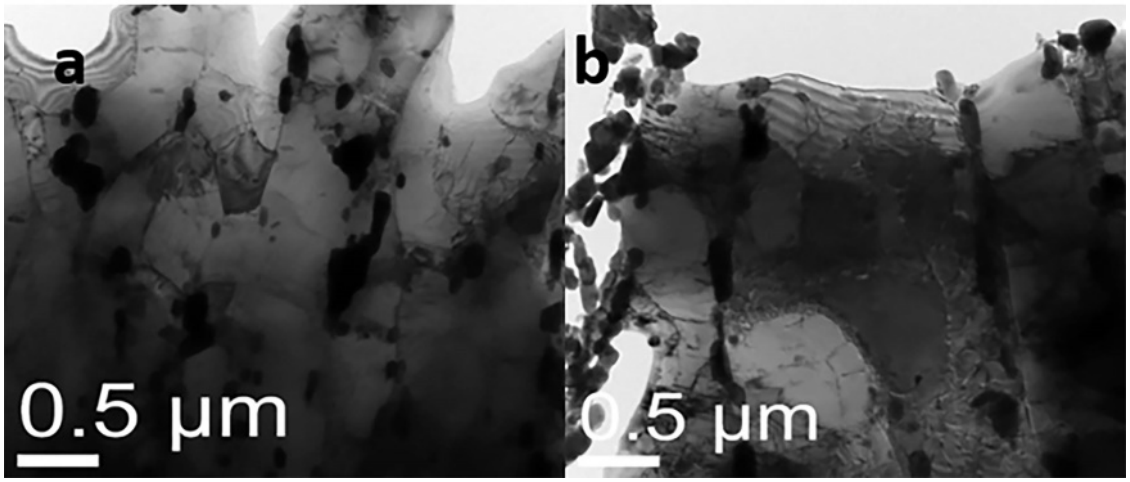


Figure 3.13 P91 base material in normalized and tempered condition: (a) and (b) showing lath morphology of martensite and carbides along the lath boundaries.

Using optical metallography, the grain size of the Inconel 600 consumable rod was measured to be around 15 ± 8 μm in the as-received condition. Figure 3.14a shows the TEM micrograph of the Inconel 600 rod which revealed a coarse carbide network of particles. These particles were on the grain boundaries of austenite. Average size of the intergranular precipitates was 275 to 300 nm, and the precipitates were observed on random high angle grain boundaries. The carbide morphology was continuous and branching into the grains of austenite. EDS results as shown in Figure 3.14b indicated the particles to be predominantly chromium carbides. Though Inconel 600 is considered to be a solid-solution alloy with austenite matrix, several types of carbides can form depending on heat treatment conditions. The precipitated phases in the matrix after heat treatment are reported to be carbides such as chromium carbides, titanium carbides, and titanium nitrides [16]. The grain boundary carbides after ageing were found to be $Cr_7C_3$ type, whereas within the grain they were found to be $Cr_{23}C_6$ [17].

The friction surfaced coating of Inconel 600 showed (Figure 3.15a) fine particles in the matrix of austenite. The coarse carbide particles which were observed in the consumable rod decreased to ~ 50 nm in the coating. Friction surfacing is a severe plastic deformation process and causes fracture and fragmentation of secondary particles originally present in the consumable rod resulting in fine particles. Figure 3.15b and Figure 3.15c show high resolution images of a secondary particle.

The grain size of the as-received consumable rod of Inconel 625 was 12 ± 5 μm. TEM microstructure (Figure 3.16a) showed that the rod structure was characterized by the presence of fine carbide particles in an austenite matrix. These carbides were analyzed using EDS and were found to be rich in Nb, Ti, and Mo.

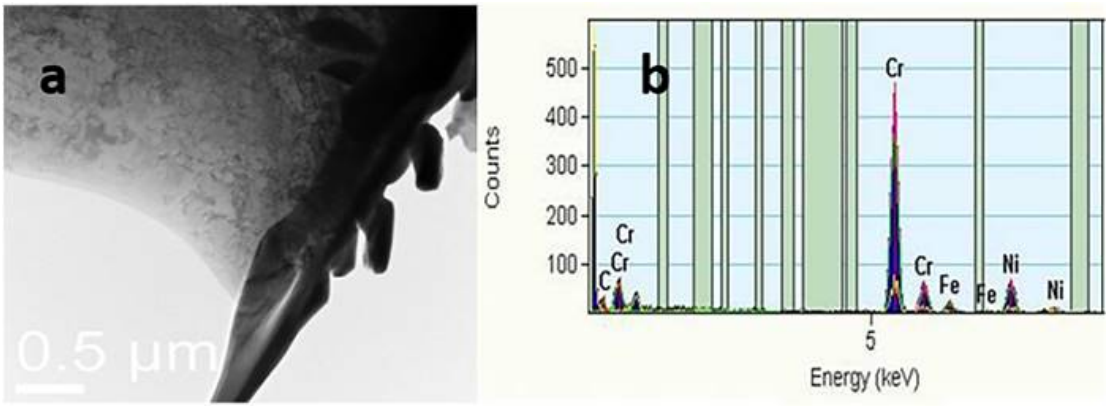


Figure 3.14 Inconel 600 rod: (a) grain boundary carbide particles
(b)EDS spectra of carbide particles.

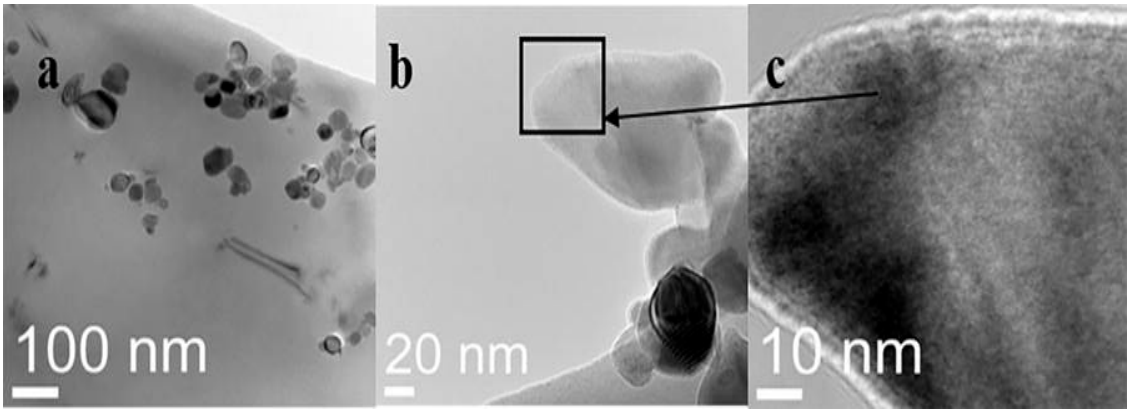


Figure 3.15 Inconel 600 coating: (a) lower magnification (b) higher magnification (c) lattice structure of the carbide particle.

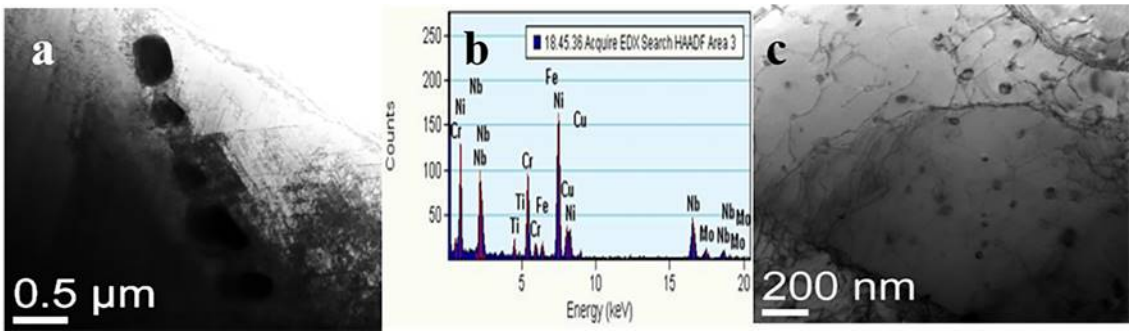


Figure 3.16 Inconel 625: (a) Carbide particles in austenite matrix of consumable rod (b) EDS of carbide particle in (a) and (c) Carbide particles in austenite matrix of coating.

These carbides are typical in the alloy and they form during the melting and solidification processes and during heat treatment [18]. Figure 3.16b shows an EDS spectrum of secondary particle rich in Cr, Ti, and Nb. Ni would have been sensed by the matrix. Cu shown in the EDS came from the background.

Inconel 625 is considered to be a solid solution alloy. Carbides that can be found in Inconel 625 are $M_{23}C_6$, a chromium-rich carbide, and MC and $M_6C$ (rich in nickel, niobium, molybdenum, and carbon). The increased hardness in Inconel 625 can be due to the sluggish precipitation of a nickel-niobium-rich phase, gamma prime, which may transform to $Ni_3Nb$ when heated for long times [19]. Even after extended periods of exposure to temperatures between 813 to 1273 K, embrittling intermetallic phases such as sigma did not precipitate out [19].

Figure.3.16c shows the Inconel 625 coating with a large number of carbide particles with a size less than 50 nm present in the austenite matrix. These fine carbides are a result of fragmentation of originally present coarser carbides due to friction surfacing. Particle morphology was more or less uniform and distributed in the austenite matrix evenly. Inconel 625 is reported to be affected by $M_{23}C_6$ carbides in the grain boundaries, gamma double prime ($\gamma''$) in the grains, and MC type carbides when exposed between 823 to 1023 K [20]. Figure 3.16c shows no gamma double prime precipitates indicating that in the as-coated sample, the strengthening precipitates dissolved into the matrix.

The standard optical metallographic methods showed the grain size of as-received Inconel 800H to be 84 ± 10 μm. Figure 3.17a shows fine carbides distributed in the matrix of austenite. Figure 3.17b shows a grain boundary carbide network of particles.

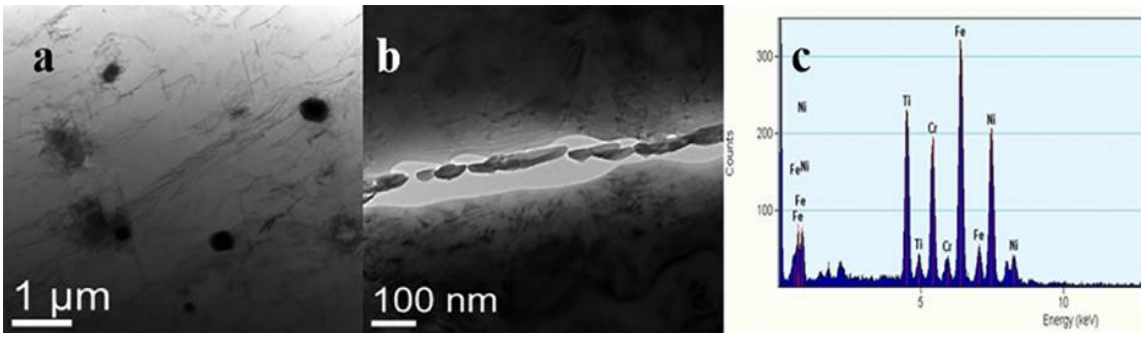


Figure 3.17 Inconel 800H rod: (a) carbide particles in the austenite matrix, (b) grain boundary carbide particles, and (c) EDS of carbide particle in (a).

Figure 3.17c shows EDS analysis of a particle in the base metal matrix. EDS analysis shows the particle could be TiC. Alloy 800H is a solid-solution-strengthened alloy with additional strengthening by precipitation of Ti(C,N) and $M_{23}C_6$ [21].

Friction surfacing of the alloy was found to cause dynamic recrystallization in Inconel 800H coating with the resulting grain size on the order of 1-3 µm (Figure 3.18a). The coatings also showed fine carbide particles uniformly distributed in the matrix (Figure 3.18b) both along the grain boundaries and within the grains. EDS analysis of the particle in the coating showed it was predominantly rich in Ti indicating it could be TiC (Figure 3.18c and Figure 3.18d). Many of the $Cr_{23}C_6$ particles coexist with Ti(C,N) precipitates in the matrix [21].

The current study showed that the carbides which play an important role in improving the creep life of these metals became finer due to the extensive plastic deformation and distributed uniformly throughout the matrix compared to their consumable rod counterparts. These finely dispersed particle may help in improving the creep life of these weld transition joints by inhibiting the movement of dislocations at the grain boundaries and matrix [3].

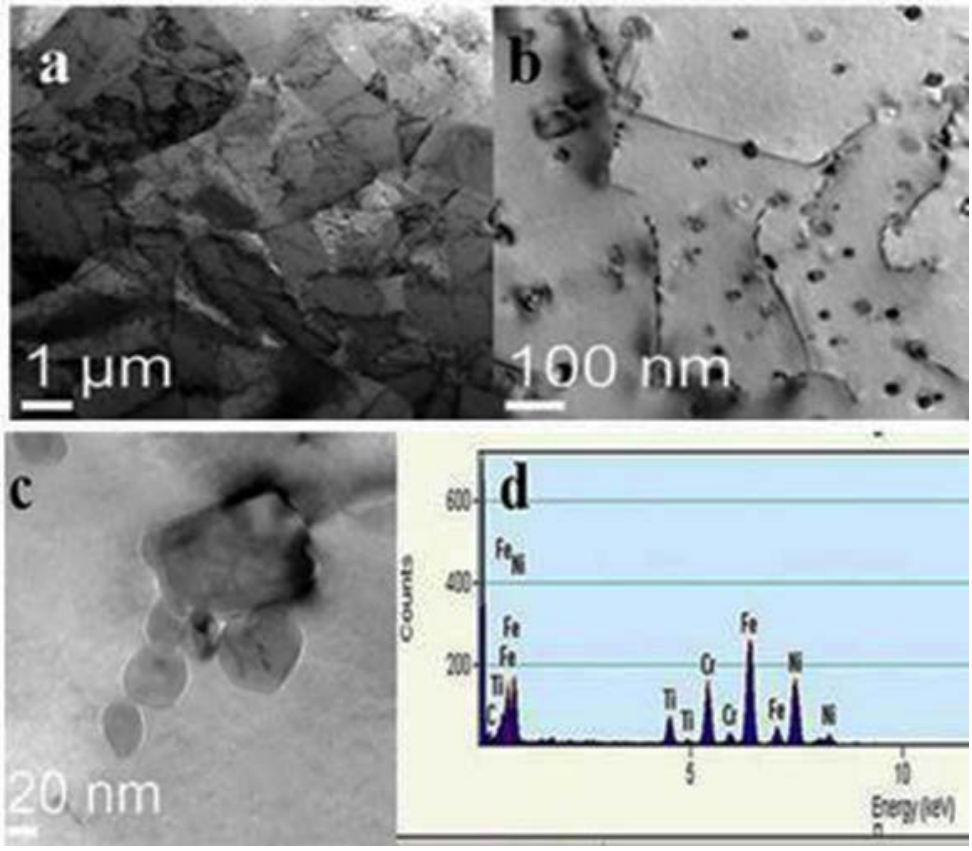


Figure 3.18 Inconel 800H coating: (a) recrystallized grains, (b) fine carbide particles in the austenite matrix. (c) high mag. of (b), and (d) EDS of carbide particle of (c).

3.1.2.3 Conclusions

1. In general, all the friction surfaced coatings studied were found to exhibit dynamic recrystallization. Grain refinement and increase in hardness were observed in all Ni-based alloy coatings due to the dynamic recrystallization. The carbide particles were found to be finer and distributed uniformly throughout the matrix, compared to their consumable rod counterparts.

2. Inconel 600 consumable rod showed chromium rich carbide particles with an average size of 275 to 300 nm. In contrast, friction surfaced coating of Inconel 600 showed fine particles with an average size of 50 nm.

3. Inconel 625 consumable rod showed carbides which were found to be rich in Nb, Ti, and Mo. Friction surfaced coating of Inconel 625 coating showed large number of carbide particles with a size less than 50 nm. No strengthening precipitates were found in the as-coated sample.

4. Inconel 800H consumable rod showed carbides distributed in the matrix as well as at the grain boundaries. Friction surfaced coating of Inconel 800H showed fine carbide particles uniformly distributed in the matrix both along the grain boundaries and within the grains.

## 3.2 Development and characterization of weld transition joints by friction welding

Friction welding is a solid state joining method which produces coalescence of material under compressive force when the workpiece rotates relative to each other, generating heat and plastically displacing the material from the faying interface resulting in metallurgical bonding. To develop transition joints between P91 steel and AISI 304 stainless steel, a continuous drive friction welding machine was used as shown in Figure 3.19. Materials to be joined were in the form of cylindrical rods and fixed in two clamps of the machine. One side of the rod is held stationary and the other rod rotates with predetermined rotational speed. The parameters which are essential to get a good bonding between two materials are friction pressure, rotational speed, burn-off-length, and upset pressure.

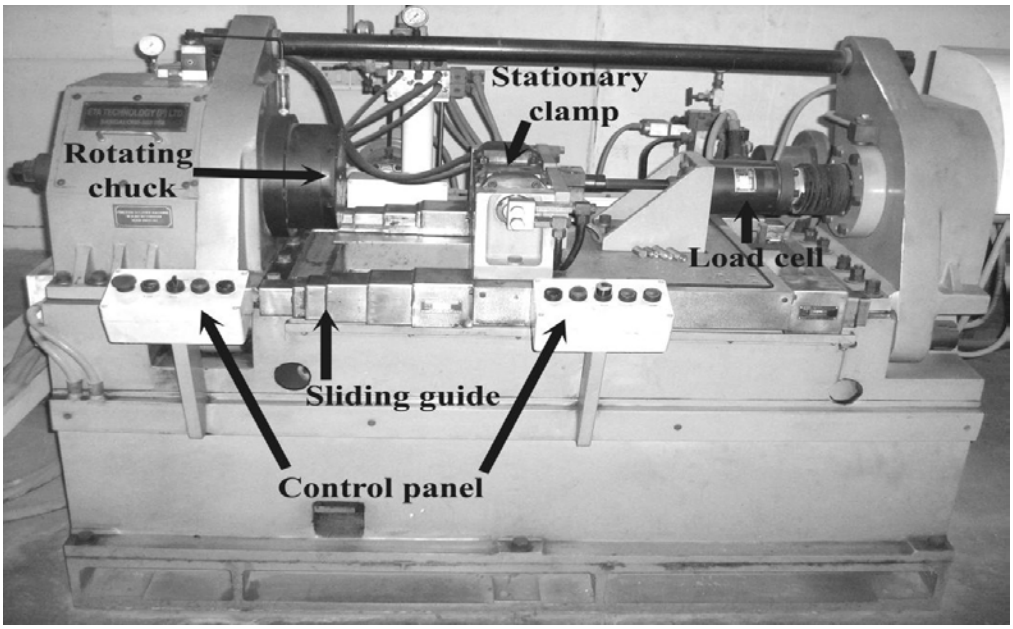


Figure 3.19 Photograph of continuous drive friction welding machine.

### 3.2.1 Process parameters used for developing friction weld transition joints

The following welding parameters were used: Friction Pressure= 160 MPa; Upset Pressure= 280 MPa; Rotational Speed= 1500 rpm; and Burn-off length= 5 mm. In the final joints, each interlayer had a thickness of ~3mm. The steps involved in making P91/AISI 304 transition joints are illustrated schematically in Figure 3.20. Initially, IN 625 rod was welded to P91 steel rod. Then IN625 rod was cut to leave an 8 mm thick layer on the P91 rod. After welding, 3 mm thick IN625 was left as an interlayer (taking in to account 5mm burn-off length). IN 600 and IN800H layers were successively deposited in the same way and finally, AISI 304 rod was friction welded to IN800H interlayer. Figure 3.21 shows a P91/AISI 304 transition joint produced using friction welding employing multiple interlayers.

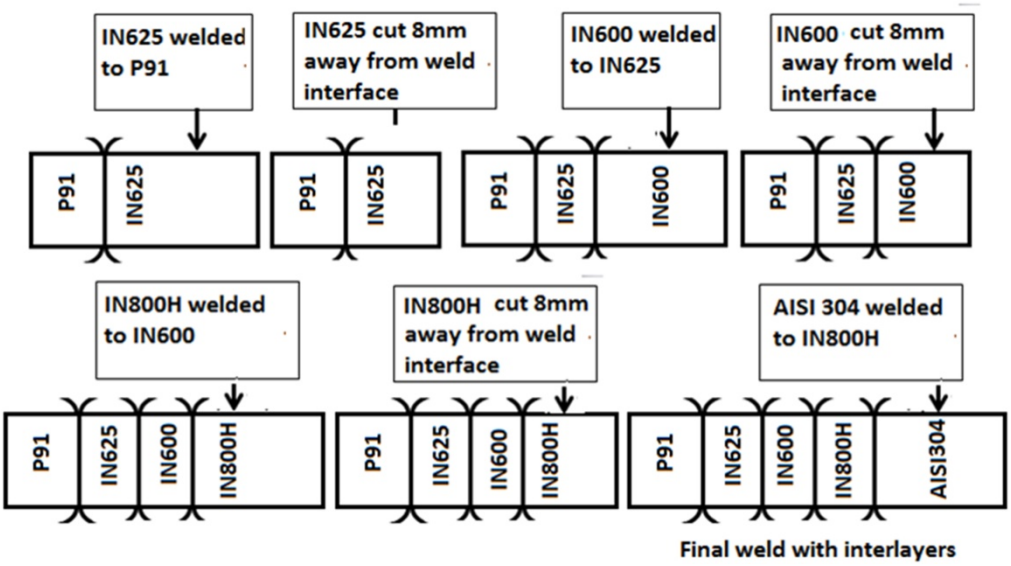


Figure 3.20 Steps involved in making P91/AISI 304 weld transition joints.

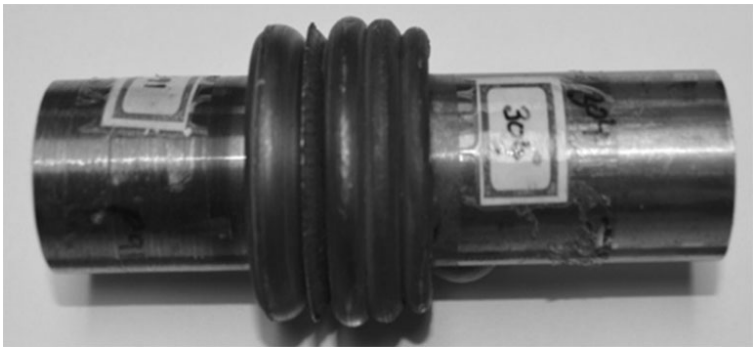

Figure 3.21 P91/AISI 304 weld transition joint produced using friction welding employing multiple interlayers.

### 3.2.2 Microstructural characterization of as-welded transition joint developed by friction welding

Figure 3.22 shows the microstructures of P91/AISI304 weld transition joint at various interfaces. All the interfaces showed good bonding without any voids and cracks. Grain size measurement and microstructural analysis were performed near the interfaces of weld interlayers in as-welded conditions. The grain size at the interfaces of the three weld interlayer materials (IN625, IN600, and IN800H) in as-weld condition are given in Table 3.7. For comparison, the grain sizes of as-received base material rods are also presented. Compared to the grain size of starting rods (12-84 µm), the weld interfaces of all Ni-based alloy interlayers were found to be relatively fine (3-10 µm). This is an indication that materials underwent dynamic recrystallization (DRX) during friction welding. This phenomenon is commonly observed in processes where high strain rates and temperatures are involved [6]. Similar phenomena (DRX) were noticed by Satyanarayana et al. and Meshram et al. near weld interface of friction welded joints [22,23].

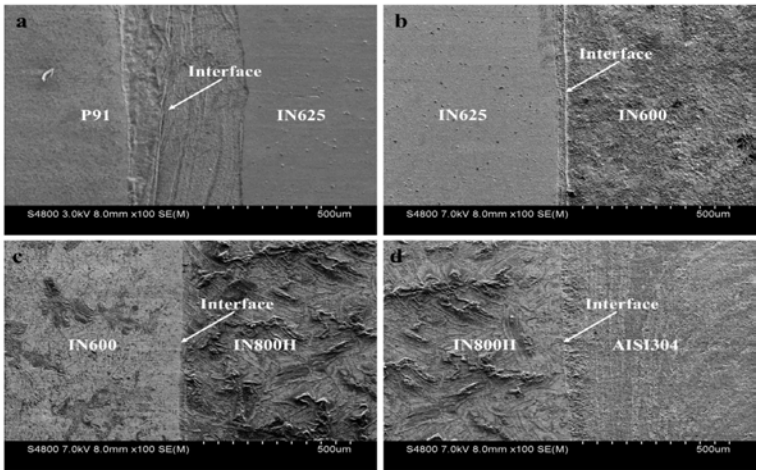


Figure 3.22 SEM micrographs at various interfaces of weld interlayers: a) P91/IN625, b) IN625/IN600, c) IN600/IN800H, and d) IN800H/AISI304.

Table 3.7 Grain size (μm) of weld interfaces in as-weld condition.

| | IN625 | | IN600 | | IN800H | |
|---|---|---|---|---|---|---|
| | Close to P91 | Close to IN600 | Close to IN625 | Close to IN800H | Close to IN600 | Close to AISI 304 |
| Rod-as-received | 12 ± 5 | 12 ± 5 | 15 ± 8 | 15 ± 8 | 84 ± 10 | 84 ± 10 |
| Interface As-weld | 3 ± 1 | 3 ± 1 | 3 ± 1 | 3 ± 1 | 10 ± 2 | 10 ± 2 |

## 3.3 Microstructure modeling of dynamic recrystallization using cellular automata

### 3.3.1 Introduction

Friction-based welding processes such as friction welding and friction stir welding are widely used for joining similar and dissimilar metals. These welds are not subjected to melting and solidification [24–27] compared to conventional fusion-based processes. Many problems such as hot cracking, porosity, inclusion, and dilution which are characteristic features of fusion welding are absent in the friction-based welding processes. In both fusion and solid state welding methods, exposure to high temperature results in different microstructural evolution across the weldment. In fusion welding, parameters influencing the microstructure are thermal related such as temperature and cooling rate. However, in solid state welds, the microstructural changes across the weldment are influenced not only by temperature but pressure too. For example, the weldment of fusion welded sample consists of solidified columnar grains followed by

coarse grain heat affected zone (CGHAZ), fine grain heat affected zone (FGHAZ), intercritical heat affected zone (ICHAZ), and unaffected zone of base metal [28]. In contrast, the friction stir and friction welded weldment consists of a weld interface of very fine grain structure followed by thermo mechanically heat affected zone (TMHAZ) [22,24–26]. The width of grain refined zone in friction stir welding is relatively larger while it is smaller in a friction weld. The formation of the grain refined structure at the weld interface or stir zone is attributed to dynamic recrystallization (DRX) phenomena due to high strain rate and temperature involvement. In these methods, friction between two metals generates heat and combination of applied pressure and rotational speed generates high strain rate in the system. Therefore, microstructural evolutions in friction-based methods are dictated by different strain rates and temperatures across weldment. However, prediction of these parameters by experimental route is very complicated, especially strain rates. For friction stir welding, various finite element modeling approaches were adopted to predict the thermal profiles, metal flow behavior, and strain rates across the weldment [29–31]. Very few works [32,33] are reported with regard to microstructural modeling of friction stir joints. As for friction welds, not much attention is paid to the microstructural modeling. In view of the limited understanding of microstructural aspects of friction-based welds through theoretical understanding, this work was taken up. It is aimed to predict the strain rates and microstructural evolution during friction welding through microstructural modeling route.

For modeling of DRX, several methods have been adopted such as Monte Carlo, phase field [34], vertex method, and cellular automata [35,36] methods. Among these, cellular automata method gained much attention for microstructural modeling of DRX

due to its discrete temporal evolution of space and time. Thus, cellular automata method is adopted in the present work. The first part of work is focused on DRX modeling and its validation with the experimental data of super alloy Inconel 718 during hot compression and the second part is focused on using the validated model to predict the strain rates and microstructural evolution during friction welding of Inconel 718 as obtained in the present case.

### 3.3.2 Background

#### 3.3.2.1 Cellular automata method

Cellular automata [15] is an algorithm-based model, where space of interest is divided into a finite number of grids called 'cells'. The state of a cell is governed by its local neighborhood and the transformation rule. There are two types of neighborhood which can be used for simulation of recrystallization, von Neumann's and Moore's neighborhood. In von Neumann's, only nearest neighbors are considered whereas Moore's consider both nearest and secondary neighbors. The state of any cell at time step ($t+\Delta t$) using von Neumann's neighboring rule can be expressed as

$$\xi_{i,j}^{t+\Delta t} = f\left(\xi_{i-1,j}^{t}, \xi_{i,j-1}^{t}, \xi_{i,j}^{t}, \xi_{i+1,j}^{t}, \xi_{i,j+1}^{t}\right)$$

where $\xi_{i,j}^{t}$ represents the value of variables $\xi$ at site ($i$,$j$) at time $t$. Function $f$ is the transformation rule which determines the evolution of the site ($i$,$j$) along with time, and it can be set according to the characteristics of the system of interest.

3.3.2.2 Theoretical model and simulation procedure for DRX

Dynamic recrystallization (DRX) is commonly observed in metals when subjected to high temperature deformation. Mostly low to medium stacking fault energy systems show this kind of behavior such as copper- and nickel-based alloys. DRX is known to occur when dislocation density of the system reaches some critical value which, in turn, depends on high temperature deformation parameters such as strain rate and temperature [37]. The final microstructure of DRX depends on two important phenomena: nucleation and growth. Both nucleation and growth are closely related to dislocation density.

For this work, 2D square lattice was employed. Four state variables were allocated to each of the cells: (i) grain number represents different grains, (ii) grain color represents orientation and boundary energy of the grain, (iii) dislocation density variable, and (iv) distance variable which controls the grain growth. Von Neumann's neighborhood was used to simulate the grain growth.

For the evolution of dislocation density, Kocks and Mecking law [11,38] was used. Based on this law, the dependence of dislocation density with strain can be expressed as

$$\frac{d\rho}{d\varepsilon} = k_1\sqrt{\rho} - k_2\rho \quad (1)$$

where $k_1$ is the constant that represents hardening and $k_2$ is the recovery parameter. The constant $k_1$ is independent of strain rate and only depends on temperature whereas recovery parameter $k_2$ is a function of both strain rate and temperature. The high temperature flow stress at the macroscopic level can be calculated using the following expression which is related to the dislocation density [11,38].

$$\sigma = \alpha G b \sqrt{\bar{\rho}} \quad (2)$$

where $\alpha$ is the dislocation interaction term (typically ranges from 0.5 to 1.0 for most of the metals), G is the shear modulus of the material, b is the burgers vector, and $\sqrt{\bar{\rho}}$ is the mean dislocation density, given by

$$\bar{\rho} = \frac{1}{n}\sum_{i=1}^{n} \rho_i \quad (3)$$

where $n$ is the total number of cells and $\rho_i$ is the dislocation density of $i^{th}$ cell. $k_1$ is related with the hardening rate [37] and expressed as

$$\theta_0 = \alpha G b k_1/2 \quad (4)$$

where $\theta_0$ is the hardening rate and can be determined from the slope of experimental flow curve at particular temperature. The recovery parameter $k_2$ and hardening constant ($k_1$) [37] are related with each other as follows

$$\sigma_s = \alpha G b k_1/k_2 \quad (5)$$

where $\sigma_s$ is the steady state stress. The recovery parameter $k_2$ can be determined after calculating the value of $k_1$ and $\sigma_s$. The steady state stress [39] is calculated according to the following equation

$$\sigma_s = \frac{1}{\alpha}\sinh^{-1}\left(\frac{Z}{A}\right)^{\frac{1}{n}} \quad (6)$$

where $A, \alpha,$ and $n$ are the material constants. Z is the Zener Holloman parameter which is a function of strain rate and temperature and given by following equation

$$Z = \dot{\varepsilon}\exp\left(\frac{Q_{act}}{RT}\right) \quad (7)$$

where $\dot{\varepsilon}$ is the strain rate, T is the temperature in Kelvin, and R is the gas constant. In the beginning of the deformation, evolution of dislocation with strain was calculated using equation (1). Once the dislocation of the deforming matrix crosses the critical value of

the dislocation, new nuclei will form at the grain boundary. The value of the critical dislocation density can be calculated using the following expression derived by Roberts and Ahlblom [40]

$$\rho_c = (\frac{20\gamma_i\dot{\varepsilon}}{3blM\tau^2})^{1/3} \quad (8)$$

where $\gamma_i$ is the grain boundary energy, $M$ is the grain boundary mobility, $l$ is the dislocation mean free path, and $\tau$ is the dislocation line energy and can be calculated from the following expression [11]

$$\tau = 0.5Gb^2 \quad (9)$$

In the present study, nucleation rate is calculated based on the following equation which is a function of both strain rate and temperature [37].

$$\dot{n}(\dot{\varepsilon}, T) = C\dot{\varepsilon}^m \exp(-\frac{Q_{act}}{RT}) \quad (10)$$

where C is the nucleation constant and m is the exponent which is set to 1 in this study. The percentage of DRX can be calculated using equation (11). For a specific hot deformation condition, if the percentage of DRX and grain size is known, nucleation rate can be calculated using equation (11) [37].

$$\eta = \dot{n}\frac{\varepsilon}{\dot{\varepsilon}}\frac{4}{3}\pi r^3 \quad (11)$$

where $\eta$ is the percentage of DRX, $\varepsilon$ is the true strain, and $r$ is the mean radius of recrystallized grain. Once the nuclei are generated at the grain boundary or any defected area, that cell is considered a recrystallized cell. The dislocation density of that cell is set to zero or annealed state dislocation density which raises the difference in dislocation densities between deformed and recrystallized cells. The difference in dislocation densities creates a force for the nuclei to grow. The velocity of the grain follows the following equation [36,37]

$$V = M\Delta f \quad (12)$$

where $\Delta f$ is the driving force per unit area and $M$ is the grain boundary mobility which can be calculated as follows

$$M = M_0 \exp(\frac{-Q_b}{RT}) \quad (13)$$

where $M_0$ is the constant and $Q_b$ is the boundary diffusion activation energy. The driving force is a function of dislocation density difference and grain boundary energy, expressed as [36,37]

$$\Delta f = \tau(\rho_m - \rho_i) - \frac{2\gamma_i}{r_i} \quad (14)$$

where $\gamma_i$ is the grain boundary energy and function of grain boundary misorientation ($\theta$). It can be calculated from Read-Shockley equation [36,37],

$$\gamma_i = \gamma_m \frac{\theta_i}{\theta_m}(1 - \ln\left(\frac{\theta_i}{\theta_m}\right)) \quad (15)$$

where $\gamma_m$ and $\theta_m$ are the grain boundary energy and misorientation when it became high angle boundary ($\theta$>15$^o$).

The initial microstructure was created using a fixed number of nuclei in a matrix and allowed them to grow until they impinges with each other. The orientation of the grains was selected randomly and ranges from 1 to 180 degree. Figure 3.23 represents the initial microstructure created as described above. The matrix consists of 250×250 cells. Each cell in real dimension is equivalent to 1 $\mu m$. Periodic boundary conditions were used for this simulation. Time step Δt is calculated as $\frac{d}{v_{max}}$, where $d$ is the diameter of critical radius and $v_{max}$ is the maximum velocity. Table 3.8 shows the constants used for this simulation. All the constant values were calculated using experimental data from the work of Chen et al. [41]. Inconel alloy 718 was used for friction welding experiments.

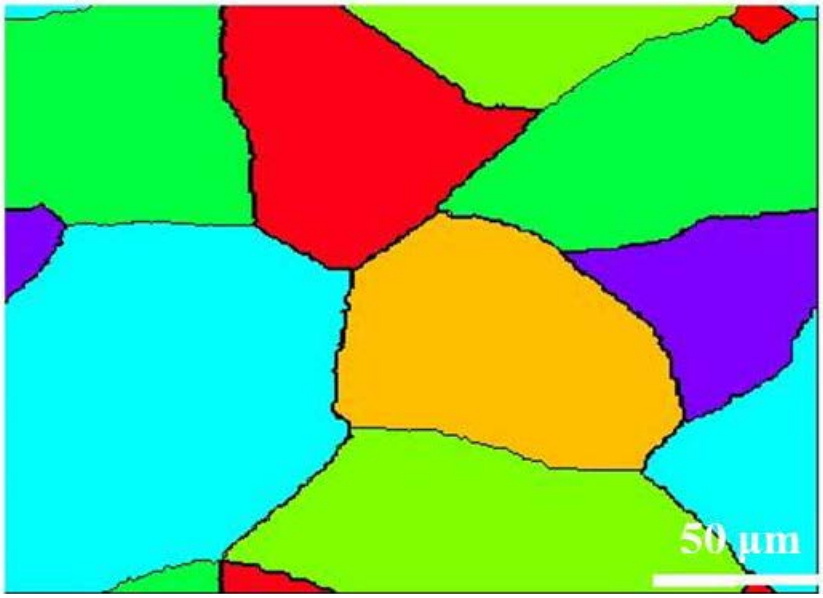


Figure 3.23 Initial microstructure generated by cellular automata.

Table 3.8 Constant values used for the simulation of Inconel 718 alloy [41].

| G<br>Pa | b<br>m | $\gamma$<br>J·m$^2$ | $Q_{act}$<br>kJ/mol | $Q_b$<br>kJ/mol | n | $\alpha$ | A<br>Pa$^{1/n}$ |
|---|---|---|---|---|---|---|---|
| $8.31\times10^{10}$ | $2.56\times10^{-10}$ | 0.625 | 474 | 474 | 4.2 | 0.00415 | $7.07\times10^{17}$ |

The chemical composition (wt%) of Inconel 718 used in is as follows: 51.6% Ni, 18.2% Cr, 5.1% Nb, 3.28% Mo, 1.06% Ti, 0.56% Al, 0.33% V, 0.09% Mn, 0.01% S, 0.004% C, 0.003% B, and 19.793% Fe. The microstructure of as-received Inconel 718 is shown in Figure 3.24. Microstructure consists of equi-axed grains and annealing twins with average grain size of 29 µm. Rotary friction welding machine was used to develop friction welds. The following welding parameters were used: Friction Pressure: 300 MPa, Upset Pressure: 600 MPa, Burn-off Length: 4 mm, and Rotational Speeds of 1200, 1500, and 1800 RPM. Microstructural analysis of as-received and welded samples was

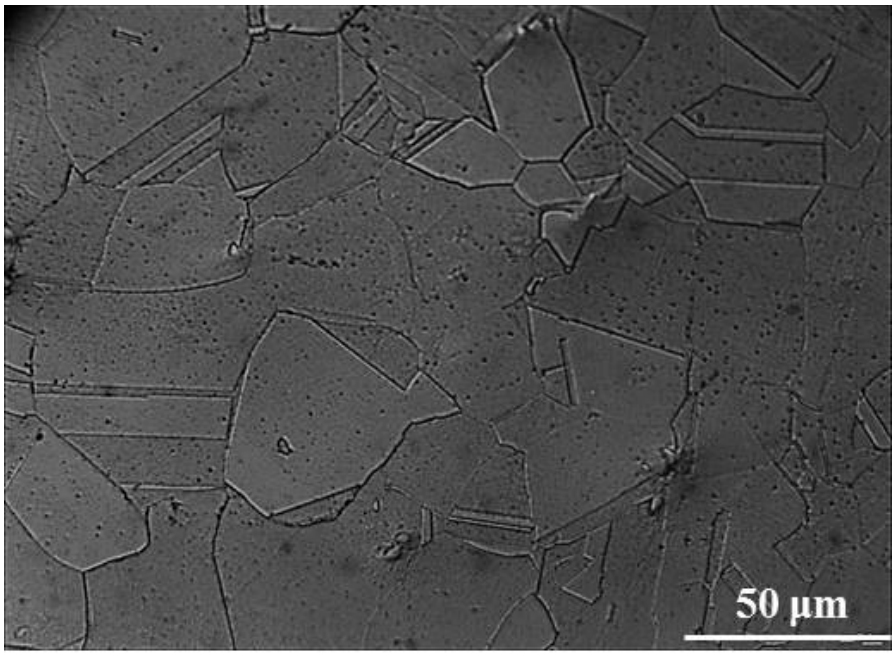


Figure 3.24 As-received base metal microstructure of Inconel 718.

perfomed with an optical and scanning electron microscope. Standard metallographic procedures of hot mounting, grinding, and polishing were performed to prepare the sample up to the surface roughness of 0.05 µm followed by etching. Samples were etched using kalling reagent (100 ml ethanol + 100 ml HCl + 5g $CuCl_2$). For electron backscattered diffraction (EBSD) studies, samples were prepared by mechanical polishing followed by final polishing with diamond and colloidal silica for 4 h. EBSD studies were conducted using an FEI Quanta-600 scanning electron microscope (SEM) equipped with TSL-OIM software with a step size of 1 µm.

### 3.3.3 Results and discussion

#### 3.3.3.1 Model validation

Typical flow curve during high temperature deformation consists of three stages: work hardening, softening, and steady state stage. In work hardening stage, the

accumulation of dislocation is very high due to weak recovery leading to accelerated increase in the flow stress. Once the dislocation reaches a critical value, dynamic recrystallization takes place resulting in dislocation annihilation which reduces the flow stress of the material (softening stage). In the steady stage region, dynamic balance is reached between dislocation accumulation (work hardening) and dislocation annihilation. Figure 3.25a represents the simulated and experimental flow curves at constant temperature (1253 K) with different strain rates (1, 0.1, 0.01, and $0.001s^{-1}$). Figure 3.25b represents the simulated and experimental flow curve at constant strain rate ($1\ s^{-1}$) with different temperatures (1193, 1223, 1253, 1283, and 1313 K).

Increasing trend in flow stress was observed with increasing strain rates and decreasing deformation temperature. The increasing trend in flow stress is possible due to two reasons: (1) increasing rate of dislocation accumulation and (2) decreasing rate of grain growth. At higher strain rate, the rate of dislocation accumulation is fast which leads to high amount of work hardening into the system. Further, the deformation time is short as compared to lower strain rates and thus reduces the growth of new recrystallized grains. However, at high temperature, the mobility of growing grain is faster which annihilates the dislocations generated by work hardening thus reducing the flow stress of the system. Simulated results are found to agree well with the experimental results as shown in Figure 3.25a and Figure 3.25b. All the simulated peak stress values are quite comparable with the experimental peak stress values. Small deviation has been observed at later stages of the deformation after 0.5% of true strain. This deviation is observed when it is deformed at high strain rates or at lower temperatures. It is found that the softening of Inconel alloys during hot deformation is due to dynamic recrystallization.

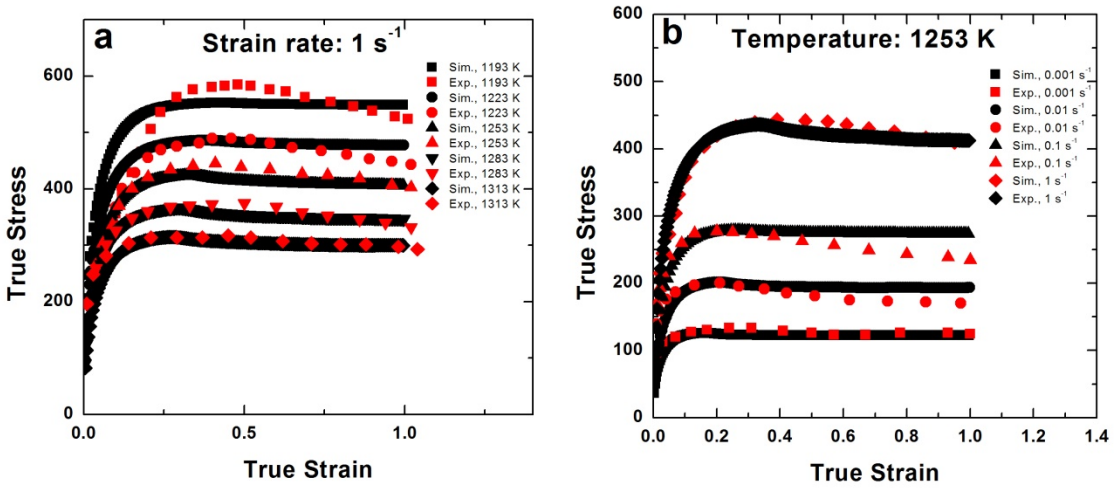


Figure 3.25 Comparison of experimental and simulated flow curve (a) for different temperatures 1193, 1223, 1253, 1283, and 1313 K) at constant rate of $1s^{-1}$ (b) for different strain rates (0.001, 0.01, 0.1, and $1s^{-1}$) at constant temperature of 1253 K.

However, adiabatic heating also plays a role in softening of material when deformed under high strain rates and lower temperatures as reported by Weis et al. [42]. It has been reported that adiabatic heating increased the temperature of the system by 333 K when deformed at 1223 K and a strain rate of 1 $s^{-1}$. Therefore, it can be concluded that deviation in flow stress between experimental and simulated curve in later stages of deformation is due to increased temperature ($\Delta T$) in the system due to adiabatic heating. Figure 3.26 shows the simulated microstructures at different temperatures (a) 1223 K, (b) 1253 K, and (c) 1283 K while keeping the strain rate constant ($0.001s^{-1}$). Figure 3.27 shows the simulated microstructures at different strain rates (a) $0.1s^{-1}$, (b) $0.01s^{-1}$, and (c) $0.001s^{-1}$ keeping the deformation temperature (1313 K) constant. The simulated microstructure agreed well with the experimental results. Here, each color represents the orientation of a particular grain. The measured grain size [41] of samples deformed with a rate of $0.001s^{-1}$ at 1223, 1253, and 1283 K are 11.3, 14.1, and 17.6 $\mu m$, respectively.

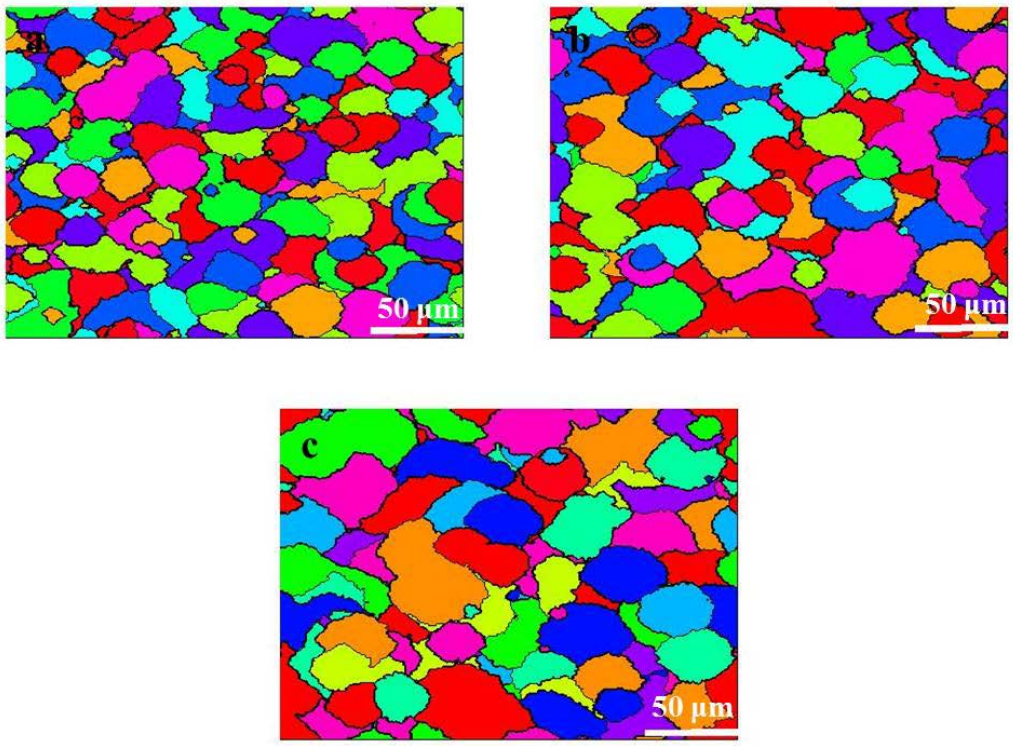


Figure 3.26 Simulated microstructures at different temperatures (a) 1223 K, (b) 1253 K, and (c) 1283 K with constant strain rate of $0.001s^{-1}$.

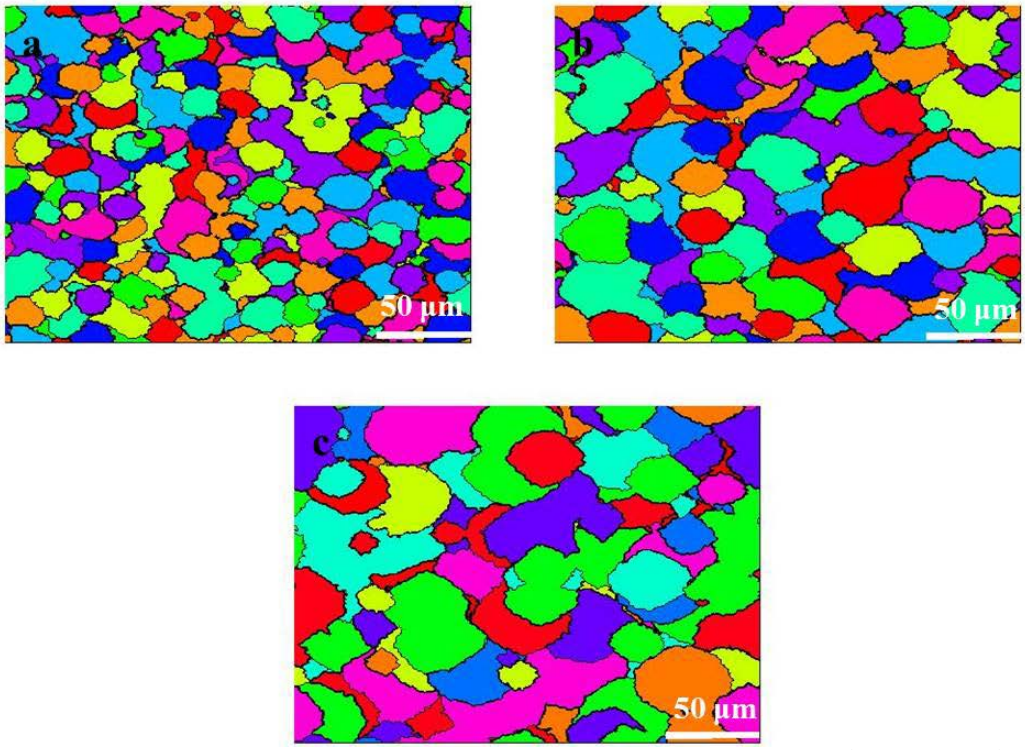


Figure 3.27 Simulated microstructures at different strain rates (a) 0.1 $s^{-1}$, (b) 0.01$s^{-1}$, and (c) 0.001$s^{-1}$ with constant temperature of 1313 K.

The simulated grain sizes deformed at 1223, 1253, and 1283 K keeping the strain rate ($0.001s^{-1}$) constant are 11.6, 14.3, and 16.75 $\mu m$, respectively. Similarly, the measured grain size deformed at 1313 K with strain rates of 0.1, 0.01, and 0.001 are 10.2, 14.2, and 18.8 $\mu m$, respectively. On the other hand, simulated grain sizes deformed at 1313 K with strain rates of 0.1, 0.01, and 0.001 are 9.8, 14.1, and 19.1 $\mu m$, respectively. The results indicate the closeness of experimental and simulated results.

3.3.3.2 Prediction of strain rate and temperature in friction welds using grain size

Cross section view of friction welded sample of Inconel 718 developed with 1500 RPM is shown in Figure 3.28. The welded region has a typical lens shape which is mostly composed of very fine equiaxed grains and can be differentiated in the picture by the white region. The formation of refined grains in the welded region is due to involvement of very high strain rates and temperature. Grain refinement phenomena due to involvement of high strain rates and temperatures are commonly known as dynamic recrystallization. Figure 3.29 illustrates the EBSD pattern of friction weld sample welded at 1500 RPM. Figure 3.29a and Figure 3.29b are the EBSD pattern at center and edge of the welded sample, respectively. It can be seen that grain size at weld zone went through significant size reduction. The average grain size at the center and edge of a welded sample was found to be 1.4 and 3.1 $\mu m$, respectively. The differences in grain sizes at these two regions could be possibly due to different strain rate and temperature exposure. Figure 3.30 shows the temperature profile captured by IR camera welded at 1500 RPM. The maximum temperature recorded by IR camera from the outer surface of the rod

Figure 3.28 Cross section view of friction weld of Inconel 718 generated with 1500 RPM.

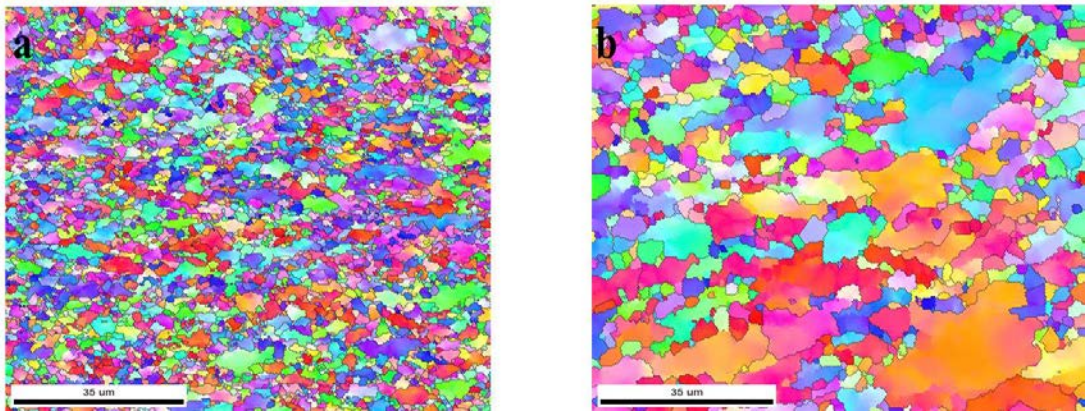


Figure 3.29 EBSD pattern of Inconel 718 friction weld developed with 1500 RPM (a) at weld center (b) at weld edge.

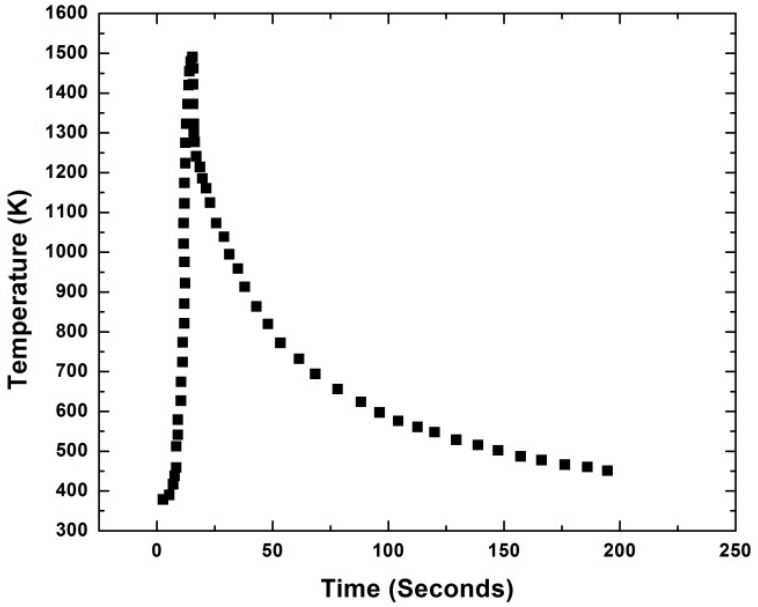


Figure 3.30 Temperature profile recorded by IR camera during friction welding performed at 1500 RPM.

during welding was 1473 K. By assuming a similar temperature at both of these locations (center and edge) for a particular rotation speed, the only parameter which creates difference in grain size is strain rate. Afterward, the validated model is used to predict the strain rate experienced during welding. For that, the temperature was kept constant equal to the recorded one (1473 K) and strain rates were varied until the grain size was matched with the experimental values. Figure 3.31a is the simulated microstructure obtained at 1473 K and 1850 $s^{-1}$ strain rate. Figure 3.31b is the simulated microstructure obtained at 1473 K and 290 $s^{-1}$ strain rate. The average grain size obtained from simulated microstructure at strain rate of 1850 $s^{-1}$ and 290 $s^{-1}$ are 1.42 and 3.13 $\mu m$, respectively. The grain size obtained from simulation is quite close to the values obtained from experimental results. Therefore, predicted values of the strain rates during friction welding at 1500 RPM from simulation at center and edge locations are 1850 and 290 $s^{-1}$,

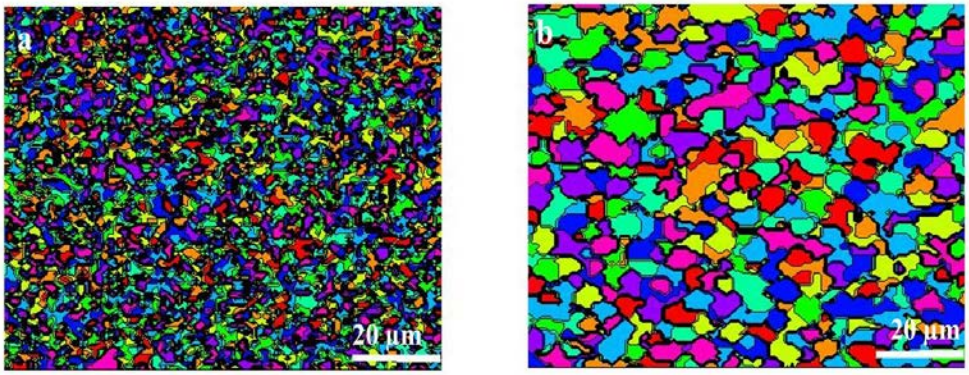


Figure 3.31 Simulated microstructure at (a) 1850 $s^{-1}$ and (b) 290 $s^{-1}$ at 1473 K temperature.

respectively. To confirm the obtained strain rate, an analytical approach is also taken to predict the strain rate during welding as adopted by Chang et al. [43,44] for friction stir welding. The material flow strain rate ($\dot{\varepsilon}$) during friction welding can be derived by the torsion type deformation as

$$\dot{\varepsilon} = \frac{R_m 2\pi r_e}{L_e} \quad (16)$$

where $R_m$ is the average material flow rate which is about half of the rotational speed, $r_e$ and $L_e$ are the radius and depth of recrystallized zone. The recrystallized zone is observed across the whole cross section of the weld interface; therefore, $r_e$ is taken as half of the rod diameter which is 8.25mm. The depth of recrystallized zone is taken as thickness of material which went through dynamic recrystallization. By taking the value of $R_m$, $r_e$, and $L_e$ as 12.5 rps (revolution per second), 8.25 mm, and 350 $\mu m$, respectively, the strain rate of 1850 $s^{-1}$ is obtained at weld center. It is also observed that the depth of recrystallization ($L_e$) at the weld center and edge is different. For example at the center, the depth of recrystallized zone is 350 $\mu m$ whereas at the edge it is 2200 $\mu m$. Similarly by taking the value of $L_e$ as 2200 $\mu m$ at the edge of the weld, the strain rate of 1850 $s^{-1}$ is

obtained. The simulated strain rate of 1850 $s^{-1}$(center) and 290 $s^{-1}$(edge) agreed well with the calculated strain rate of 1850 $s^{-1}$(center) and 294 $s^{-1}$(edge) based on equation (16) which indicates that the model can predict the actual strain rate material experienced during welding. To confirm the feasibility of this model, simulation was also carried out to predict the strain rates for friction welds generated at different rotational speeds. Rotational speeds such as 1200 and 1800 RPM were used to generate the friction welds. Figure 3.32 represents the EBSD pattern of friction welds generated at 1200 and 1800 RPM. Similar trends in grain size were observed for samples with 1200 and 1800 RPM as was observed for 1500 RPM weld sample at center and edge locations.

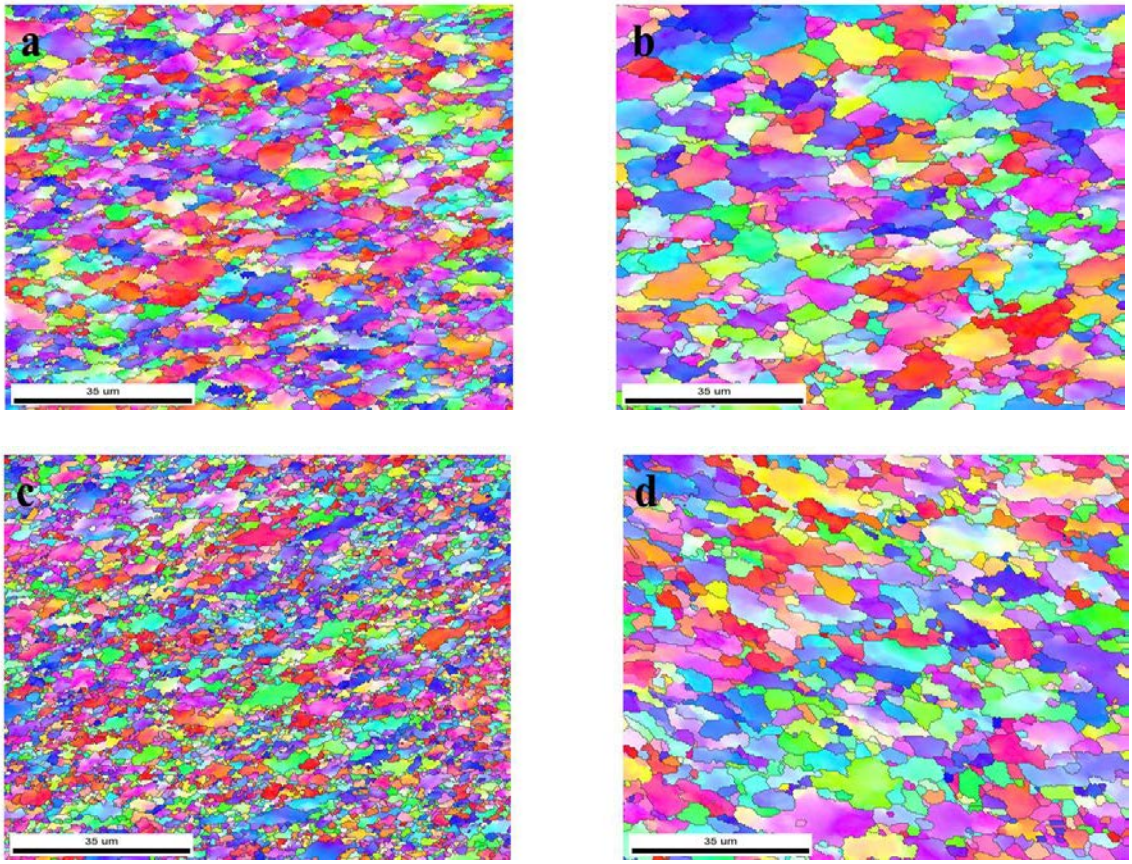


Figure 3.32 EBSD pattern of friction welds (a) at center and (b) at edge generated with 1200 RPM and (c) at center and (d) at edge generated with 1800 RPM.

The average value of grain size at different locations is listed in Table.3.9. Depth of recrystallization and hardness value corresponding to that location is also listed in Table 3.9. It can be seen from Table 3.9 that the central portion of friction welds went through higher amount of grain refinement as compared to edge in all cases and validated by their corresponding hardness values. Quite similar grain size is observed in the center and edge of friction welds generated at all rotational speeds. For example, at central position, the average grain size for 1200 RPM sample is 3.2 μm whereas for 1800 RPM sample, it is 2.9 μm. The difference in grain size is very small but it affects to a larger extent the strain rates as listed in Table 3.9. However, the calculated strain rate, based on equation (16), does not incorporate the size of grain; therefore, simulations were also run to predict the strain rates involved for samples with 1200 and 1800 RPM.

Table 3.9 List of depth of recrystallization, hardness values, grain size, and calculated strain rate at center and edge of weld with different rotational speed.

| RPM | $R_m/2$ | $r_e$, mm | $L_e$, μm | Hardness | Grain size, μm | Strain rate, $s^{-1}$ |
|---|---|---|---|---|---|---|
| 1200 | 10 | 8.25 (Edge) | ~2150 | 313.356 | 3.2 | 240.97 |
| 1500 | 12.5 | 8.25 (Edge) | ~2200 | 302.1396 | 3.1 | 294.37 |
| 1800 | 15 | 8.25 (Edge) | ~ 2000 | 302.0692 | 2.9 | 388.57 |
| 1200 | 10 | 8.25 (Center) | ~423 | 381.6391 | 1.7 | 1224.82 |
| 1500 | 12.5 | 8.25 Center) | ~350 | 421.8447 | 1.4 | 1850.35 |
| 1800 | 15 | 8.25 Center) | ~300 | 422.8921 | 1.3 | 2590.5 |

Simulations were run for 240 $s^{-1}$and 389 $s^{-1}$ strain rates at 1473 K for 1200 and 1800 RPM values, respectively. The simulated grain sizes for 1473 K at 1200 and 1800 RPM were 3.53 and 2.64 $\mu m$, respectively. The grain sizes were close to the experimental values but over predicted for 1200 RPM and under predicted for 1800 RPM within a range of ±0.2 $\mu m$. Therefore, simulations were run again with adjusted temperatures for both the rotational speeds while keeping the strain rates constant calculated by equation (16). By adjusting the temperature as 1469 K instead of 1473 K for 1200 RPM sample and, 1483 K instead of 1473 K for 1800 RPM sample, almost similar grain sizes were achieved. The simulated grain size for 1200 rpm at the center and edge of the weld were found to be 1.62 and 3.13 $\mu m$, respectively. The simulated grain sizes for 1800 RPM at the center and edge of the weld were found to be 1.38 and 3.03 $\mu m$, respectively. Figure 3.33 shows the simulated microstructures of friction welds for samples with 1200 and 1800 RPM values. Figure 3.33a and Figure 3.33b are the simulated microstructures generated at 1469K/1225$s^{-1}$ and 1469K/240$s^{-1}$, respectively. Figure 3.33c and Figure 3.33d are the simulated microstructures generated at 1483K/2590$s^{-1}$ and 1483K/389$s^{-1}$, respectively. The simulated grain size values were comparable to the experimental grain size. This suggests that not only different strain rates are responsible for the formation of different grain sizes, but temperature also plays a vital role in deciding the final grain size. It can be concluded that using this model, localized strain rates and temperature distributions can be calculated if one parameter such as temperature and strain rate is known.

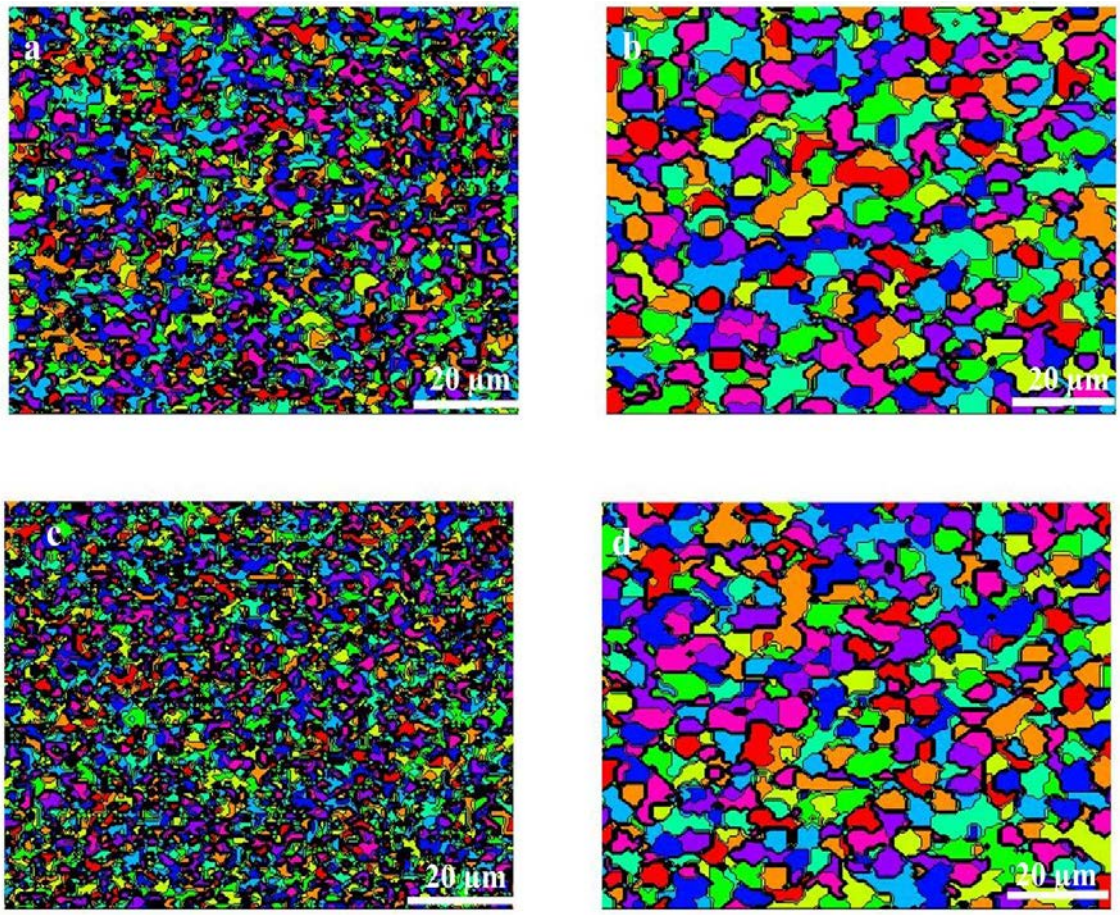


Figure 3.33 Simulated microstructure at (a) 1469K/1225$s^{-1}$, (b) 1469K/240$s^{-1}$, (c) 1483K/2590$s^{-1}$, and (d) 1483K/389$s^{-1}$.

### 3.3.4 Conclusions

Cellular automata method was employed to model microstructural evolution of Inconel 718 during hot deformation. Experimental and simulated flow curves were found to be quite comparable. However, little deviation in later stages of deformation was observed which was attributed to adiabatic heating of material due to plastic deformation. All the simulated grain sizes were found to be comparable with the experimental results. Larger grain size was observed at low strain rates and high temperature attributed to more deformation time and higher mobility. The strain rates predicted from the model at the center and edge of the weld for 1500 RPM weld were found to be 1850 $s^{-1}$ and 290 $s^{-1}$, respectively. The predicted strain rates were compared with the torsion type deformation model. In all the cases, finer grain size was observed at the weld center as compared to the edge of the weld. Temperature difference of smaller value showed significant effect on resulted grain size.

## 3.4 Selection of welding method for developing the weld transition joint for creep test

After these initial studies of optimizing the weld parameters and characterizing their microstructures, a decision had to be taken to choose one process between the friction surfacing and friction welding method to develop the weld transition joints. Considering the following factors, friction welding method was selected to develop the transition joints for further high temperature mechanical testing.

1) Easy to fabricate: Friction welding technique was found to be a time saving and easier method to fabricate transition joints compared to friction surfacing. As discussed

earlier in friction surfacing, coating thickness varied from material to material. To realize the required thickness of an interlayer with one composition, one had to deposit multiple numbers of coatings one over the other. It was found to be highly time consuming. In contrast, required interlayer thickness was found to be realized in one go using friction welding method. Keeping in view the practical advantages of simplicity, time saving, and material saving, friction welding method was selected for developing the weld transition joints for further studies.

2) Better microstructure for creep: Creep deformation and creep strength are a grain size sensitive property. During creep, first microstructural degradation happens through formation of individual voids and pores. Voids and pores are often found at the triple junction of grains. These voids eventually link together and propagate along the grain boundary leading to final failure. Therefore, smaller grain size (larger grain boundary area) reduces the creep strength of a material. On the contrary, larger grain size (smaller grain boundary area) helps improve the creep strength of a material. Both the techniques (friction welding and friction surfacing) resulted in DRX (finer) grains due to high strain rate and temperature. However, the structure after heat treatment was found to be different in both the cases as shown in Figure 3.34 and Figure 3.35. Figure 3.34a and Figure 3.34b are the microstructures of Inconel 600 alloy as coated and heat treated at 1023K/1 hour, respectively.

Figure 3.35a and Figure 3.35b show the microstructures of Inconel 625 alloy in as-welded and post welded heat treated condition (1023K/1 hour), respectively. It can be seen clearly that coated material (by friction surfacing) did not respond to heat treatment effectively with the result that the grain size was almost similar in both the cases.

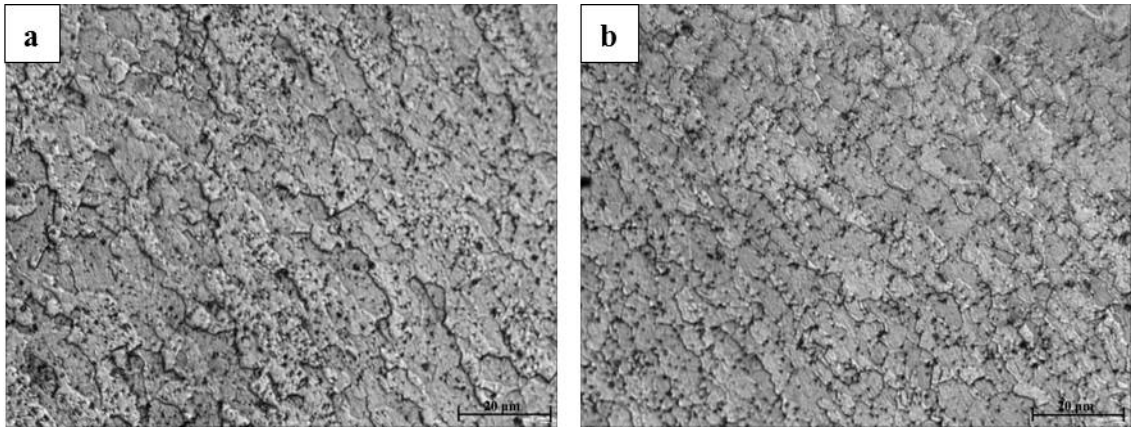


Figure 3.34 Inconel 600 alloy friction surfaced (a) as coated and (b) heat treated.

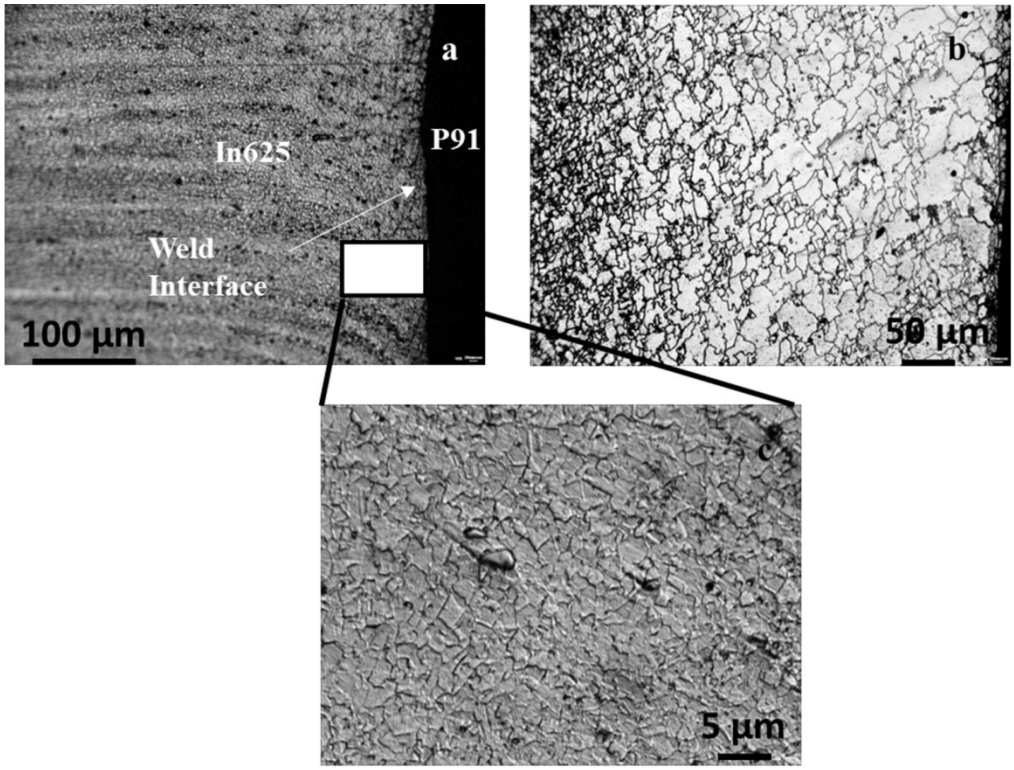


Figure 3.35 Microstructure of IN 625 near P91 interface (a) as welded (b) post heat treated (c) higher magnification picture at a region shown in a).

However, friction welded samples responded very well to the post weld heat treatment. Significant amount of grain growth was observed near the weld interface after heat treatment as can be seen from Table 3.10 which shows grain size near the interface of all three interlayer (IN625, IN600, and IN800H) in as-welded and PWHT conditions. Considering both these factors, viz., (a) ease of fabrication and (b) larger grain size after PWHT, friction welding method was adopted for developing the weld transition joints for further creep studies.

Table 3.10 Grain size (μm) of weld interfaces in as-weld and PWHT conditions.

| | IN625 | | IN600 | | IN800H | |
|---|---|---|---|---|---|---|
| | Close to P91 | Close to IN600 | Close to IN625 | Close to IN800H | Close to IN600 | Close to AISI 304 |
| Rod-as-received | 12 ± 5 | 12 ± 5 | 15 ± 8 | 15 ± 8 | 84 ± 10 | 84 ± 10 |
| Interface, As-weld | 3 ± 1 | 3 ±1 | 3 ±1 | 3 ±1 | 10 ±2 | 10 ± 2 |
| Interface, PWHT | 56 ± 5 | 20.± 4 | 37 ± 5 | 100 ± 2 | 70 ± 5 | 15 ± 8 |

## 3.5 References


[1] J. Akram, P.R. Kalvala, M. Misra, Effect of process parameters on friction surfaced coating dimensions, Adv. Mater. Res. 922 (2014) 280–285.

[2] J. Akram, R. Puli, P.R. Kalvala, M. Misra, A novel weld transition joint by friction surfacing, Manuf. Lett. 2 (2014) 104–107.

[3] J. Akram, J.. J.S. Dilip, D. Pal, B. Stucker, P.R. Kalvala, M. Misra, Microstructures of friction surfaced coatings – a TEM study, Pract. Metallogr. 53 (2016) 261–272.

[4] J. Akram, R. Puli, P.R. Kalvala, M. Misra, Microstructural studies on friction surfaced coatings of Ni-based alloys, Pract. Metallogr. 52 (2015) 590–606.

[5] H.K. Rafi, G.D. Janaki Ram, G. Phanikumar, K. Prasad Rao, Microstructural evolution during friction surfacing of tool steel H13, Mater. Des. 32 (2011) 82–87.

[6] R. Puli, G.D. Janaki Ram, Dynamic recrystallization in friction surfaced austenitic stainless steel coatings, Mater. Charact. 74 (2012) 49–54. doi:10.1016/j.matchar.2012.09.001.

[7] Y.S. Sato, P. Arkom, H. Kokawa, T.W. Nelson, R.J. Steel, Effect of microstructure on properties of friction stir welded inconel alloy 600, Mater. Sci. Eng. A. 477 (2008) 250–258. doi:10.1016/j.msea.2007.07.002.

[8] K.H. Song, K. Nakata, Microstructural and mechanical properties of friction-stir-welded and post-heat-treated inconel 718 alloy, J. Alloys Compd. 505 (2010) 144–150. doi:10.1016/j.jallcom.2010.06.016.

[9] R. Damodaram, S. Ganesh Sundara Raman, K. Prasad Rao, Microstructure and mechanical properties of friction welded alloy 718, Mater. Sci. Eng. A. 560 (2013) 781–786.

[10] K. Prasad Rao, A. Veera Sreenu, H.K. Rafi, M.N. Libin, K. Balasubramaniam, Tool steel and copper coatings by friction surfacing- a thermography study, J. Mater. Process. Technol. 212 (2012) 402–407.

[11] F.J. Humphreys, M. Hatherly, Recrystallization and related annealing phenomena, Elsevier Ltd, 2004.

[12] B.B. Rath, M.A. Imam, C.S. Pande, Nucleation and growth of twin interfaces in fcc metals and alloys, Mater. Phys. Mech. 1 (2000) 61–66..

[13] H.K. Rafi, N. Kishore Babu, G. Phanikumar, K. Prasad Rao, Microstructural evolution during friction surfacing of austenitic stainless steel AISI 304 on low carbon steel, Metall. Mater. Trans. A. 44A (2013) 345–350.

[14] M.E. Abd El-Azim, O.H. Ibrahim, O.E. El-Desoky, Long term creep behaviour of welded joints of P91 steel at 650℃, Mater. Sci. Eng. A. 560 (2013) 678–684. doi:10.1016/j.msea.2012.10.013.

[15] A. Orlova, J. Bursik, K. Kucharova, V. Sklenicka, Microstructural development during high temperature creep of 9% Cr steel, Mater. Sci. Eng. A. 245 (1998) 39–48.

[16] http://www.specialmetals.com/assets/documents/alloys/inconel/inconel-alloy-600.pdf.

[17] H.Y. Zhang, Y.H. Lu, M. Ma, J. Li, Effect of precipitated carbides on the fretting wear behavior of inconel 600 alloy, Wear. 315 (2014) 58–67.

[18] D. Li, Q. Guo, G. Shengli, H. Peng, Z. Wu, The microstructure evolution and nucleation mechanisms of dynamic recrystallization in hot-deformed inconel 625 superalloy, Mater. Des. 32 (2011) 696–705.

[19] http://www.specialmetals.com/assets/documents/alloys/inconel/inconel-alloy-625.pdf.

[20] J.F. Radavich, A. Fort, Effects of long time exposure in alloy 625 at 1200°F, 1400°F and 1600°F, in: TMS, (1994) 635–47.

[21] L. Tan, L. Rakotojaona, T.R. Allen, R.K. Nanstad, J.T. Busby, Microstructure optimization of austenitic alloy 800H (Fe–21Cr–32Ni), Mater. Sci. Eng. A. 528 (2011) 2755–2761.

[22] V. V. Satyanarayana, G.M. Reddy, T. Mohandas, Dissimilar metal friction welding of austenitic-ferritic stainless steels, J. Mater. Process. Technol. 160 (2005) 128–137. doi:10.1016/j.jmatprotec.2004.05.017.

[23] S.D. Meshram, T. Mohandas, G.M. Reddy, Friction welding of dissimilar pure metals, J. Mater. Process. Technol. 184 (2007) 330–337.

[24] M.B. Uday, M.N. Ahmad Fauzi, H. Zuhailawati, A.B. Ismail, Advances in friction welding process: a review, Sci. Technol. Weld. Join. 15 (2010) 534–558. doi:doi:10.1179/136217110X12785889550064.

[25] R. Nandan, T. DebRoy, H.K.D.H. Bhadeshia, Recent advances in friction-stir welding - Process, weldment structure and properties, Prog. Mater. Sci. 53 (2008) 980–1023. doi:10.1016/j.pmatsci.2008.05.001.

[26] R.S. Mishra, Z.Y. Ma, Friction stir welding and processing, Mater. Sci. Eng. R Reports. 50 (2005) 1–78. doi:10.1016/j.mser.2005.07.001.

[27] M. Maalekian, Friction welding – critical assessment of literature, Sci. Technol. Weld. Join. 12 (2007) 738–759. doi:10.1179/174329307X249333.

[28] S.. Mannan, K. Laha, Creep behaviour of Cr–Mo steel weldments, Trans. Indian Inst. Met. 49 (1996) 303–320.

[29] D.M. Neto, P. Neto, Numerical modeling of friction stir welding process: a literature review, Int. J. Adv. Manuf. Technol. 65 (2013) 115–126.

[30] C.C. Tutum, J.H. Hattel, Numerical optimisation of friction stir welding: review of future challenges, Sci. Technol. Weld. Join. 16 (2011) 318–324.

[31] X. He, F. Gu, A. Ball, A review of numerical analysis of friction stir welding, Prog. Mater. Sci. 65 (2014) 1–66. doi:10.1016/j.pmatsci.2014.03.003.

[32] K.K. Song, Z.B. Dong, K. Fang, X.H. Zhan, Y.H. Wei, Cellular automata modelling of dynamic recrystallization microstructure evolution during friction stir welding of titanium alloy, Mater. Sci. Technol. 30 (2014) 700–711.

[33] P. Asadi, M. Kazem, B. Givi, M. Akbari, Microstructural simulation of friction stir welding using a cellular automaton method : a microstructure prediction of AZ91 magnesium alloy, Int. J. Mech. Mater. Eng. (2015). doi:10.1186/s40712-015-0048-5.

[34] T. Takaki, T. Hirouchi, Y. Hisakuni, A. Yamanaka, Y. Tomita, Multi-phase-field model to simulate microstructure evolutions during dynamic recrystallization, Mater. Trans. 49 (2008) 2559–2565. doi:10.2320/matertrans.MB200805.

[35] R. Ding, Z.X. Guo, Coupled quantitative simulation of microstructural evolution and plastic flow during dynamic recrystallization, Acta Mater. 49 (2001) 3163–3175. doi:10.1016/S1359-6454(01)00233-6.

[36] G. Kugler, R. Turk, Modeling the dynamic recrystallization under multi-stage hot deformation, Acta Mater. 52 (2004) 4659–4668.

[37] R. Ding, Z.X. Guo, Microstructural modelling of dynamic recrystallisation using an extended cellular automaton approach, Comput. Mater. Sci. 23 (2002) 209–218. doi:10.1016/S0927-0256(01)00211-7.

[38] H. Mecking, U.F. Kocks, KInetics of flow and strain-hardening, Acta Metall. 29 (1981) 1865–1875.

[39] C. Zener, J.H. Hollomon, Effect of strain rate upon plastic flow of steel, J. Appl. Phys. 15 (1944) 22–32. doi:10.1063/1.1707363.

[40] W. Roberts, B. Ahlblom, A nucleation criterion for dynamic recrystallization during hot working, Acta Metall. 26 (1978) 801–813.

[41] X.M. Chen, Y.C. Lin, D.X. Wen, J.L. Zhang, M. He, Dynamic recrystallization behavior of a typical nickel-based superalloy during hot deformation, Mater. Des. 57 (2014) 568–577. doi:10.1016/j.matdes.2013.12.072.

[42] M. Weis, M. Mataya, S.. Thompson, D. Matlock, The hot deformation behavior of an as-cast alloy 718 ingot, in: Miner. Met. Mater. Soc. (1989) 135–154. doi:10.7449/1989/Superalloys_1989_135_154.

[43] C.I. Chang, C.J. Lee, J.C. Huang, Relationship between grain size and zener–holloman parameter during friction stir processing in AZ31 Mg alloys, Scr. Mater. 51 (2004) 509–514. doi:10.1016/j.scriptamat.2004.05.043.

[44] C.I. Chang, X.H. Du, J.C. Huang, Achieving ultrafine grain size in Mg-Al-Zn alloy by friction stir processing, Scr. Mater. 57 (2007) 209–212. doi:10.1016/j.scriptamat.2007.04.007.

# CHAPTER 4

# CREEP PROPERTIES OF WELD TRANSITION JOINT

In this chapter, results are shown in two parts. The first part of the work deals with studying the effects of heat treament on microstructure across the heat affected zone of welds and how it is responsible for the creep performance of these joints. The second part deals with the comparison of creep behavior between a single layer weld developed with Inconel 600 (P91/IN600/AISI304) and three layer welds developed with Inconel 625, Inconel 600, and Inconel 800H (P91/IN625/IN600/IN800H/AISI304). It primarly deals with characterizing the creep behavior and associated mechanisms in weld joints using threshold stress concept and analysis of creep rupture life based on the Monkman-Grant approach.

## 4.1 Carbon diffusion across weld transition joint

### 4.1.1 Microstructure of welded specimen

In friction welds, microstructural evolution at the heat affected zone (HAZ) is governed by different levels of frictional heat, strain, and strain rates [1] experienced by the welds. The different zones in the HAZ are classified as follows: (a) contact zone (b) fully plasticised zone (c) partly deformed zone and (d) undeformed zone [1]. The microstructures in these zones are different from each other. For example, (a) in the

contact zone, the grains are very refined due to the exposure to a high degree of plastic deformation and temperature; (b) in the fully plasticized zone, material undergoes dynamic recrystallization; (c) in the partly deformed zone, grains undergo grain growth; and (d) in the undeformed zone, grain size is similar to base metal. Figure 4.1 shows the hardness profile in the HAZ and base metal side of P91 (up to a length of 5 mm) at the weld interface of a three layer weld after PWHT. The interlayer facing P91 at the interface is IN 625. It can be seen that the hardness in the HAZ of P91, very close to the interface, was relatively high compared to the base metal hardness value.

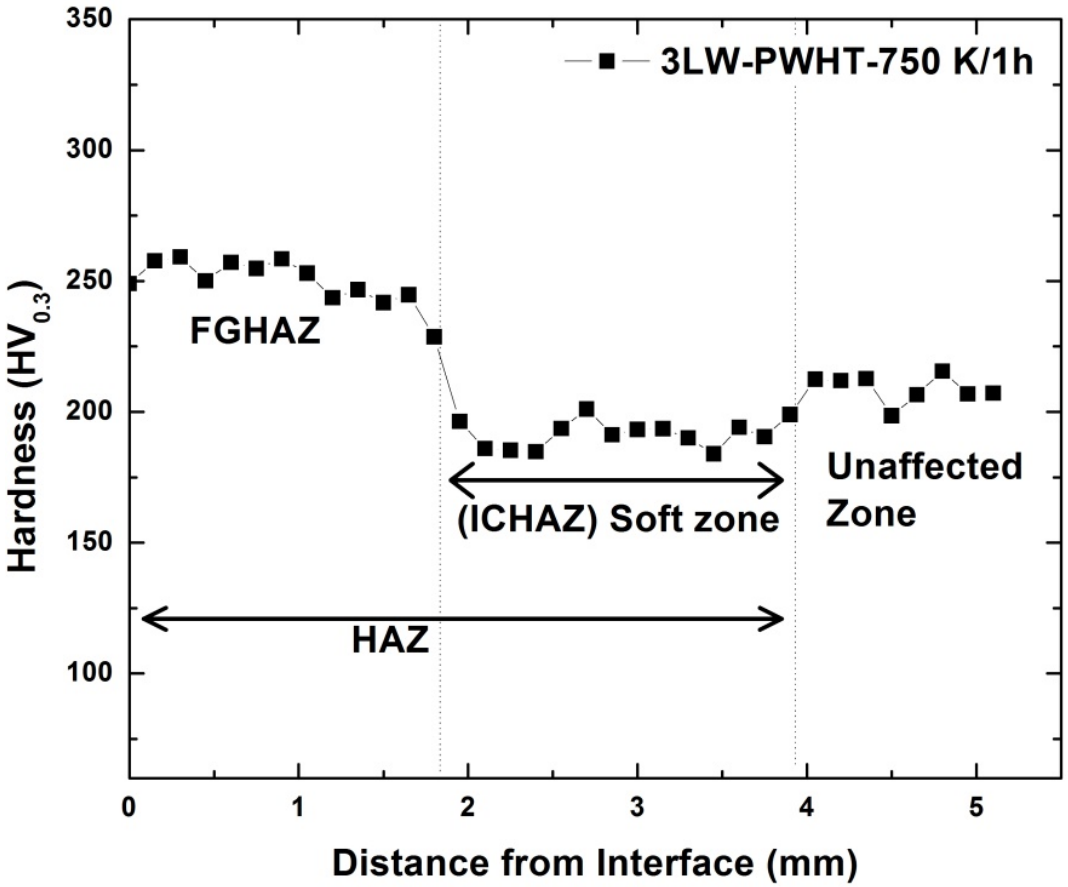


Figure 4.1 Hardness profile of three layer weld in PWHT condition on P91 HAZ and base metal side at the weld interface.

This increased hardness of the three layer weld (3LW) near the weld interface can be attributed to the grain refinement due to dynamic recrystallization as shown in Figure 4.2a and Figure 4.2b. It can be seen from Figure 4.2a and Figure 4.2b that the microstructure near the interface and even away from the interface is composed of very fine lath martensite structure. These fine grains were responsible for giving higher hardness in these zones and also reported in various works [2–4]. As one moves from the weld interface towards the base metal side, approximately 2 mm away from the interface, a sudden fall in hardness value was noticed.

This lower hardness region prevailed for a width of 2 mm followed by the unaffected base metal hardness zone. Figure 4.2c and Figure 4.2d show the microstructures corresponding to the lower hardness region (designated as the soft zone) and the unaffected zone, respectively. The microstructure of the soft zone HAZ of P91 consisted of big subgrains without the martensitic lath structure as shown in Figure 4.2c and Figure 4.3 (EBSD orientation map)**.** The absence of lath martensite could be responsible for showing such lower hardness in this region. To the best of our knowledge, the formation of the soft zone in the HAZ during friction welding of P91 is not reported in literature yet, though it is commonly observed in fusion welds of Cr-Mo steels.

This soft zone in the HAZ is normally located at the intercritical heat affected zone (ICHAZ) [5–7] where temperature during fusion welding reaches in between $AC_1$ and $AC_3$. The reduced strength in soft zone was attributed to the following reasons [6]: (a) replacement of lath martensite with large subgrains with low dislocation density, (b) coarsening of $M_{23}C_6$ carbides, and (c) reduction in misfit of carbonitride (V/Nb) particles with matrix due to its shape change from needle to spherical.

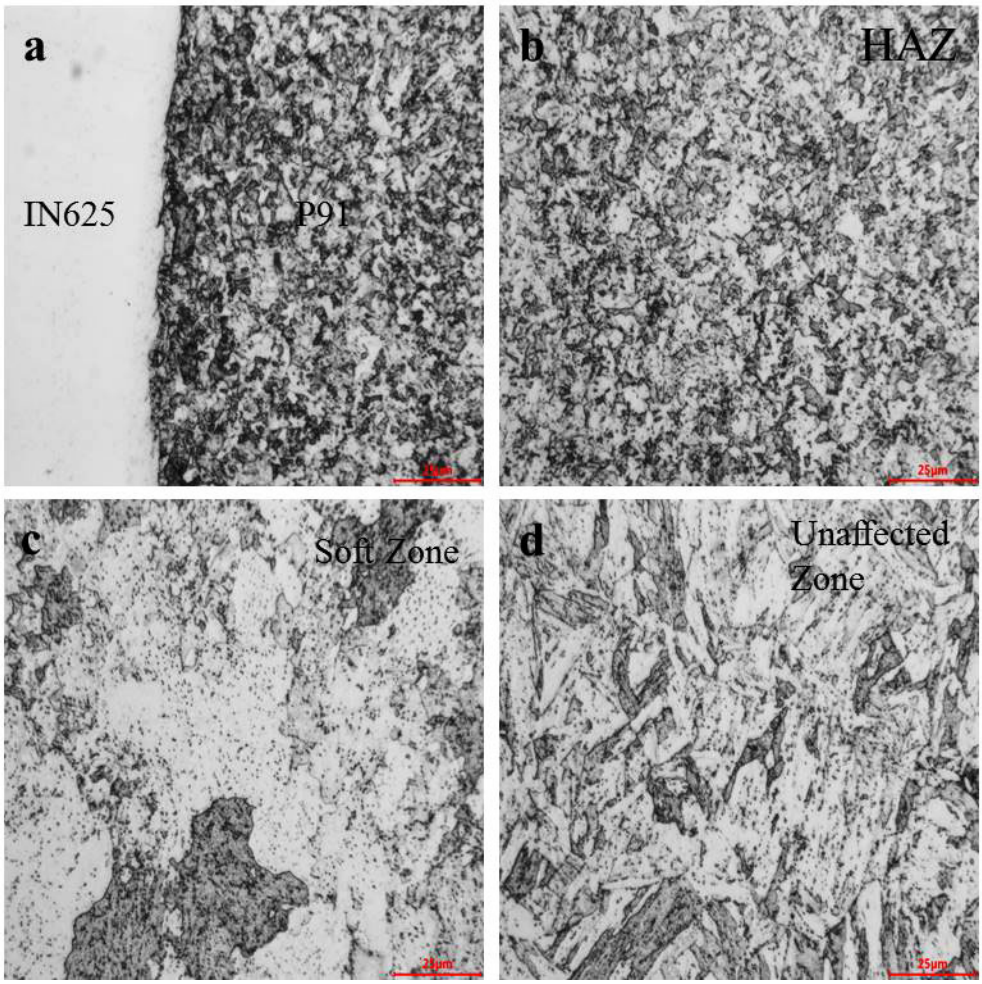


Figure 4.2 Microstructure of three layer weld in PWHT condition at (a) interface of P91 and IN625, (b) FGHAZ of P91, (c) soft zone of P91, and (d) unaffected zone of P91.

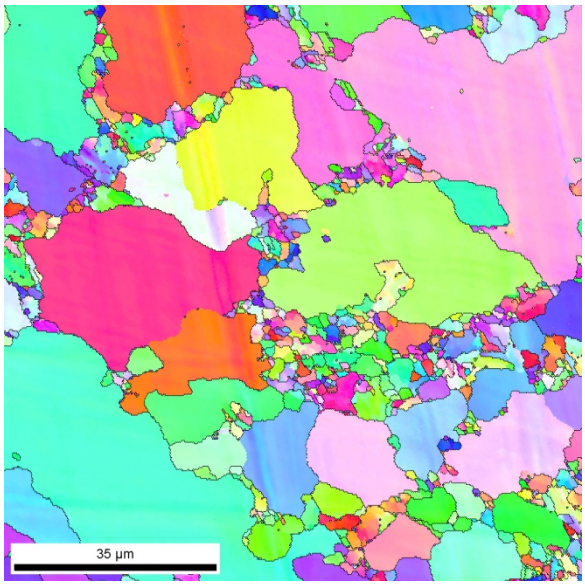


Figure 4.3 EBSD map of the soft zone of P91 HAZ of three layer weld in PWHT condition.

Laha et al. [6] carried out the TEM studies on P91 sample soaked at the intercritical region (1133 K) for 5 minutes followed by tempering at 1033 K for 1 hour. Their results showed the absence of lath martensite, presence of recrystallized grain, and coarsening of carbides. Similar results such as absence of lath martensite and presence of recrystallized grains in the soft zone HAZ of our PWHT samples were observed as shown in Figure 4.3. Dissolution of lath martensite is also possible by local diffusion of carbon between fresh transferred martensite which is lean in carbon content due to partial dissolution of carbides in austenite during intercritical heating and untransformed ferrite. Partial dissolution of carbides [8] and mixture of transformed martensite and untransformed ferrite [6] after intercritical heating were reported in literature. Therefore, the soft zone formation in friction welded specimens is also attributed to microstructural changes induced due to thermal exposure at the intercritical region (1023-1433 K, above $AC_1$ and below $AC_3$) during friction welding operation.

### 4.1.2 Heat treatment of three layer and single layer weld transition joint

#### 4.1.2.1 Three layer weld samples

In order to understand the microstructural changes and hardness after prolonged timings, an additional heat treatment is taken up. Three and single layer welds were subjected for post weld heat treatment at 973 K for different durations such as 100, 250, and 500 hours. This is in addition to the conventional post weld heat treatment after welding which was done at 1023 K for 1 hour. Figure 4.4 shows the interface microstructures of P91 and IN625 at different temperatures. The lath martensite structure is intact at the interface of the sample heat treated for 100 hours as shown in Figure 4.4a. On the other hand, sample heat treatment for 250 hours showed large grains without lath martensite (Figure 4.4b).With further exposure to 500 hours, the large grain region is expanded as shown in Figure 4.4c. The loss of lath martensite structure at the interface is also reflected in hardness values as shown in Figure 4.5.

Sample heat treated for 100 hours showed almost similar hardness values at the interface compared to the conventional PWHT (1023 K for 1 hour) sample. However, the width of the soft zone at ICHAZ is found to be more than found in the conventional PWHT sample. Initiation of the soft zone near the interface is seen first after 250 hours exposure as also reflected in sudden hardness drop close to interface. This soft zone was found to get extended with time. At 500 hours, the soft zone is extended throughout the HAZ, starting from the interface until the preexisting soft zone. This type of soft zone formation at the interface of dissimilar welds between Cr-Mo steels and austenitic steels was reported widely and attributed to carbon diffusion [9–15]. The carbon diffusion in such dissimilar joints was facilitated by the presence of chemical gradient across the

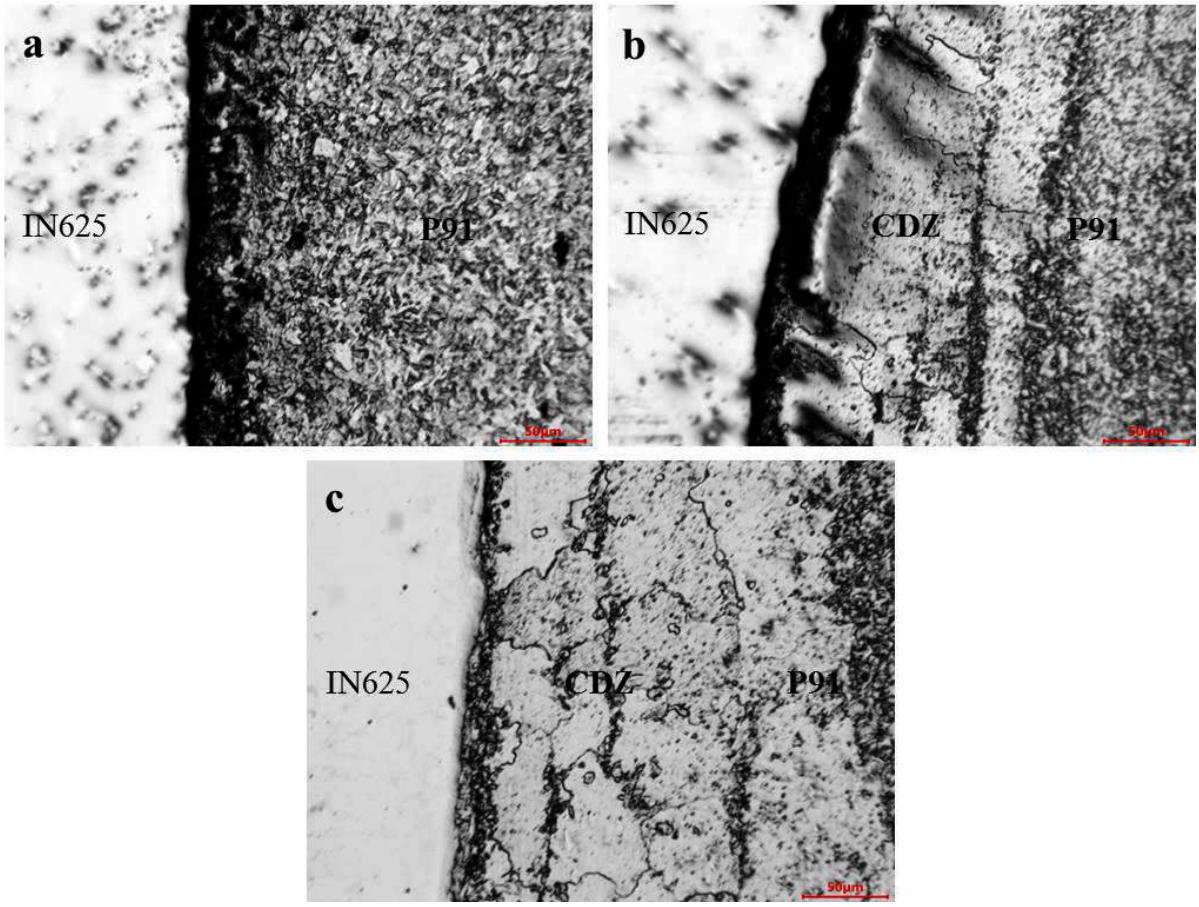


Figure 4.4 Three layer weld-interfacial microstructure between P91 and IN625 as a function of heat treatment time (a) 100, (b) 250, and (c) 500 hours at 973 K.

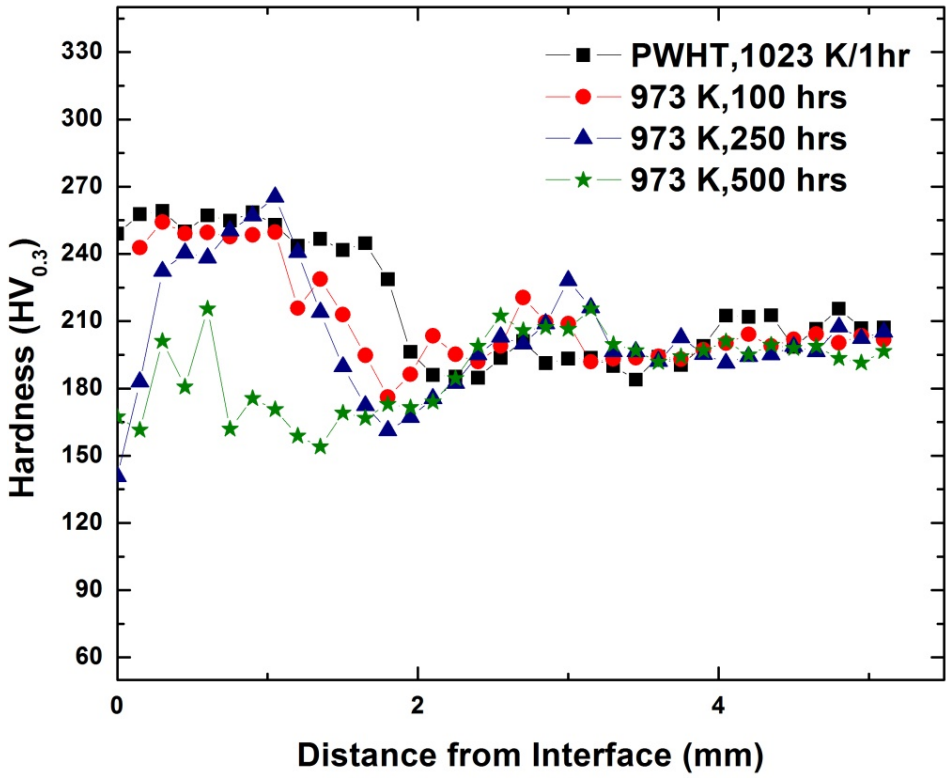


Figure 4.5 Hardness profiles of HAZ of P91 (Three layer weld) at the interface between P91 and IN625 as a function of heat treatment time (a) 100, (b) 250, and (c) 500 hours at 973 K.

interface such as carbon, chromium, and nickel gradient. Figure 4.6 shows the line scans of chromium, nickel, and iron contents across the interface of P91 and IN625 of three layer weld in PWHT condition. Figure 4.6 shows a sharp gradient of all the three elements at the weld interface.

The diffusion of carbon occurs from the high carbon content side (P91, 0.12 wt% C) to low carbon content side (IN625, 0.03 wt% C) material due to the downhill diffusion driven by carbon gradient. Carbon diffusion is also driven by chromium gradient as carbon diffuses from low the chromium content side to high chromium content side material, resulting in an uphill diffusion.

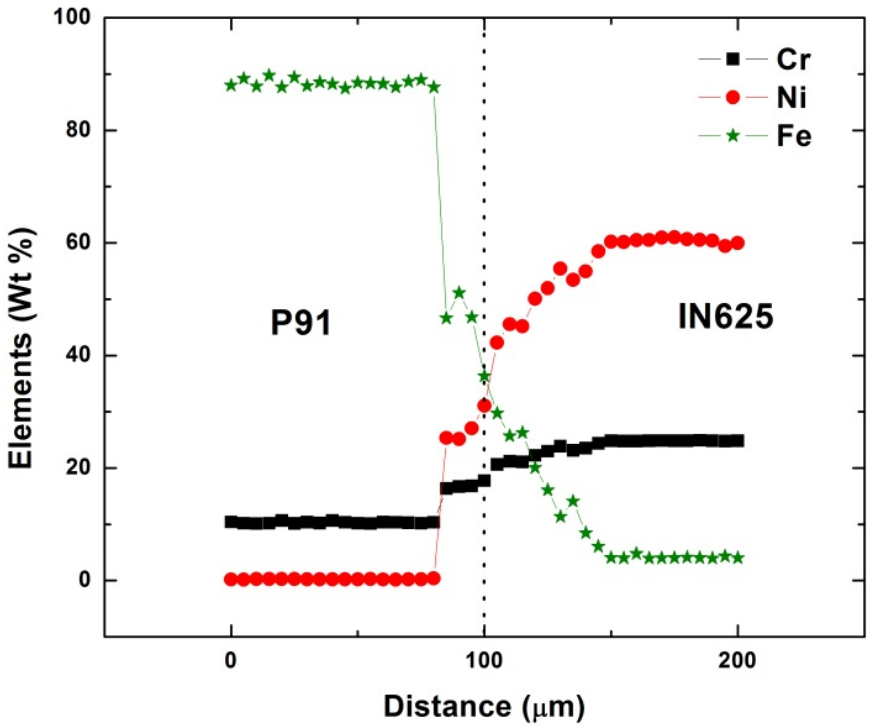


Figure 4.6 Chemical composition across the weld interface of P91 and IN625 (three layer weld-PWHT (1023 K for 1 hour).

As carbon diffusion progresses with time, one zone is left behind with a zone which is lean in carbon and the other side with enriched carbon. The carbon enriched zone is mostly present at the interface and grain boundaries of the materials and can be seen in Figure 4.4b and Figure 4.4c as dark etched area. For better clarity, the microstructure of the three layer weld sample heat treated for 500 hours is shown in Figure 4.7 at low magnification. The carbon enriched zones (dark etched area) are marked with arrows. These zones are found to be more segregated at the grain boundaries (located nonuniformly throughout the area) as shown in Figure 4.7. These carbon enriched zones also showed higher hardness values and are also reflected in hardness profile (Figure 4.5) (third, fourth, and fifth indentation from interface) of the three layer weld, heat treated for 500 hours.

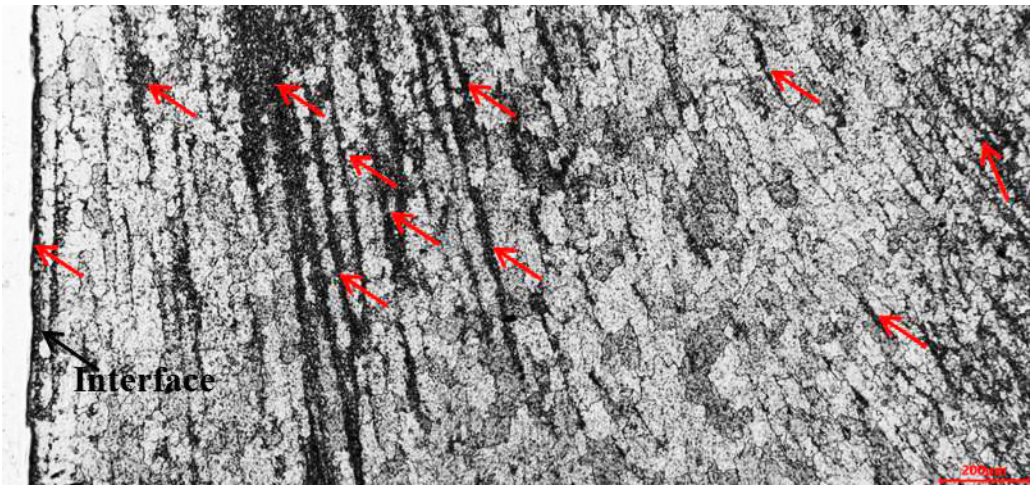


Figure 4.7 HAZ of P91 in three layer weld after heat treatment at 973 K for 500 hours.

Other features of these dark zones are their alignment; mostly form in parallel lines such as along prior lath boundaries. Figure 4.8 shows the line scan of chromium and carbon near the hard zone. The bright zone which is marked with a dotted square box represents the hard zone and the yellow line shows the scanned area (500 μm). It can be seen from the intensity peaks that the area corresponding to the hard zone (dotted square box) shows high intensity of chromium and carbon content as compared to the soft zone (solid square box). Higher magnification images corresponding to the hard zone (dotted square box) and the soft zone (solid square box) are shown in Figure 4.9. Figure 4.9a and Figure 4.9b are the SEM micrographs of the soft zone and the hard zone as indicated in Figure 4.8. It can be seen clearly that carbide density at the hard zone is more as compared with the soft zone. Analytical chemical composition of these carbides was confirmed by EDS analysis as shown in Figure 4.10. Peaks confirmed the presence of Cr, Mo, and C. These carbides are mostly decorated along the grain boundaries and seen in spherical shape. Size of these carbides is found to be relatively bigger than reported for base metal of tempered P91.

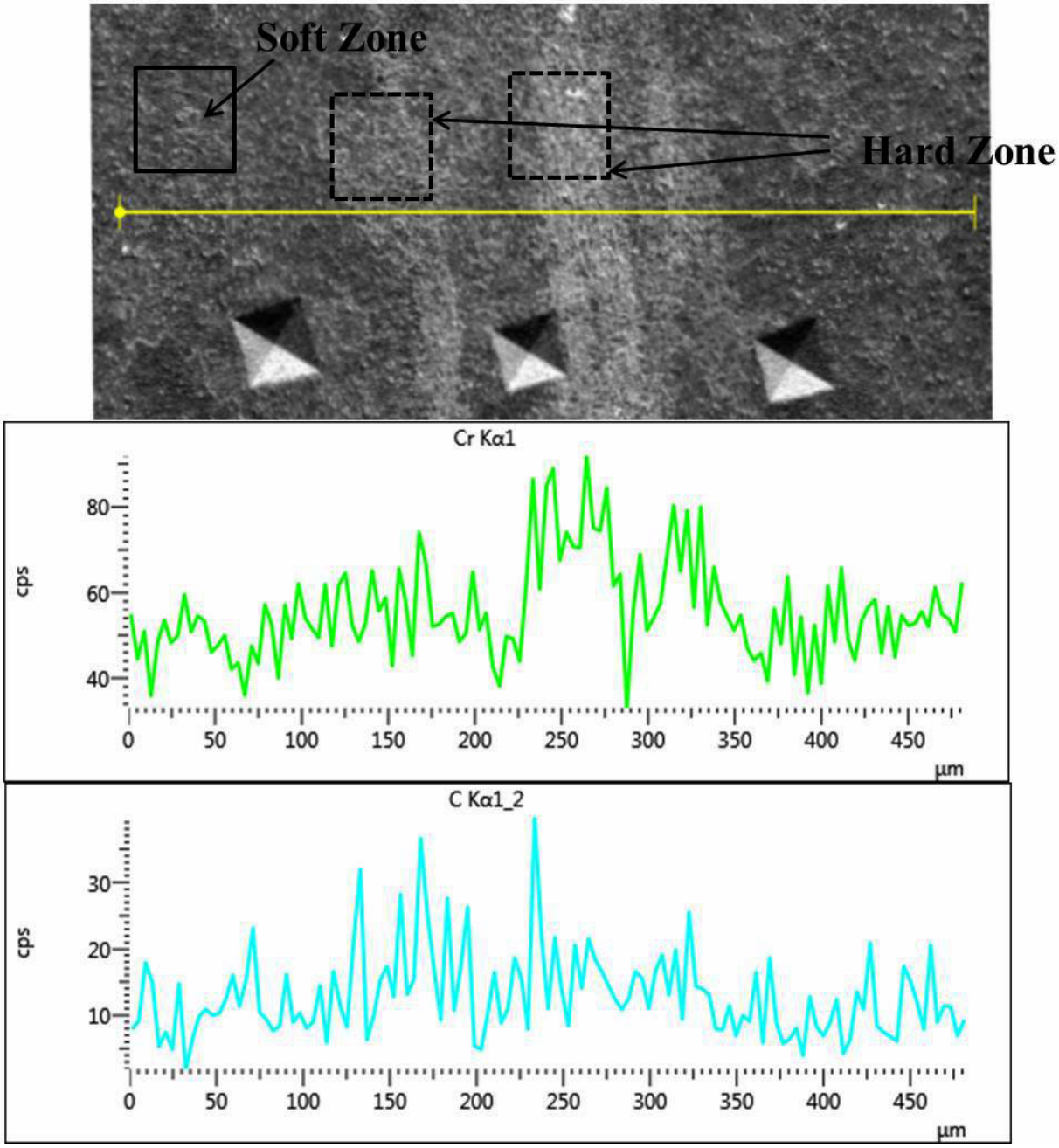


Figure 4.8 Line scan across hard and soft zones in three layer weld (P91 HAZ) PWHT 973 K for 500 hours.

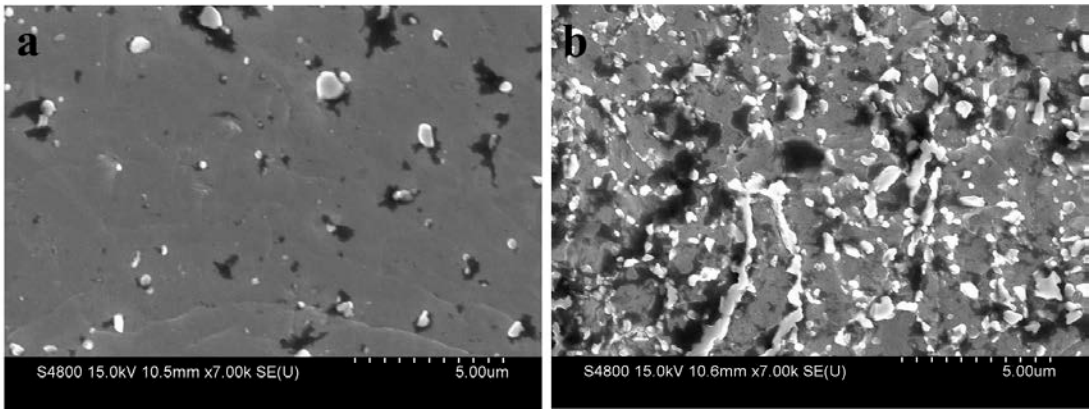


Figure 4.9 SEM micrograph showing presence of carbides at (a) soft zone and (b) hard zone in three layer weld (P91 HAZ) PWHT 973 K for 500 hours.

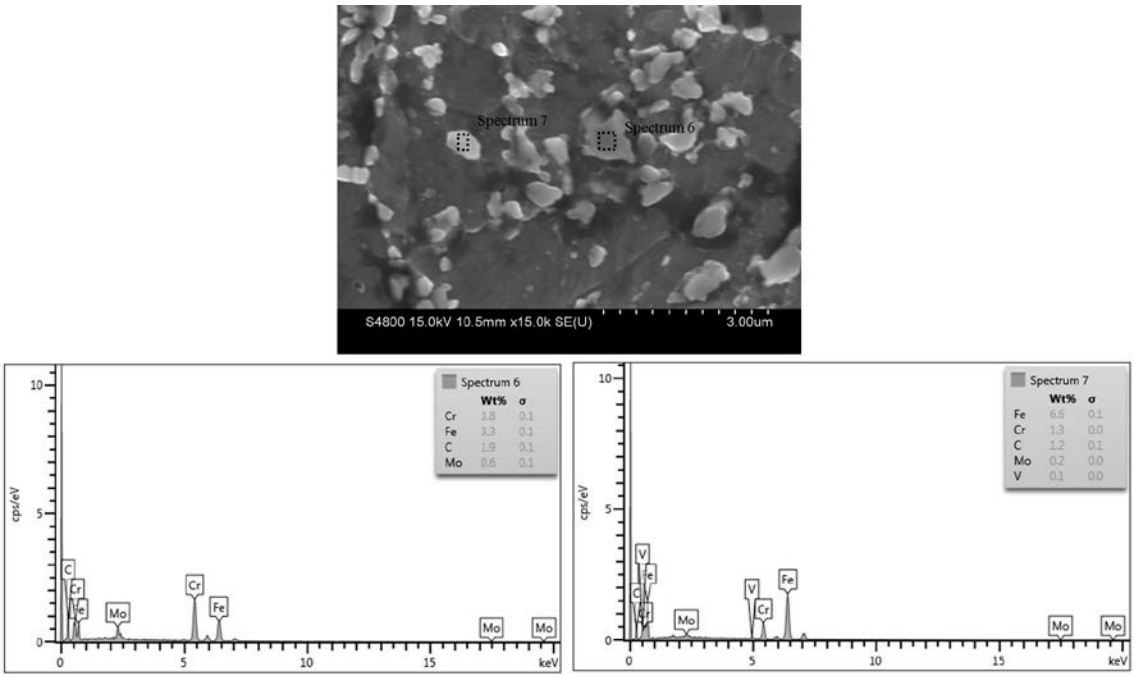


Figure 4.10 EDS spectrum on carbide particles of hard zone in three layer weld (P91 HAZ) PWHT 973 K for 500 hours.

4.1.2.2 Single layer weld samples

As done for three layer weld samples, single layer weld samples (IN600/P91) were also subjected for heat treatment at 973 K for different time periods, 100, 250, and 500 hours. This heat treatment is in addition to the conventional post weld heat treatment after welding which was done at 1023 K for 1 hour. Figure 4.11a, 4.11b, and 4.11c show the interface microstructures of P91 and IN600 heat treated at 973 K for 100, 250, and 500 hours, respectively. It can be seen from the microstructures that in all the cases, lath microstructure are intact on the P91 side and also reflected in hardness values as shown in Figure 4.12. As time proceeded, the hardness values near the interface decreased. However, no soft zone near the interface was observed. This is in contrast to the three layer welds, where a soft zone near the interface was noticed (Figure 4.5). Reduced hardness near the interface may be due to over tempering during heat treatment.

Better performance of IN600 as a barrier at the interface could be attributed to the difference in chemical composition of these two alloys (IN625 and IN600) which help stop the diffusion of carbon. Although they are nickel-based alloys, percentage of nickel and chromium is different in both of these alloys. For example, IN600 contains 72 wt% of nickel and 18 wt% of chromium whereas IN625 contains 65 wt% of nickel and 22 wt% of chromium. It is reported that for dissimilar welds, the higher the percentage of nickel content at the weld interface, the lower will be the diffusion of carbon [11,15]. Apart from nickel content, presence of chromium gradient across the interface is also another factor for fast carbon diffusion. Therefore, formation of a soft zone near the interface due to carbon diffusion in three layer welds could be attributed to the lower amount of nickel content and higher chromium gradient present at the interface.

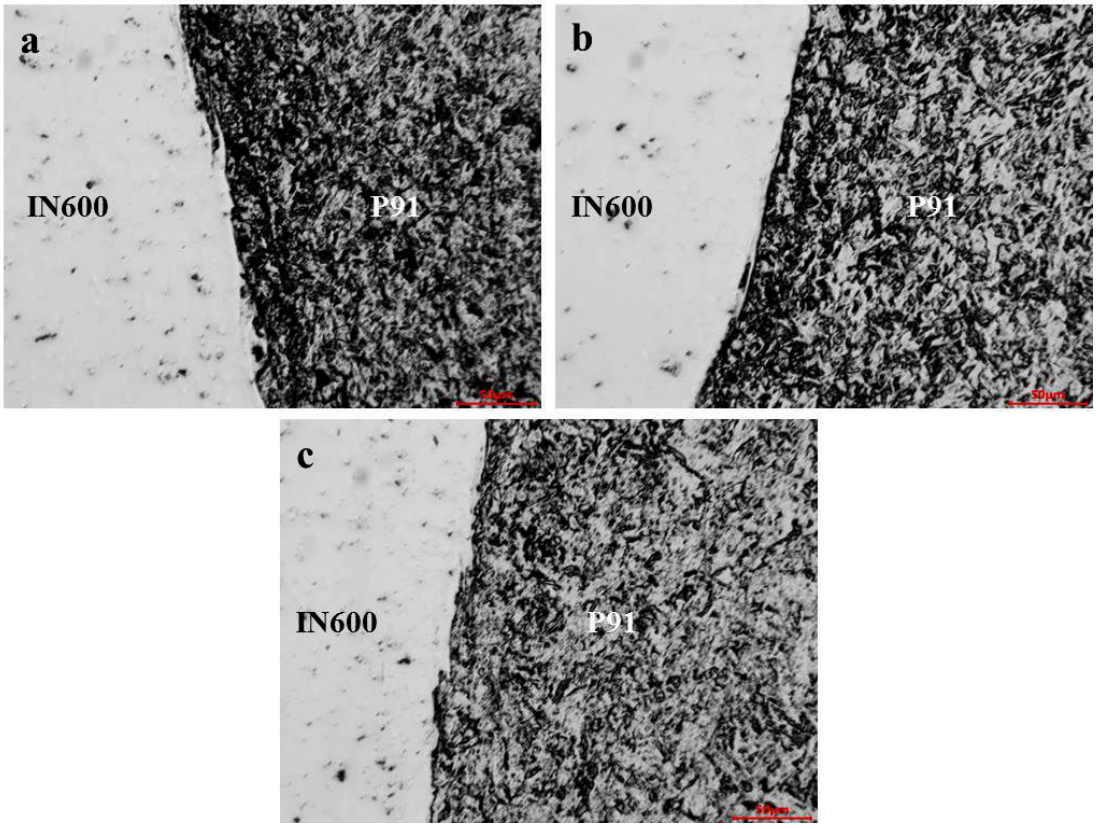


Figure 4.11 Interfacial microstructure of P91 and IN600 (single layer weld) as a function of heat treatment time (a) 100, (b) 250, and (c) 500 hours at 973 K.

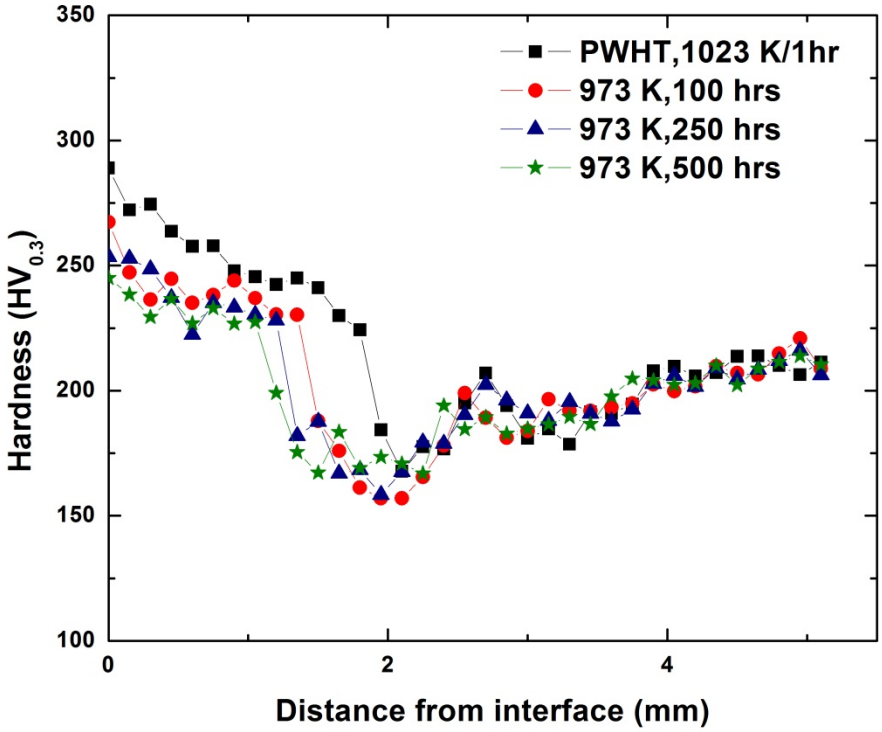


Figure 4.12 Hardness profile across P91 HAZ (single layer weld) as a function of heat treatment time (a) 100, (b) 250, and (c) 500 hours at 973 K.

It is observed that as time increased, the width of the soft zone at the HAZ increased and can be seen in the hardness profile for both the single and three layer welds (Figure 4.5 and Figure 4.12). Comparison of soft zone width in the three layer weld is shown in Figure 4.13. Figure 4.13a and Figure 4.13b show the width of soft zone formation in the three layer weld after PWHT at 1023 K for 1 hour and heat treatment at 973 K for 100 hours.

It is also noticed that the soft zone moving front is towards the interface in the FGHAZ and it is also reflected in the hardness profile. Susceptibility of FGHAZ towards dissolving the martensite structure could be due to presence of unstable martensite (lean carbon content). This region during welding experiences a temperature somewhere more than $AC_3$ (next to intercritical region), where it transforms to austenite. However, due to insufficient time, carbides dissolution is not complete. Therefore, it is likely that the transformed martensite would have a lean percentage of carbon after cooling. During subsequent heat treatment at 1023 K for 1 hour, new precipitates will nucleate and start growing by taking the carbon from the unstable martensite. This results in dissolution of martensite lath structure into large subgrains. Further, the carbon diffusion will be motivated by the presence of carbon gradient between fine grain martensite in the HAZ and preexisting soft zone. Figure 4.9b also shows the evidence of excess precipitates in the hard zone which is larger in size and higher in number next to the large subgrains. High recovery rate of excess dislocations is also reported in FGHAZ which leads to large subgrain formation and precipitation coarsening [16].

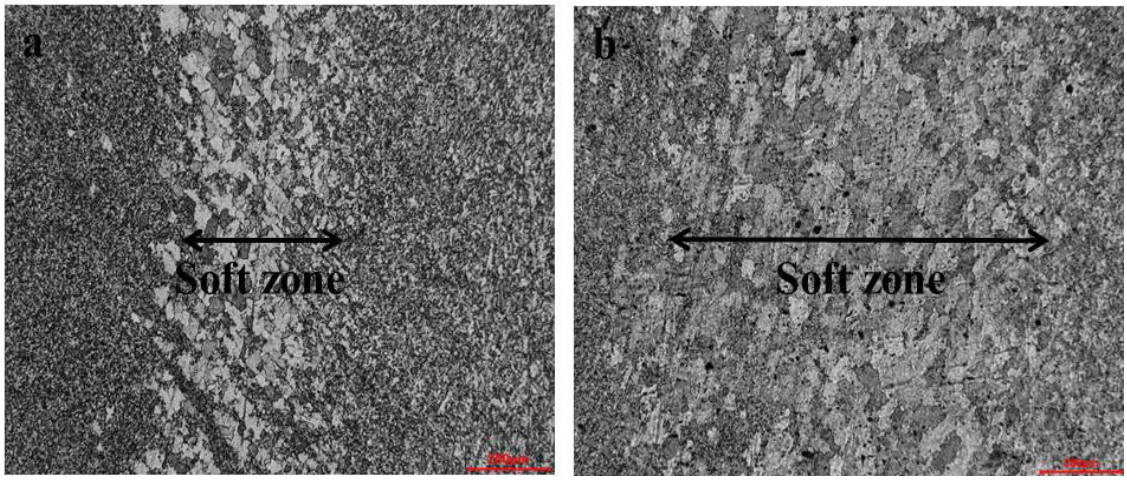


Figure 4.13 Soft zone formation after (a) post heat weld treated at 1023 K for 1 hour (b) heat treatment at 973 K for 100 hours.

### 4.1.3 Conclusions

1) The soft zone in the HAZ of P91 was observed 2mm away from the weld interface for both single and three layer welds and is attributed to the intercritical heating (between $AC_1$ and $AC_3$) during welding operation. The replacement of lath martensite with large subgrains is responsible for reduced strength of the soft zone in HAZ of P91.

2) The weld interface between P91 and IN625 showed soft zone formation whereas the interface between P91 and IN600 did not show such a soft zone. Soft zone formation near the weld interface is attributed to the carbon diffusion. Better performance of IN600 as a carbon barrier is due to the presence of high nickel content and less gradient of chromium at the interface as compared to IN625.

3) The moving front of soft zone was observed towards FGHAZ. Dissolution of lath martensite in FGHAZ is attributed to unstable martensite formation during welding operation. The transformation of unstable martensite to subgrains was found to be helped by the carbides precipitation and presence of local carbon gradient between the

preexisting soft zone and fine grained HAZ.

## 4.2 Creep behavior of dissimilar metal weld joints

### 4.2.1 Experimental method for stress rupture test

A stress rupture test was performed using a canti-lever beam test set up with a 20:1 lever arm ratio. Tests were carried out at different temperatures between 823 K to 973 K and stresses between 75 MPa to 250 MPa. Stress rupture tests were performed on post weld heat treated (1023 K, 1 hour/air cooled) samples only. Figure 4.14 shows a typical test specimen indicating dimensions. The gauge length (15 mm) consisted of five materials (P91, IN 625, IN 600, IN 800H, and AISI 304) having 3 mm thickness each. Some of the tests were interrupted before final fracture due to time constraint.

### 4.2.2 Results and discussion

#### 4.2.2.1 Microstructure of base metal

Figure 4.15a and 4.15b show the SEM pictures of modified 9Cr-1Mo (P91) steel in the normalized and tempered condition at lower and higher magnifications, respectively. Microstructure of normalized and tempered base material consisted of tempered martensite as shown in Figure 4.15a. Mechanisms by which this high alloy steel strengthen are as follows: solution hardening, precepitiation or dispersion hardening, dislocation hardening, and boundary or sub-boundary hardening [17]. However, creep strength of this high alloy steel (P91) comes siginificantly from precipitation hardening in addition to other hardening mechanisms. Several types of carbonitrides and intermetallic compounds are present at the grain boundaries and in the matrix.

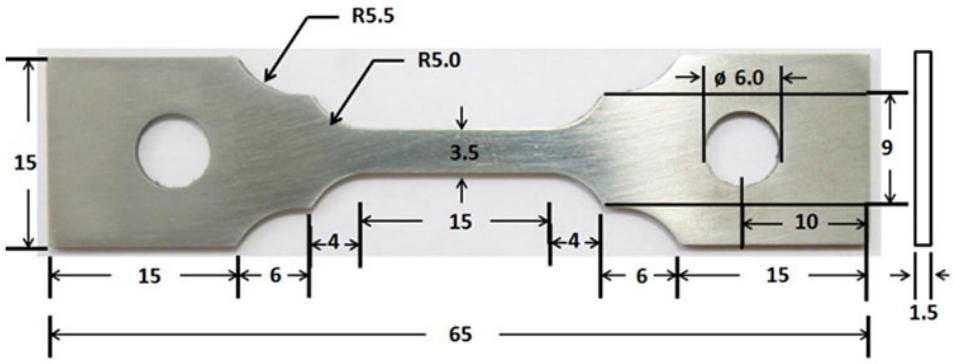


Figure 4.14 Flat creep specimen (all dimension in mm).

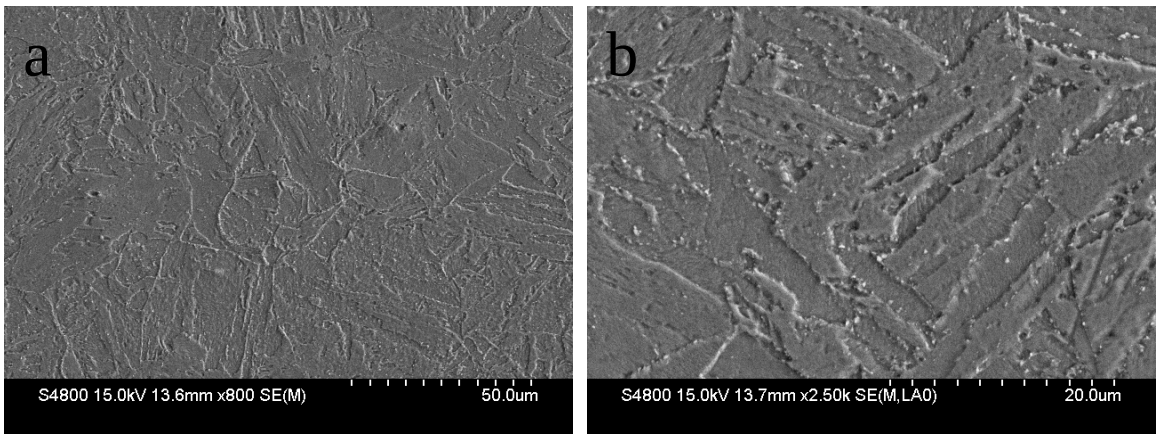


Figure 4.15 SEM micrographs (secondary electron images) showing microstructure of as received P91 steel (a) lower (b) higher magnification.

Typical carbides and carbonitrides include $M_{23}C_6$, $M_6C$, $M_7C_3$, MX, and $M_2X$, where M stands for a metallic element such as Cr, Mo, Nb, and V and X stands for carbon and nitrogen atoms. The volume percenage of $Cr_{23}C_6$ precipitates are almost 2% whereas MX type precipitates are close to 0.2% [17]. The size and shape of these two types of precipitates are also different: $M_{23}C_6$ carbides are present in the rod shape which are larger in size as compared to smaller, spherical MX-type precipitates [18]. Figure 4.15b is a higher magnification picture of P91, with carbides (white particles) at grain boundaries of lath martensite.

4.2.2.2 Stress rupture behavior: comparison between single and three layer welds

A typical creep curve consists of three stages: 1) primary, 2) secondary, and 3) tertiary. In the primary stage, the creep rate decreases due to work hardening via dislocation multiplication and interaction. In the secondary (or steady state) creep stage, the creep rate is relatively constant due to balance between work hardening and recovery effect. Finally, in the tertiary stage, the creep rate increases rapidly because cavities/voids start growing leading to final failure. In this study, all the creep curves showed three distinct regions: primary, secondary, and tertiary regions as shown in Figure 4.16. Figure 4.16 shows a typical creep curve of a three layer weld (3LW) tested at 873 K and 200 MPa. Three layer welds (3LW) were compared with single layer welds (SLW). Figure 4.17a and Figure 4.17b show the comparision of creep curves between three and single layer welds tested at 873 K/200 MPa and 923 K/125 MPa, respectively. Results showed improved creep life for three layer welds under both of these conditions.

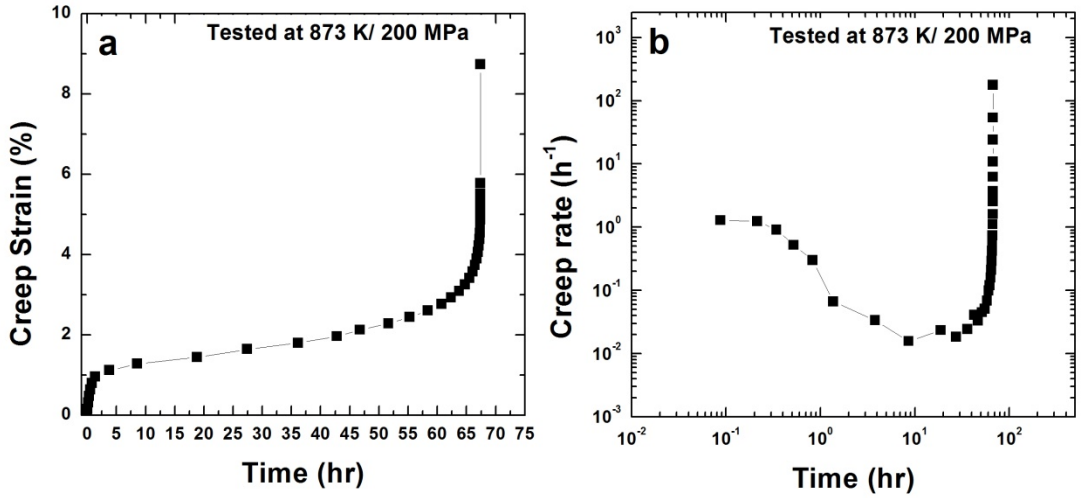


Figure 4.16 Plot between (a) creep strain vs. time (b) creep rate vs. time of three layer weld (3LW) tested at 873 K and 200 MPa.

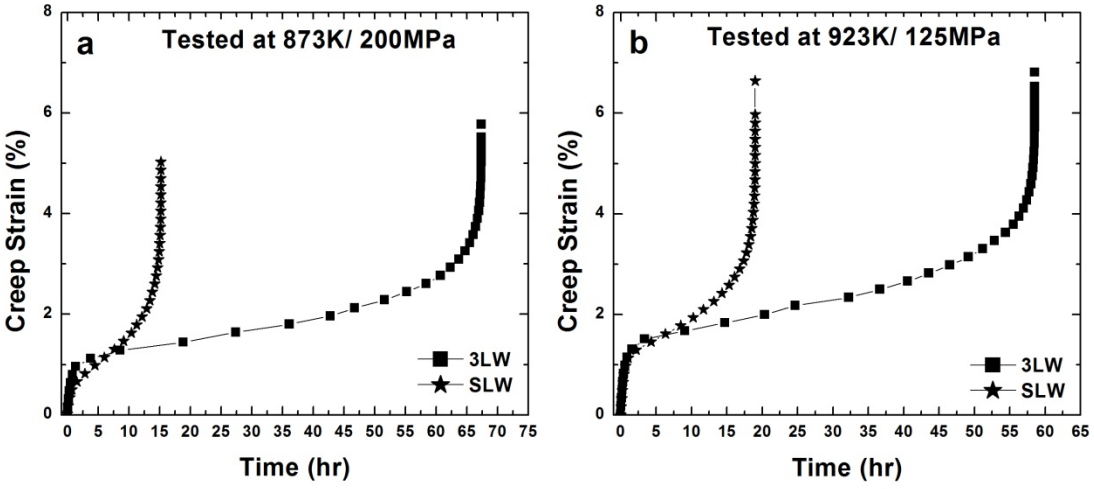


Figure 4.17 Comparison between creep curves of weld joints of single and three layer welds tested at (a) 873 K and 200 MPa, and (b) 923 K and 125 MPa.

For example, the rupture life of a single layer weld crept at 873 K and 200 MPa was 15.2 hours, whereas the three layer weld ruptured after 67.4 hours. Similarly, the rupture life for a three layer weld crept at 923 K and 125 MPa was 58 hours whereas for the single layer weld, it was only 28 hours. Figure 4.18 is a plot between rupture time and stress of all the single layer and three layers welds. The graph compares the rupture time of single layer and three layer welds tested at different temperatures and stress levels. A limited number of single layer welds were tested for comparison purpose. It can be seen from Figure 4.18 that, irrespective of test temperatures and stress levels, three layer welds performed better than single layer welds. Figure 4.19 shows the hardness profile of three and single layer weld crept at 923 K and 125 MPa. The failure location is located in the preexisting soft zone region and can be seen in the hardness profile of three and single layer welds compared with PWHT sample (1023 K/1hour). The failure location of all the three and single layer welds was found to be in the preexisting soft zone which is around 2 mm away from the weld interface. The soft zones near the fracture tips were also noticed in the microstructures as shown in Figure 4.20. Figure 4.20a and Figure 4.20b are the microstructures of a three layer weld tested at 923 K and 125 MPa at the interface and fracture tip, respectively. Figure 4.20c and Figure 4.20d are the microstructures of a single layer weld tested at 973 K and 125 MPa at the interface and fracture tip, respectively. Both three and single layer welds showed a soft zone near the fracture tip as indicated by arrow marks in Figure 4.20b and Figure 4.20d. The interfacial microstructure of both three and single layer welds does not show any soft zone formation near the interface, as shown in Figure 4.20a and Figure 4.20c. However, three layer weld heat treated samples showed formation of a soft zone near interface as shown

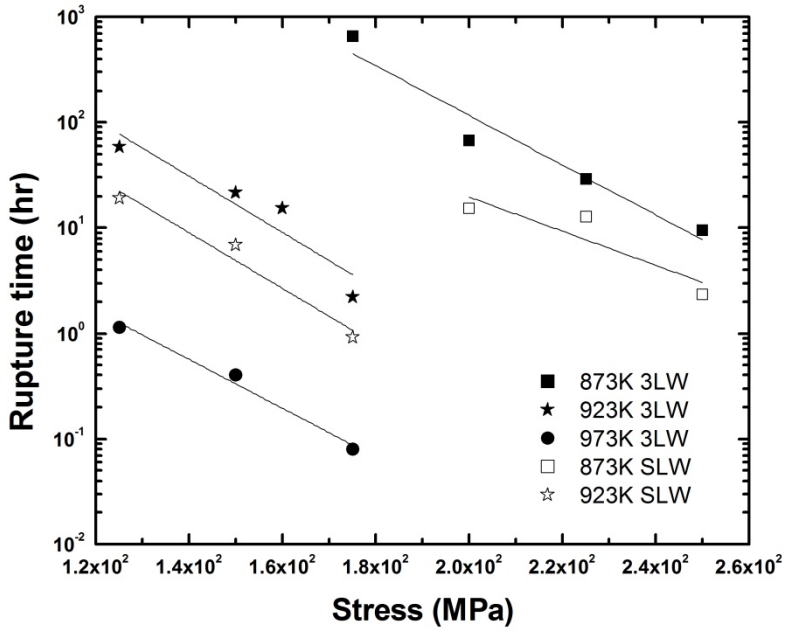


Figure 4.18 Plot between rupture time and stress for three and single layer weld at different temperatures and stress levels.

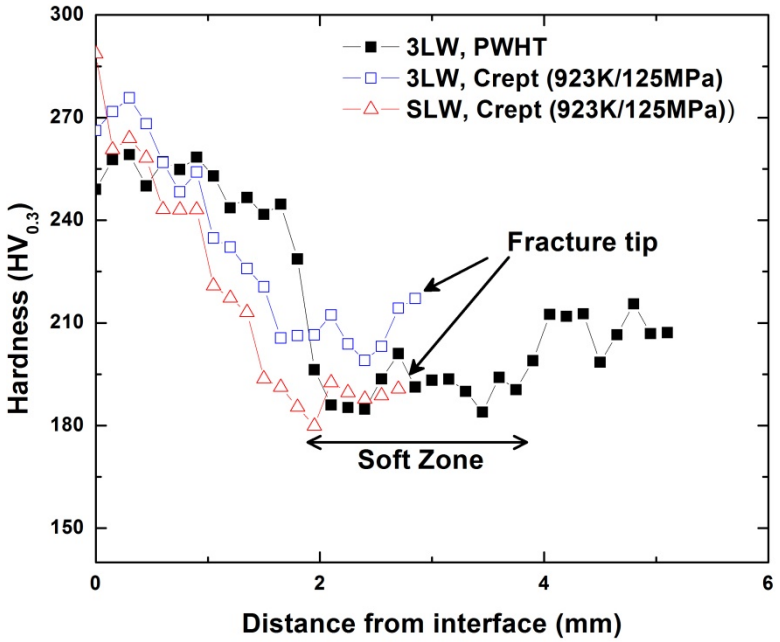


Figure 4.19 Hardness profile of three and single layer weld crept at 923 K and 125 MPa.

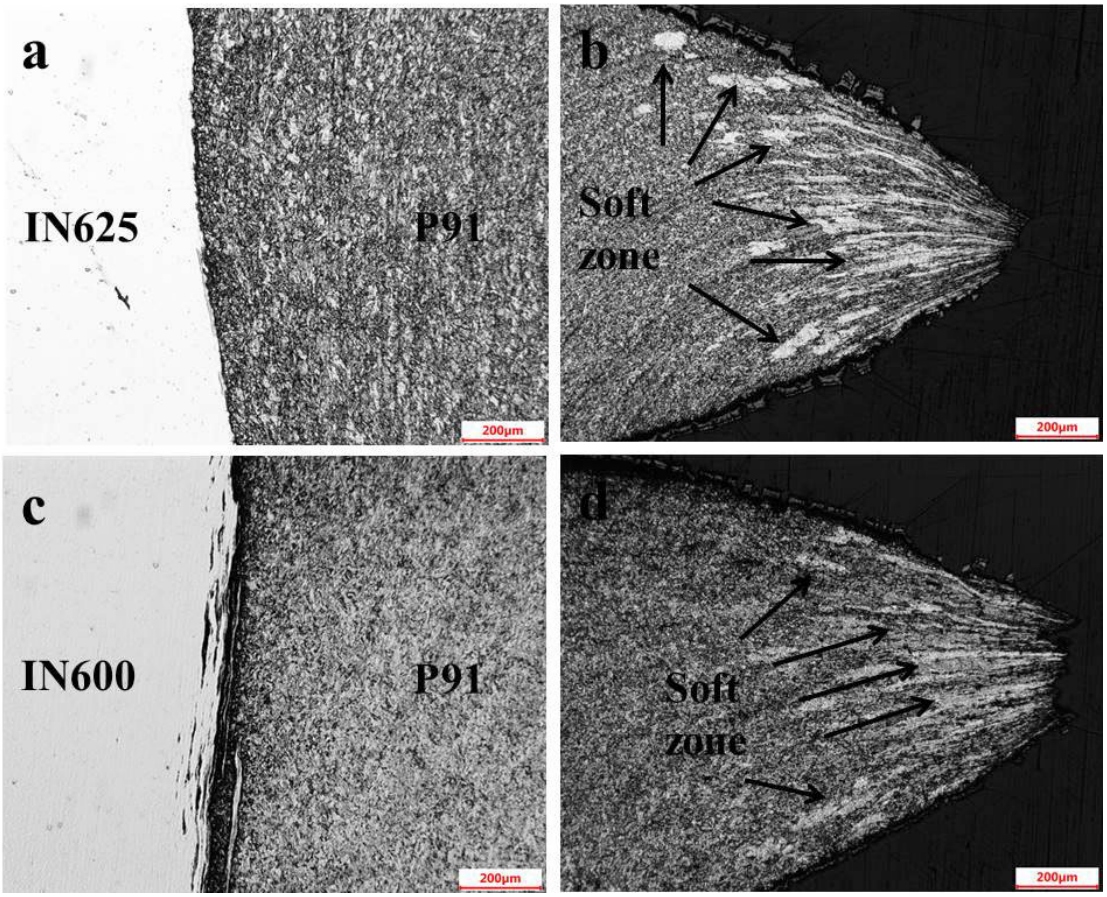


Figure 4.20 Optical micrograph of three layer weld at (a) interface (P91 and IN625) (b) fracture tip and single layer weld at (c) interface (P91 and IN600) (d) fracture tip tested at 923 K and 125 MPa.

in Figure 4.4. The absence of a soft zone near the interface in the three layer weld should be due to shorter rupture time and lower temperature than heat treated sample. At this point, both these welds showed similar microstructure; however, three layer welds performed better than the single layer weld. The only possible reason which would help increase the life of three layer welds is gradient in coefficient of thermal expansion.

It has been reported that the presence of inhomogeneous microstructure across the interface develops stress concentration and stress triaxiality which also promotes the failure of dissimilar weld joints [19]. Similarly, in the three and single layer welds apart from inhomogeneous microstructure across the weld interface, another factor which contributes to stress concentration is mismatch in CTE value. In a single layer weld, the transition is provided but not as gradual as compared to the three layer weld; therefore, increased rupture life of a three layer weld can be attributed to the gradual transition in CTE value from austenitic to ferritic side.

#### 4.2.2.3 Fractography of crept specimens

Figure 4.21a and Figure 4.21b show the fractographs of the sample crept at 873 K/175 MPa and 873 K/200 MPa, respectively. Both the fractured surfaces showed dimple patterns with multiple numbers of cavity and voids. The dimple pattern is a characteristic feature of transgranular mode of facture. The transgranular mode of fracture in 9Cr-1Mo steel was also reported by Shrestha et al. [20] and Choudhary et al. [21]. It is observed that the size and number density of creep voids are different at different operating conditions. Larger size of creep voids is observed at low applied stress (175 MPa) as compared to sample tested at high applied stress (200 MPa).

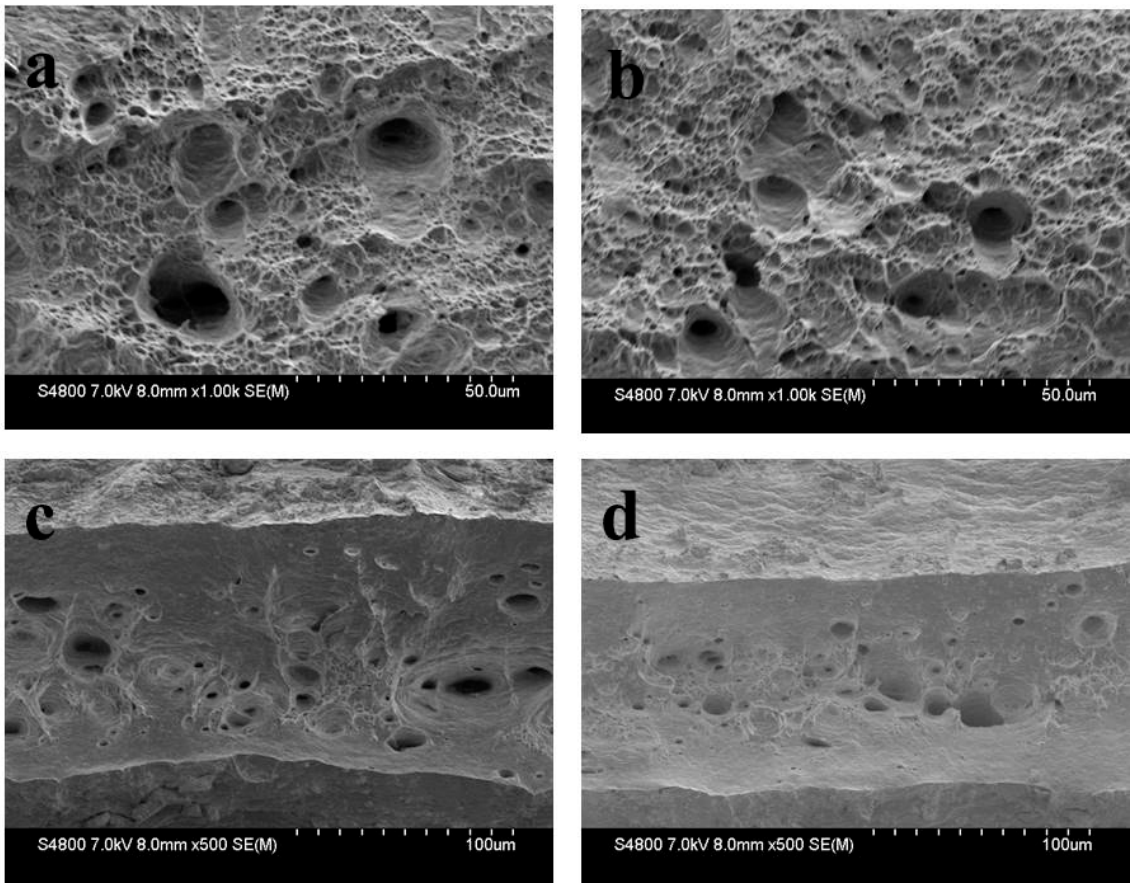


Figure 4.21 SEM micrograph (secondary electron images) of crept sample: (a) fractured surface tested at 873 K and 175 MPa, (b) fracture surface tested at 873 K and 200 MPa, (c) cross section view tested at 923 K and 125 MPa, and (d) cross section view tested at 923 K and 150 MPa.

However, the density of creep voids is higher at higher stress as shown in Figure 4.21b. Higher density of creep voids is due to accelerated plastic deformation during high applied stress. On the other hand, large size of voids is attributed to duration of the sample exposed to such elevated temperature. Figure 4.21c and 4.21d show the cross section area near the fractured tip, tested at 923 K/125 MPa and 923 K/150 MPa, respectively. Smaller cross section area is observed at high applied stress as compared to a lower one. Table 4.1 represents the reduction in area and true strain to fracture at different temperatures and stresses.

Increased reduction in area and true strain is observed with increased temperature and stress. Similar behavior is also reported by Shrestha et al. [20] in modified 9Cr-1Mo steel. Accelerated void formation, coalescence of microvoids, and plastic flow at high temperature and stress levels result in high percentage of area reduction and fracture strain.

#### 4.2.2.4 Creep deformation mechanism of weld joints

Figure 4.22a and Figure 4.22b show the comparison of creep curves of a three interlayer weld as a function of stress and temperature. Figure 4.22a shows the creep curve comparison tested at 923 K as a function of applied stress. It can be seen that the creep rate increased and rupture time decreased with increasing applied stress. Figure 4.22b shows the comparision of creep curves tested at 175 MPa as a function of temperature. Similar trends were observed as observed above. Norton power law was used to analyze the stress dependence of minimum creep rate. Figure 4.23a shows a double logarithmic plot of minimum creep rate and stress at 873, 923, and 973 K.

Table 4.1 Summary of percentage reduction in area and true fracture strain of the specimens tested at different temperatures and stresses.

| Temp. | 873K | | | | 923K | | | 973K | | |
|---|---|---|---|---|---|---|---|---|---|---|
| Stress (MPa) | 175 | 200 | 225 | 250 | 125 | 150 | 175 | 125 | 150 | 175 |
| Three layer welds (3LW) | | | | | | | | | | |
| Reduction in area (%) | 94.5 | 95.0 | 96.0 | 96.6 | 95.8 | 96.8 | 96.9 | 95.3 | 96.4 | 96.5 |
| $\varepsilon_f$ | 2.90 | 3.0 | 3.23 | 3.38 | 3.18 | 3.44 | 3.46 | 3.05 | 3.32 | 3.36 |
| Single layer welds (SLW) | | | | | | | | | | |
| Reduction in area % | --- | 95.9 | 95.9 | 96.7 | 95.9 | 96.6 | 96.9 | --- | --- | --- |
| $\varepsilon_f$ | --- | 3.2 | 3.2 | 3.4 | 3.2 | 3.4 | 3.5 | --- | --- | --- |

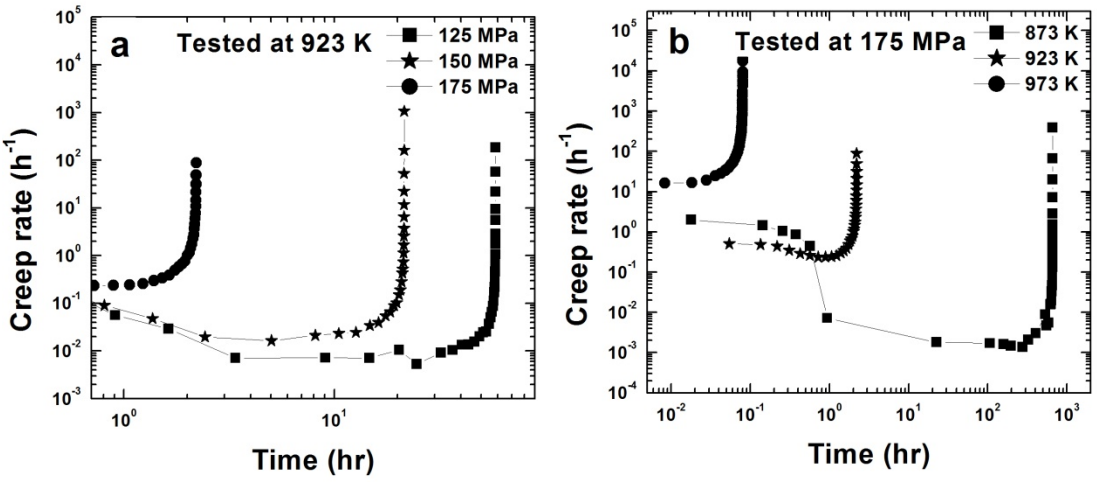


Figure 4.22 Variation in creep rates as a function of (a) stress and (b) temperature for three layer welds.

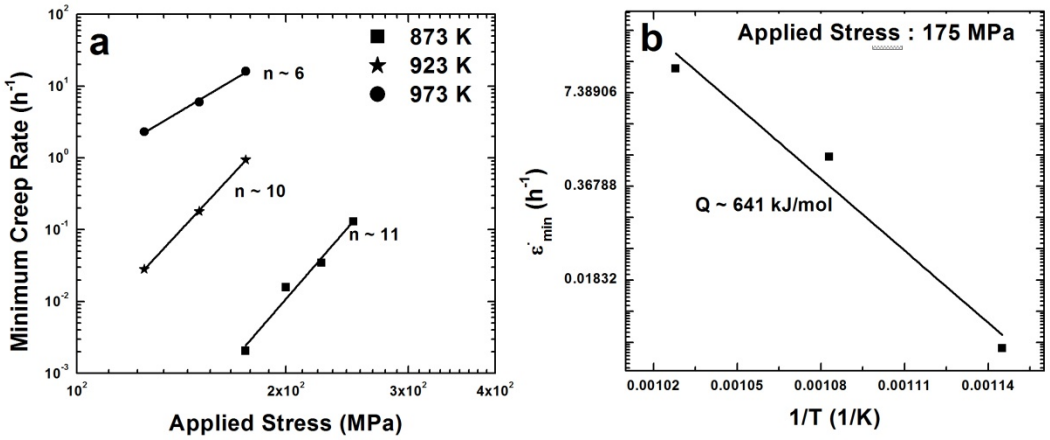


Figure 4.23 Log-log plot between minimum creep rate vs. applied stress (a) and plot between minimum creep rate vs. inverse of temperature for apparent activation energy calculation (b).

The slope of logarithmic plot between minimum creep rate and stress gives the stress exponent ($n$). The stress exponent ($n$) obtained for 873, 923, and 973 K is approximately 11, 10, and 6, respectively. The apparent activation energy of about 641 kJ/mol is obtained for the test performed at stress of 175 MPa as shown in Figure 4.23b.

Such high values of stress exponent and activation energy were reported previously in a number of studies. Shrestha et al. [18] reported the stress exponent of 11 at high stress regime with an activation energy of 510 kJ/mol for the monolithic Grade 91 specimen. Choudhary et al. [21] reported activation energy of 621 kJ/mol and stress exponent of 12 at a test temperature range of 823 K to 873 K. In both of their works, decreased stress exponent was observed with increased temperature and these studies were carried out on unwelded creep samples. High stress exponent 22 and activation energy of 1,117 kJ/mol was reported by Anderson et al. [22] for samples tested at high stress (220 to 240 MPa) regime. They indicated that the stress exponent and activation energy shift to lower values at low stress and high temperature regime.

The applied stress in the present work is more than 100 MPa which is intermediate to high stress regimes. Therefore, high values of stress exponent and activation energy obtained in the present work are also in agreement with reported work in literature. Decreasing stress exponent value is observed with increasing temperature. Lower value of stress exponent at high temperature could correspond to dissolution of precipitates at elevated temperature which is also in agreement with the previously reported works. It is noted that higher stress exponent and activation energy more than the normal values require incorporation of threshold stress which arises due to the interruption of dislocation motion by fine particles. In Grade 91 steels, MX type particles

can help in creating this kind of effect. Different approaches were taken to calculate the threshold stress as reported in literature [18,23–25]. In the present work, linear extrapolation method as adopted by Shrestha et al. [18], Mishra et al. [25], and Huang and Langdon [26] is used to calculate the threshold stress.

Minimum creep rate raised to the power of the inverse stress exponent versus modulus compensated stress is plotted with possible stress exponent as shown in Figure 4.24. Stress exponent was varied from 3 to 6 to find out the operating creep mechanism between viscous glide ($n$ = 3) and dislocation climb ($n$ = 5). Figure 4.24a and Figure 4.24b show the plots when stress exponents were chosen as 3 and 5, respectively. At $n$ = 3, the correlation coefficients of 0.96, 0.97, and 0.98 were obtained at 873, 923, and 973 K, respectively. At $n$ = 5, the correlation coefficients of 0.98, 0.99, and 0.99 were obtained at 873, 923, and 973 K, respectively. Better fit was found for stress exponent of 5 as compared to 3. The stress exponent less than 3 resulted in poor fit. The threshold

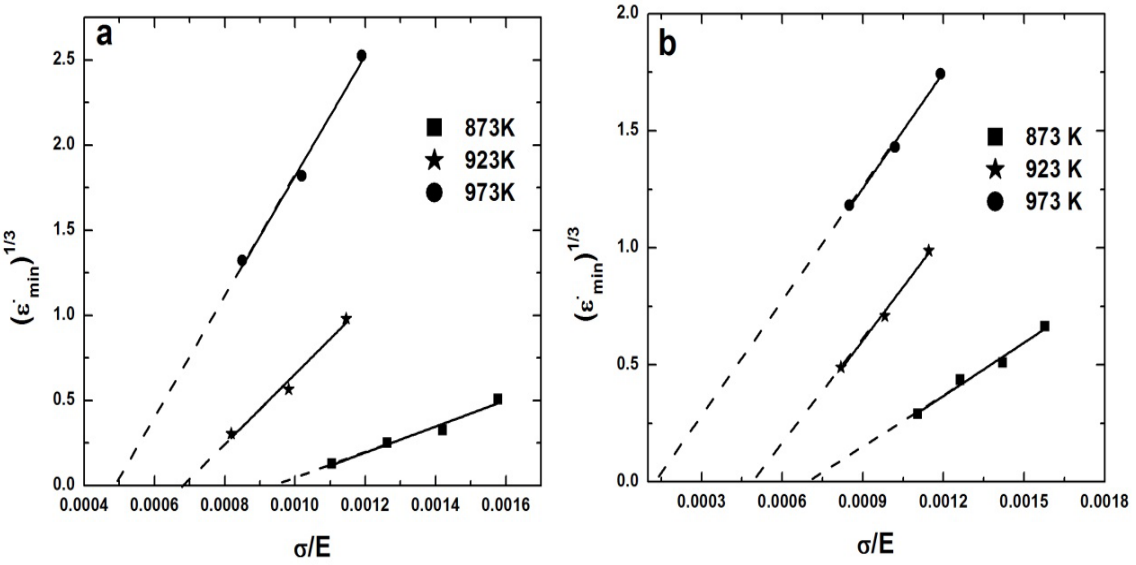


Figure 4.24 Linear extrapolation plot for threshold stress calculation for (a) viscous glide ($n$ = 3) and (b) dislocation climb ($n$ = 5).

stresses obtained from the linear extrapolation at 873, 923, and 973 K for $n$ = 3 were 150.1, 104.4, and 71.5 MPa, respectively. The threshold stresses obtained from the linear extrapolation at 873, 923, and 973 K for $n$ = 5, were 113.3, 76.8, and 20.6 MPa, respectively.

The obtained threshold stresses were incorporated in double logarithmic plot of minimum creep rate and stress as shown in Figure 4.25. After incorporating the threshold stress, in both the cases, stress exponent reduced from higher value to lower value. Stress exponent reduced to a single value of ~3 for all the temperatures after incorporating the calculated threshold stress assuming creep mechanism as viscous glide ($n$ = 3) as shown in Figure 4.25a. A stress exponent of 5 was obtained assuming creep mechanism as dislocation climb ($n$ = 5) as shown in Figure 4.25b. To calculate the true activation energy, minimum creep rate was plotted against modulus compensated effective stress for each temperature.

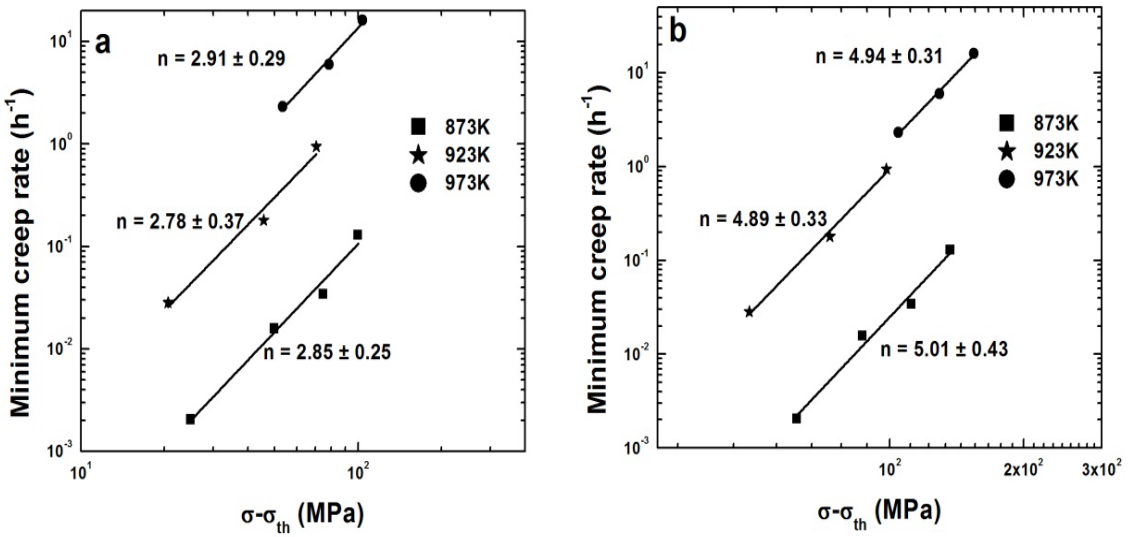


Figure 4.25 Double logarithmic plots between minimum creep rate vs. effective stress for true stress exponent assuming (a) viscous glide and (b) dislocation climb as a creep mechanism.

Then, the corresponding creep rate was taken for each temperature at constant modulus compensated effective stress. The obtained creep rates were plotted against inverse of temperature for both the cases as shown in Figure 4.26. True Activation energy of 289 kJ/mol is obtained assuming stress exponent of 3 at $4.0\times10^{-4}$ modulus compensated effective stress as shown in Figure 4.26a. Similarly, true Activation energy of 290 kJ/mol is obtained assuming stress exponent of 5 at $8.2\times10^{-4}$ modulus compensated effective stress as shown in Figure 4.26b. The obtained activation energy is reduced from the high value of 621 kJ/mol to 290 kJ/mol which is close to activation energy of lattice diffusion in α-iron. Afterward, all the minimum creep rates obtained for each temperature were normalized with lattice diffusion ($\dot{\varepsilon_{min}}kT/DEb$) and plotted against modulus compensated effective stress ($(\sigma-\sigma_{th})/E$) to verify operating creep mechanism between viscous glide ($n = 3$) and dislocation climb ($n > 4$).

D is the diffusivity described by the following relation, $D = D_o \exp(-\frac{Q_{apt}}{RT})$, where $Q_{apt}$ is the apparent activation energy obtained from linear extrapolation for $n = 3$ and $n = 5$, $D_0$ (diffusivity constant) is equal to $1.9\times10^{-4}$ $m^2s^{-1}$ [23], $R$ is the gas constant, and T is the temperature in K. Burgers vector of $2.8\times10^{-10}$ m [23] and $E_o$ (shear modulus) of 223 GPa was used. Figure 4.27a and Figure 27b are the normalized plots for viscous glide ($n = 3$) and dislocation climb ($n = 5$), respectively. It can be seen that all the data fall reasonably close to 2.8 (~3) when true activation energy and threshold stress were taken assuming viscous glide as creep mechanism ($n = 3$) as shown in Figure 4.27a. On the other hand, a single stress exponent of 3.98 is obtained when true activation energy and threshold stress was incorporated assuming dislocation climb as a creep mechanism ($n = 5$) as shown in Figure 4.27b.

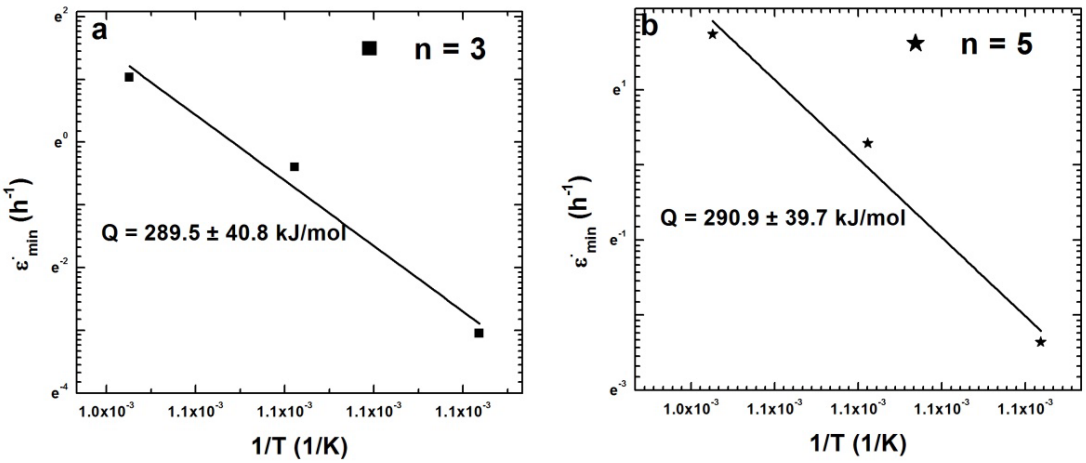


Figure 4.26 Minimum creep rate vs. inverse temperature plot for true activation energy assuming (a) viscous glide and (b) dislocation climb.

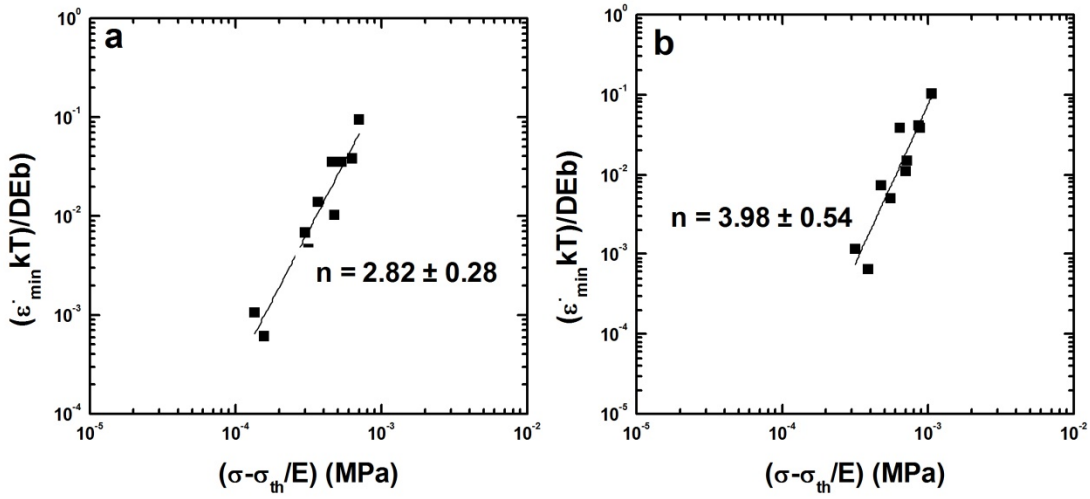


Figure 4.27 Plot between diffusion compensated minimum creep rate vs. modulus compensated effective stress (a) for viscous glide ($n$ = 3) and (b) for dislocation climb ($n$ = 5).

Quite a large difference in stress exponent (3.98) from the assumed stress exponent (5) is found in the latter case. Assuming viscous glide as creep mechanism, all the data merged reasonably well close to assumed stress exponent of ~3. Therefore, it could be concluded that the creep deformation mechanism of weld transition joint studied in the present work at high stress regime is viscous glide. This is in contradiction with the reported creep mechanism of 9Cr-1Mo steel which is predominantly accepted as dislocation climb [18,23]. However, this difference can be anticipated by considering the structural changes induced during creep exposure between a parent metal and dissimilar joint metal.

As shown in Figure 4.20, all the failures were located at the soft zone in HAZ of P91 and was also confirmed with other crept specimens as shown in Figure 4.28. Figure 4.28a and Figure 4.28b are the microstructures of crept sample tested at 873 K/175 MPa (rupture time 652 h) near the weld interface and fracture tip, respectively. Figure 4.28a reveals typical lath martensitic structure with a hardness of 280 HV near the weld interface. On the other hand, microstructure near the fracture tip shows loss of martensite as shown in Figure 4.28b also in conformity with hardness value of 205 HV. It is also observed that these soft zone widths exist in HAZ of P91 extent over time towards FGHAZ. The formation and extension of soft zone is facilitated by diffusion of carbon from lath martensite which will precipitate out in the form of carbides at the grain boundaries. Therefore, viscous glide creep mechanism in these weld joints could be due to diffusion of carbon atoms. The activation energy of carbon diffusion in Fe and/or Ni is quite small. It is proposed that as solute atoms diffuse, they drag the pinned dislocations with them and create solute drag viscous glide.

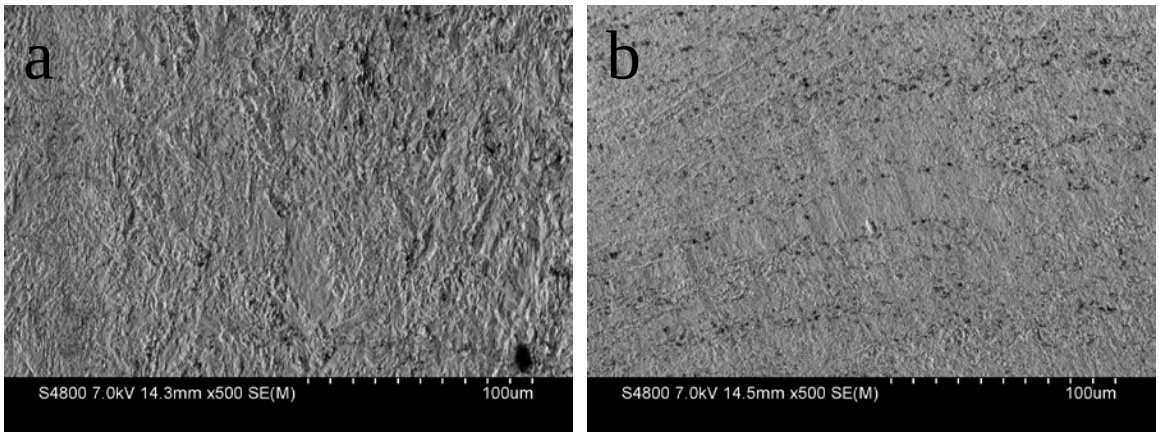


Figure 4.28 Microstructure of crept sample tested at 873 K and 175 MPa (Rupture time = 652 hours) (a) at the interface of 9Cr-1Mo steel and Inconel 625 (b) at fracture tip.

It is reported in the literature that when stress exponent $n$ = 3, dislocation glide is controlled by the rate of migration of solute atoms that are attached to moving dislocations [27,28]. Therefore, the controlling creep mechanism of the weld joints studied in the present work is proposed to be viscous glide due to the diffusion of carbon.

4.2.2.5 Analysis of creep rupture data

The time to reach the onset of the tertiary stage is related to rupture time by the following relationship.

$$t_{rt}^{m} = C t_{ots}$$

where $t_{rt}$ is the rupture time, $t_{ots}$ is the onset of the tertiary stage, and $C$ is a constant. Figure 4.29 shows the plot between rupture time and onset of the tertiary stage. All the data are fitted considerably well in a straight line with a slope of ~1.0. From the deduced constant value, $t_{ots}$ is equal to 0.44 fraction of $t_{rt}$ where exponent '$m$' is almost equal to 1. This indicates that the time spent in the tertiary stage is quite large and contribution from the secondary and primary creep stage is small.

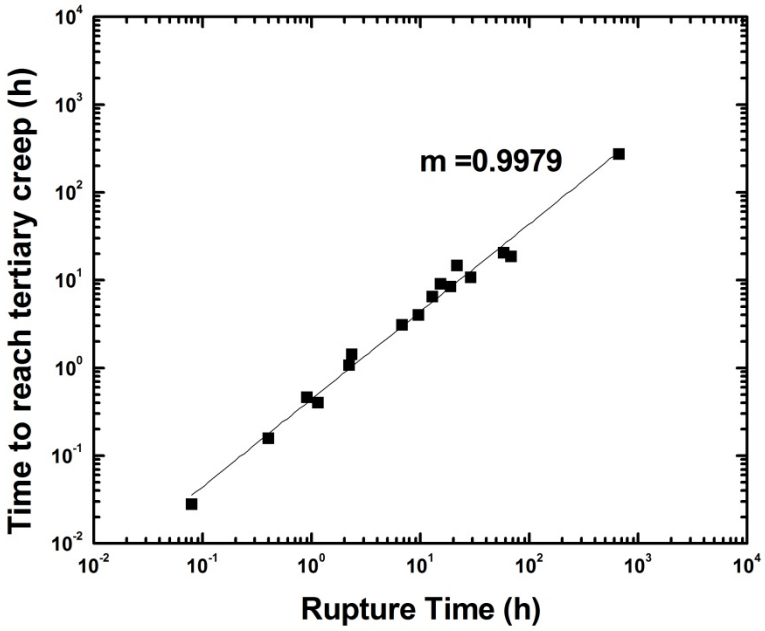


Figure 4.29 Plot between time to reach tertiary creep vs. rupture time for three and single layer welds at 873, 923, and 973 K.

This also suggests that contribution to the creep strain from secondary and primary is small as compared to the tertiary stage and maximum ductility was derived from the tertiary stage of the creep. Low value of C (0.28) was also obtained in 9Cr-1Mo steel [21]. The minimum creep rate and rupture time relationship is given by the Monkman-Grant equation [29] and expressed as follows

$$\dot{\varepsilon}_m^{m\prime} t_{rt} = C_{MG}$$

where $C_{MG}$ is the Monkman-Grant constant, $t_{rt}$ the time to rupture, and $\dot{\varepsilon}_m$ the minimum creep rate. $C_{MG}$ and $m'$ are the constants and independent of testing temperature, stress, chemical composition, and heat treatment of a particular alloy [29]. Figure 4.30a is a log-log plot between rupture time and minimum creep rate. Data fall considerably well in a straight line with a slope of ($m'$) 0.92. The Monkman Grant constant ($C_{MG}$) is quite high as compared to 0.036 [21], and 0.04 [20] reported for 9Cr-1Mo steel.

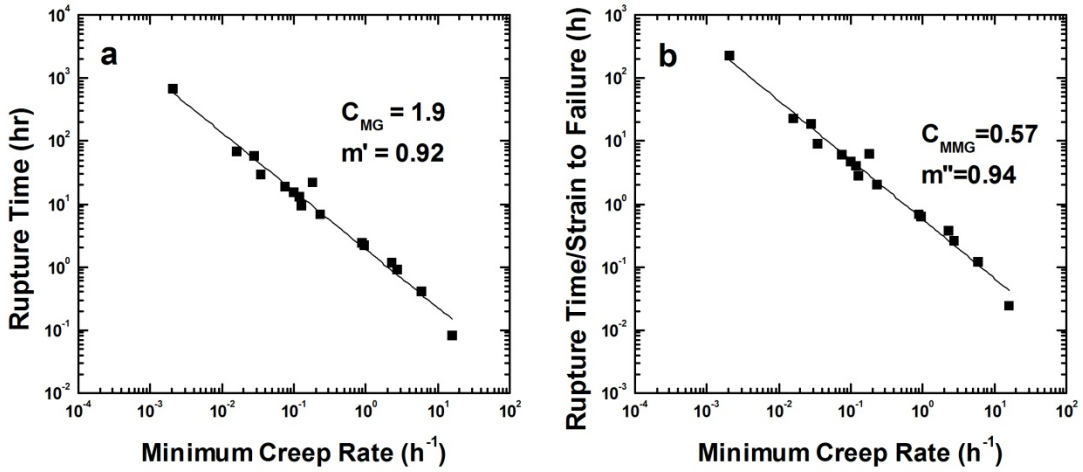


Figure 4.30 Plots of rupture time vs. minimum creep rate showing Monkman-Grant relation (a) and (b) plot between ratio of rupture time to strain to failure and minimum creep rate for Modified Monkman-Grant relation.

However, variation in intercept values is very common in metallic alloys, and such high constant values were also included in Monkman-Grant work [29]. The slope value obtained in this study is close to 0.92 (~1.0), and such values are indicated in studies reported by Monkman-Grant [29], Choudhary et al. [21], and Shrestha et al. [20]. It is also mentioned that $m'$ value close to 1 is better for good prediction. Therefore, the obtained relationship between rupture time and minimum creep rate can be used for the prediction of rupture time.

Dobes and Milicka [30] proposed a Modified Monkman-Grant relation for metallic alloys which incorporates true fracture strain in the relationship given by the following relation:

$$\dot{\varepsilon}_m^{m''} \frac{t_{rt}}{\varepsilon_f} = C_{MMG}$$

where $\varepsilon_f$ is the strain to fracture and $C_{MMG}$ and $m$" are the Modified Monkman Grant

constants independent of stress and temperature. Figure 4.30b is a log-log plot between rupture time/strain to failure and minimum creep rate. Slope (m′′) of 0.94 and constant value ($C_{MMG}$) of 0.57 was obtained for weld joints as shown in Figure 4.30b. From obtained constant ($C_{MMG}$), creep damage tolerance factor ($\lambda$) was evaluated. Creep damage tolerance factor ($\lambda$) is expressed as inverse of ($C_{MMG}$) [31,32] and used to find out operating rupture mode. Typically, the value of $\lambda$ ranges from 1 to 20 for engineering alloys [20,32]. There are many ways creep damage can occur such as external necking, internal necking due to cavity formation and growth, oxidation, and microstructural degradation (coarsening of particles) [21,32]. Each creep damage mechanism acting on material results in corresponding value of $\lambda$.

For example, when $\lambda$ = 1, creep damage occurs in a brittle fracture mode without significant plastic deformation and have very low creep strain. $\lambda$ values in between 1.5 to 2.5 indicates that damage is facilitated by growth of cavities due to combined effect of power law and diffusional creep [32]. Higher value of $\lambda$ (more than 5) indicates that material can withstand strain concentration without local cracking and microstructural degradation as the dominant creep damage mechanism. In the present work, intermediate value of $\lambda$ is obtained which is 1.75 for weld joints. This value falls in the range of 1.5 to 2.5 indicating that the creep damage mechanism is due to growth of cavities from combined effect of power law and diffusion creep. Creep damage tolerance factor ($\lambda$) of 1.75 obtained in the present work is also in conformity with the fractography results as shown in Figure 4.21. The entire fractured surface reveals the presence of creep cavities and voids. Therefore, the creep damage mechanism in weld joints in the present work is attributed to growth of cavities.

### 4.2.3 Conclusions

Weld transition joints between P91 steel and AISI 304 consisting of three Inconel interlayers (P91/IN625/IN600/IN800H/AISI304) showed better rupture life as compared to single interlayer welds (P91/IN600/AISI304). The increased rupture life is attributed to gradual transition in coefficient of thermal expansion between P91 steel and AISI 304 stainless steel. A stress exponent of 3 was obtained suggesting creep mechanism as viscous glide due to solute drag effect. Transgranular mode of fracture was observed in all crept samples. Creep damage tolerance factor ($\lambda$) of 1.75 was obtained which indicates the damage mechanism due to cavity growth by the combined effect of power law and diffusion creep.

## 4.3 References

[1] M. Maalekian, Friction welding – critical assessment of literature, Sci. Technol. Weld. Join. 12 (2007) 738–759. doi:10.1179/174329307X249333.

[2] S.D. Meshram, T. Mohandas, G.M. Reddy, Friction welding of dissimilar pure metals, J. Mater. Process. Technol. 184 (2007) 330–337.

[3] H.K. Rafi, G.D.J. Ram, G. Phanikumar, K.P. Rao, Microstructure and tensile properties of friction welded aluminum alloy AA7075-T6, Mater. Des. 31 (2010) 2375–2380. doi:10.1016/j.matdes.2009.11.065.

[4] V. V. Satyanarayana, G.M. Reddy, T. Mohandas, Dissimilar metal friction welding of austenitic-ferritic stainless steels, J. Mater. Process. Technol. 160 (2005) 128–137. doi:10.1016/j.jmatprotec.2004.05.017.

[5] J. a. Francis, W. Mazur, H.K.D.H. Bhadeshia, Review Type IV cracking in ferritic power plant steels, Mater. Sci. Technol. 22 (2006) 1387–1395..

[6] K. Laha, K.S. Chandravathi, P. Parameswaran, K.B. Sankara, S.L. Mannan, Characterization of microstructures across the heat-affected zone of the modified 9cr-1mo weld joint to understand its role in promoting Type IV cracking, Metall. Mater. Trans. A. 38A (2007) 58–67. doi:10.1007/s11661-006-9050-0.

[7] S. Mannan, K. Laha, Creep behaviour of Cr–Mo steel weldments, Trans. Indian

Inst. Met. 49 (1996) 303–320.

[8] X. Yu, Multi-scale characterization of heat-affected zone in martensitic steels, (2012).

[9] R.J. Christoffel, M.R. Curran, Carbon migration in welded joints at elevated temperatures, Weld. J. 35 (1956) 457s–468s.

[10] J.M. Race, Carbon diffusion across dissimilar steel welds, 1992.

[11] Y.Y. You, R.K. Shiue, R.H. Shiue, C. Chen, The study of carbon migration in dissimilar welding of the modified 9Cr-1Mo steel, J. Mater. Sci. Lett. 20 (2001) 1429–1432. doi:10.1023/A:1011616232396.

[12] J.F. Eckel, Diffusion across dissimilar metal joints, Weld. J. 43 (1964) 170s–178s.

[13] C.D. Lundin, Dissimilar metal welds — transition joints literature review, Weld. J. (1982) 58s–63s.

[14] A.K. Bhaduri, Transition metal joints for steam generatore-an overview, Int. J. Press. Vessel. Pip. 58 (1994) 251–265.

[15] J.N. Dupont, R.E. Mizia, Review of dissimilar metal welding for the NGNP helical-coil steam generator, 2010. doi:INL/EXT-10-18459.

[16] M.E. Abd El-Azim, O.H. Ibrahim, O.E. El-Desoky, Long term creep behaviour of welded joints of P91 steel at 650℃, Mater. Sci. Eng. A. 560 (2013) 678–684. doi:10.1016/j.msea.2012.10.013.

[17] F. Abe, Precipitate design for creep strengthening of 9% Cr tempered martensitic steel for ultra-supercritical power plants, Sci. Technol. Adv. Mater. 9 (2008) 013002. doi:10.1088/1468-6996/9/1/013002.

[18] T. Shrestha, M. Basirat, I. Charit, G.P. Potirniche, K.K. Rink, U. Sahaym, Creep deformation mechanisms in modified 9Cr-1Mo steel, J. Nucl. Mater. 423 (2012) 110–119. doi:10.1016/j.jnucmat.2012.01.005.

[19] K. Laha, K.S. Chandravathi, P. Parameswaran, S. Goyal, M.D. Mathew, A comparison of creep rupture strength of ferritic/austenitic dissimilar weld joints of different grades of Cr-Mo ferritic steels, Metall. Mater. Trans. A. 43 (2012) 1174–1186. doi:10.1007/s11661-011-0957-8.

[20] T. Shrestha, M. Basirat, I. Charit, G.P. Potirniche, K.K. Rink, Creep rupture behavior of grade 91 steel, Mater. Sci. Eng. A. 565 (2013) 382–391. doi:10.1016/j.msea.2012.12.031.

[21] B.K. Choudhary, E. Isaac Samuel, Creep behaviour of modified 9Cr-1Mo ferritic steel, J. Nucl. Mater. 412 (2011) 82–89. doi:10.1016/j.jnucmat.2011.02.024.

[22] P. Anderson, T. Bellgardt, F.L. Jones, Creep deformation in a modified 9Cr-1Mo steel_2003, Mater. Sci. Technol. 19 (2003) 207–213.

[23] B. Ule, A. Nagode, A model based creep equation for 9Cr–1Mo–0·2V (P91 type) steel, Mater. Sci. Technol. 23 (2007) 1367–1374.

[24] S. Spigarelli, E. Cerri, P. Bianchi, E. Evangelisa, Interpretation of creep behaviour of a 9Cr-Mo-Nb-V-N steel using threshold stress concept, Mater. Sci. Technol. 15 (1999) 1433–1440.

[25] R.S. Mishra, T.R. Bieler, A.K. Mukherjee, Superplasticity in powder metallurgy aluminum alloys and composites, Acta Metall. Mater. 43 (1995) 877–891.

[26] Y. Huang, T.G. Langdon, The creep behavior of discontinuously reinforced metal-matrix composites, Jom. 55 (2003) 15–20. doi:10.1007/s11837-003-0187-7.

[27] O.D. Sherby, E.M. Taleff, Influence of grain size, solute atoms and second-phase particles on creep behavior of polycrystalline solids, Mater. Sci. Eng. A. 322 (2002) 89–99. doi:10.1016/S0921-5093(01)01121-2.

[28] G. Graiss, A.F. Abd El-Rehim, Examination of breakdown stress in creep by viscous glide in Al-5·5 at.-%Mg solid solution alloy at high stress levels, Mater. Sci. Technol. 23 (2007) 1144–1148. doi:10.1179/174328407X226545.

[29] F. Monkman, N. Grant, An empirical relationship between rupture life and minimum creep rate in creep-rupture tests, Proc. ASTM. 56 (1956) 593–620.

[30] F. Dobes, K. Milicka, The relation between minimum creep rate and time to fracture, Met. Sci. 10 (1976) 382–384.

[31] F.A. Leckie, D.R. Hayhurst, Constitutive equations for creep rupture, Acta Metall. 25 (1977) 1059–1070.

[32] M.F. Ashby, B.F. Dyson, Advances in Fracture Research, vol 1, 1984.

# CHAPTER 5

# CONCLUSIONS

1) Process parameters such as consumable rod rotational speed (RPM), feed rate (mm/min) and axial load (N), and high temperature strength of material a played significant role in affecting the friction surfaced metallic coating dimensions.

2) All the friction surfaced coatings studied were found to exhibt dynamic recrystallization. Grain refinement and increase in hardness were observed in all Ni-based alloy coatings due to the dynamic recrystallization. The carbide particles were found to be finer and distributed uniformly throughout the matrix, compared to their consumable rod counterparts.

3) Dynamically recrystallized grains were observed near the weld interface of friction welded transition joints in as-weld conditions. Grain growth was observed near the weld interface after post weld heat treatment.

4) Friction welding method was selected for developing the weld transition joints due to its simplicity, less time and material consumption, and larger grain size near the interface which is helpful for creep strength.

5) Microstructural modeling route was adopted to predict the strain rates in friction welds of Inconel 718 during welding operation using cellular automata method. All the simulated grain sizes were found to be comparable well with the experimental

results. Larger grain size was observed at low strain rates and high temperature attributed to more deformation time and higher mobility. The strain rates predicted from the model at the center and edge of the weld for 1500 RPM weld were found to be 1850 $s^{-1}$ and 290 $s^{-1}$, respectively. The predicted strain rates were compared with torsion type deformation model. In all the cases, finer grain size was observed at the weld center as compared to edge of the weld. Temperature difference of smaller value showed significant effect on resulting grain size.

6) The soft zone in the HAZ of P91 was observed 2mm away from the weld interface for both single and three layer welds and is attributed to the intercritical heating (between $AC_1$ and $AC_3$) during welding operation. Apart from the soft zone in the HAZ of P91 (2mm away from the interface), the weld interface between P91 and IN625 also showed soft zone formation whereas the interface between P91 and IN600 did not show such a soft zone. Soft zone formation near the weld interface is attributed to carbon diffusion.

7) Weld transition joints between P91 steel and AISI 304 fabricated with multilayer Ni-based alloys (P91/IN625/IN600/IN800H/AISI304) showed better rupture life as compared to single interlayer welds (P91/IN600/AISI304). The increased rupture life is attributed to gradual transition in coefficient of thermal expansion between P91 steel and AISI 304 stainless steel. A stress exponent of 3 was obtained suggesting creep mechanism as viscous glide due to solute drag effect. Transgranular mode of fracture was observed in all crept samples. Creep damage tolerance factor ($\lambda$) of 1.75 was obtained which indicates the damage mechanism is cavity growth by the combined effect of power law creep and diffusional creep.

# CHAPTER 6

# FUTURE WORK

The creep data presented here were mostly a short-term creep test and the failure locations were identified at the soft zone in the HAZ of P91. However, in real service condition these joints are exposed to elevated temperature for a longer time. As showed the three layer weld formed a soft zone at the interface during the heat treatment, long-term creep test could shift the failure location from the soft zone in the HAZ of P91 to the interface of joint. Therefore, a long-term creep test of at least more than 2000 to 5000 hours would be helpful to get better insight of failure locations. Apart from a long-term creep test, work should also go in the direction of suppressing the formation of the soft zone in the HAZ of P91 which occurs due to intercritical heating during welding operation. Finally, microstructural modeling route can also be taken up to understand the formation of these soft zone by applying the first principle of diffusion law and recrystallization phenomena.

# APPENDIX

## LIST OF PUBLICATIONS


[1] J. Akram, R. Puli, P.R. Kalvala, M. Misra, A novel weld transition joint by friction surfacing, Manuf. Lett. 2 (2014) 104–107.

[2] J. Akram, P.R. Kalvala, M. Misra, Effect of process parameters on friction surfaced coating dimensions, Adv. Mater. Res. 922 (2014) 280–285.

[3] J. Akram, P.R. Kalvala, M. Misra, Stress rupture behavior of P91-AISI 304 weld transition joint developed by friction surfaced additive manufacturing method, TMS2015 Annu. Meet. Suppl. Proc. (2015) 405–412.

[4] J. Akram, R. Puli, P.R. Kalvala, M. Misra, Microstructural studies on friction surfaced coatings of Ni-based alloys, Pract. Metallogr. 52 (2015) 590–606.

[5] J. Akram, J.. J.S. Dilip, D. Pal, B. Stucker, P.R. Kalvala, M. Misra, Microstructures of friction surfaced coatings – a TEM study. Practical Metallography, Pract. Metallogr. 53 (2016) 261–272.

[6] P. Rao, J. Akram, M. Misra, Low temperature frictions stir welding of P91 steel, Def. Technol. (2015). doi:10.1016/j.dt.2015.11.003.

[7] P.R. Kalvala, J. Akram, M. Misra, Friction assisted solid state lap seam welding and additive manufacturing method, Def. Technol. 12 (2016) 16–24. doi:10.1016/j.dt.2015.11.001.